Combined optical imaging and electric transport studies on resistive switching and light-induced phase transitions in strongly correlated insulators

Dissertation
der Mathematisch-Naturwissenschaftlichen Fakultät
der Eberhard Karls Universität Tübingen
zur Erlangung des Grades eines
Doktors der Naturwissenschaften
(Dr. rer. nat.)

vorgelegt von
Theodor Hans Albert Luibrand
aus Weingarten

Tübingen
2024

Abstract

The emerging field of neuromorphic computing strongly demands for memristive devices in order to emulate basic functionalities of the human brain. In recent years, there is growing interest in devices based on strongly correlated insulator thin films, which undergo thermally driven metal-to-insulator transitions (MIT) and insulator-to-metal transitions (IMT). These materials show memristive behavior due to resistive switching, i.e. the change of electical resistance induced by an external stimulus.

In the three publications of this cumulative PhD thesis, we adress distinct research questions in the scope of the fundamental mechanism behind resisitve switching, spatial switching dynamics, and thermodynamical aspects of laser light-induced phase transitions.

In **publication 1**, we investigate the characteristic length scales of conductive filaments in planar two-terminal thin film devices of the perovskite nickelates $NdNiO_3$ and $SmNiO_3$. For potential applications, it is crucial to have knowledge about the spatial filament dynamics, e.g. for miniaturization, but this fundamental question has been mostly unnoticed so far. In a study with complementary imaging techniques, namely optical widefield and scattering-type scanning near-field optical microscopy and with theoretical support by numerical simulations, we find key parameters, that determine the size of the filament. We identify the resistivity contrast during MIT/IMT to be a key parameter for the filament's size. Larger resistive drops and sharp switching leads to narrower filaments with higher current density. Besides of that, bias current, temperature and thermal conductivity of the substrate play important roles, too.

In **publication 2**, we present a study on resistive switching in the prototypical Mott insulator V_2O_3, touching the fundamental question of the origin of resistive switching. By use of optical widefield microscopy, we visualize the thermally driven strain-induced phase separation during MIT/IMT as well as volatile resistive switching in a planar two-terminal thin film device. The current-voltage-characteristics and the shape of the filaments are well reproduced by a numerical model, unveiling clear signs of an electrothermal breakdown, and correlating local heterogeneities like strain directly to the switching dynamics.

In **publication 3**, we study laser irradiation of a V_2O_3 thin film and gain thermodynamical insights into the first-order nature of the Mott transition. We irradiate the sample by scanning a focused laser beam across the thin film surface and acquire optical widefield micrographs *in situ*. Laser irradiation modifies the phase configuration depending on the thermal history: during IMT, the laser induces predominantly metallic domains, whereas during MIT, it predominantly induces insulating domains. Most likely, the laser beam drives metastable states into stable ones in a non-thermal way. A numerical model supports this hypothesis.

Kurzfassung

Neuromorphes Computing ist ein aufstrebendes Forschungsgebiet, dessen Ziel es ist, grundlegende Funktionen des menschlichen Gehirns nachzuahmen. Dafür werden dringend Bauteile mit memristiven Eigenschaften gebraucht. In den letzten Jahren ist das Interesse an Bauelementen, die auf dünnen Schichten aus stark korrelierten Isolatoren basieren, gewachsen. Diese Materialien durchlaufen thermisch getriebene Metall-Isolator- und Isolator-Metall-Übergänge. Die Bauteile zeigen memristives Verhalten aufgrund von resistivem Schalten, d. h. der Änderung des elektrischen Widerstands durch einen externen Stimulus.

In den drei Veröffentlichungen dieser kumulativen Dissertation werden verschiedene Forschungsfragen behandelt: Fragen nach den grundlegenden Mechanismen des resistiven Schaltens, nach der räumlichen Schaltdynamik metallischer Filamente sowie nach thermodynamischen Aspekten laser-induzierter Phasenübergänge.

In **Publikation 1** werden die charakteristischen Längenskalen leitender Filamente in planaren, zweipoligen Dünnschichtbauelementen aus den Perowskit-Nickelaten $NdNiO_3$ und $SmNiO_3$ untersucht. Für potenzielle Anwendungen ist die Kenntnis der räumlichen Filamentdynamik von entscheidender Bedeutung, beispielsweise für die Miniaturisierung von Bauelementen. Dennoch ist diese grundlegende Fragestellung in der Forschung bisher weitgehend unbeachtet geblieben. Mithilfe komplementärer bildgebender Verfahren sowie theoretischer Unterstützung mit numerischen Simulationen können Schlüsselparameter, die die Breite des Filaments bestimmen, identifiziert werden. Die Abbildungstechniken der Wahl sind hierbei optische Weitfeld- sowie Rasternahfeld-Mikroskopie. Es stellt sich heraus, dass die Höhe der Widerstandsänderung während des Metall-Isolator- bzw. Isolator-Metall-Übergangs ein Schlüsselparameter für die Breite des Filaments ist. Größere Widerstandsänderungen und steiles resistives Schalten führen zu schmaleren Filamenten mit höherer Stromdichte. Zusätzlich sind dabei auch der Bias-Strom, die Temperatur sowie die Wärmeleitfähigkeit des Substrats von Bedeutung.

Publikation 2 ist eine Studie über resistives Schalten im prototypischen Mott-Isolator V_2O_3, die die grundlegende Frage nach dem Ursprung des resistiven Schaltens berührt. Mittels optischer Weitfeldmikroskopie wird sowohl die thermisch getriebene, verspannungsinduzierte Phasenseparation während des Metall-Isolator- sowie Isolator-Metall-Übergangs als auch das volatile resistive Schalten, das mit der Bildung eines leitenden Filaments einhergeht, in einem planaren zweipoligen Dünnschichtbauelement visualisiert. Die Strom-Spannungs-Kennlinien sowie die Form der Filamente werden durch ein numerisches Modell sehr gut reproduziert. Einerseits gibt es dadurch klare Anzeichen für einen elektrothermischen Zusammenbruch, andererseits können lokale Heterogenitäten wie Verspannungen im Dünnfilm direkt mit der räumlichen Schaltdynamik korreliert werden.

In **Publikation 3** wird die Auswirkung der Bestrahlung eines V_2O_3-Dünnfilms mit einem fokussierten Laserstrahl untersucht. Hierbei lassen sich thermodynamische Erkenntnisse über die Natur des Mott-Übergangs erster Ordnung gewinnen. Die Probe wird bestrahlt, indem ein fokussierter Laserstrahl über die Dünnschichtoberfläche geras-

tert wird. Vor und nach der Bestrahlung werden Abbildungen mittels optischer Weit-feldmikroskopie *in situ* aufgenommen. Die Laserbestrahlung verändert die Phasenkonfiguration in Abhängigkeit von der thermischen Vorgeschichte des Dünnfilms: Während des Isolator-Metall-Übergangs induziert der Laser vorwiegend metallische Domänen, wohingegen während des Metall-Isolator-Übergangs vorwiegend isolierende Domänen induziert werden. Wahrscheinlich treibt der fokussierte Laserstrahl metastabile in stabile Zustände – vermutlich auf nicht-thermische Art und Weise. Ein numerisches Modell stützt diese Hypothese.

List of Publications

This is a cumulative thesis based on three publications. Summaries of the publications can be found in Chap. 2.

The publications are not in a chronological order, but assorted thematically with respect to the device materials under test. **Publication 1** deals with resistive switching and filament formation in the nickelates $NdNiO_3$ and $SmNiO_3$, **publication 2** introduces the vanadate V_2O_3 and examines filamentary resistve switching as well. **Publication 3** is also a V_2O_3 study dealing with optically induced phase transitions.

The publications are appended at the end of this thesis.

Publication 1 **Theodor Luibrand**, Adrien Bercher, Rodolfo Rocco, Farnaz Tahouni-Bonab, Lucia Varbaro, Carl Willem Rischau, Claribel Domínguez, Yixi Zhou, Weiwei Luo, Soumen Bag, Lorenzo Fratino, Reinhold Kleiner, Stefano Gariglio, Dieter Koelle, Jean-Marc Triscone, Marcelo J. Rozenberg, Alexey B. Kuzmenko, Stefan Guénon, and Javier del Valle

Characteristic length scales of the electrically induced insulator-to-metal transition

Physical Review Research **5**, 013108 (2023)

Publication 2 Matthias Lange, Stefan Guénon, Yoav Kalcheim, **Theodor Luibrand**, Nicolas M. Vargas, Dennis Schwebius, Reinhold Kleiner, Ivan K. Schuller, and Dieter Koelle

Imaging of Electrothermal Filament Formation in a Mott Insulator

Physical Review Applied **16**, 054027 (2021)

Publication 3 **Theodor Luibrand**, Lorenzo Fratino, Farnaz Tahouni-Bonab, Amihai Kronman, Yoav Kalcheim, Ivan K. Schuller, Marcelo Rozenberg, Reinhold Kleiner, Dieter Koelle, and Stefan Guénon

Laser-induced quenching of metastability at the Mott-insulator to metal transition

arXiv:2401.11889 [cond-mat.str-el]

Contents

Chapter 1

Introduction

1.1 Motivation – Bio-inspired neuromorphic computing

Neuromorphic computing is an emerging field of research with the aim to complement conventional computing [1–4]. Conventional computing implies silicon-based programmable complementary metal-oxide-semiconductor (CMOS) computing machines. Characteristically, these modern conventional computers perform computing steps digitally and serially with clock frequencies in the GHz regime and with very high precision. This technique was key for the digital revolution of the past decades, but it has limits. One of those is the von Neumann bottleneck: the conventional computer architecture spatially separates the central processing unit from the memory unit. The data transfer between those is slow and energy consuming, often referred to as von Neumann latency. Furthermore, the serial execution of computing steps limits the speed of computing (e.g. large matrix multiplications).

The development of artificial neural networks (ANN) in computer science [5, 6] was a milestone towards biomimetic, brain-inspired computing. Realization of ANNs is possible with high-end conventional computers, but goes along with high energy consumption. Neuromorphic systems, however, try to follow the architecture of the human brain, which shows a huge amount of interconnectivity between a massive number of neurons via even more synapses. Neurons and synapses are the central elements of biological neural networks. Neurons produce voltage spikes after being triggered by an electrical stimulus reaching a certain threshold, which is referred to as "firing". Crucial is not the strength, but the frequency of the trigger signal, i.e. the neuron will fire only after it was stimulated by a certain amount of spikes in a given time interval. This leads to the characteristic features of neurons, namely leaky-integrate-and-fire. In an oversimplified physical model, the neuron can be seen as capacitor, which can be charged by voltage spikes (integrate) until reaching a threshold (fire) while slowly discharging (leaky). This feature requires volatile, i.e. non-permanent changes of states. On the contrary, synapses, the signal transmitters and simultaneous memory units of the network, require non-volatile behavior. This is due to the fact, that synapses show plasticity, i.e. the stimulus created by the voltage spikes affects their connection strength. Again, these synaptic weights are dependent on the timing of firing activity of connected neurons [7]. Note, that in the human brain each neuron is connected to up to 15.000 other neurons via synapses in a complex three-dimensional network. Furthermore, biological neural network systems do not work in a stable state like conventional computing machines,

but they are in abstract states of criticality (e.g., states close to phase transitions), which means that they are highly susceptible to stimuli causing huge changes in the properties of the system.

Mimicking the human brain leads to the idea of neuromorphic computing. This approach implies high parallelism, i.e. thousands of neurons, that perform analogue computing operations in parallel. The memory unit is integrated in the network, which overcomes the von Neumann bottleneck intrinsically, and due to unreliable and stochastic behavior of single operations steps, the whole system is more robust against propagation of errors. This way, a huge cluster of analogue and unreliable devices can collectively be much more energy-efficient and powerful than conventional digital computers in particular tasks like pattern recognition or in image processing. Research in neuromorphic computing is not anywhere near to reach the complexity and powerfulness of the human brain in the near future, but it can identify essential functionalities of biological systems. First steps were taken by emulating neuronal and synaptic features in form of neuristors [8, 9] or synaptic transistors [10].

Ongoing research reveals quantum materials as promising candidates to realize neuromorphic devices [3, 11]. Quantum materials are a class, that includes materials whose essential properties are governed by quantum effects at macroscopic scales [12, 13], e.g. strongly correlated oxides [3, 11], phase change materials [14, 15] or van-der-Waals materials [16, 17]. Strongly correlated oxides, in particular strongly correlated insulators showing metal-to-insulator transitions [18] are materials with good prospects for neuromorphic applications. Due to hysteretic effects, they show memristive properties, which are crucial for the emulation of basic functionalities of neurons and synapses. A striking point is, that one can take advantage of non-linear properties: small stimuli can cause large responses, for instance in states being close to phase transitions (see Sec. 1.3 and Sec. 1.4), which can be associated with intended states of criticality.

Already today, there are many promising approaches to neuromorphic computing based on strongly correlated insulators. The emulation of a neuronal spiking was demonstrated, first with external capacitors [19], but the desired leaky-integrate-and-fire behaviour was realized recently without external capacitors in devices based on strongly correlated insulators [20–24]. Del Valle *et al.* demonstrated the possibility of re-triggering the resistive switching with subthreshold voltages after having returned into the insulating state for time scales even up to milliseconds [25]. The authors connect this behavior directly to the phenomenon of metastability, which goes along with the first-order nature of the phase transition. In a different approach, current-spike-induced Joule heating was used to trigger resistive switching, and basic neuronal functionalities were implemented as caloritronics-based neuristors [9]. Stochastic computing with probabilistic bits as emerging technology within neuromorphic computing is an additional field for applications of strongly correlated insulator devices [26–29].

Despite these advances, many fundamental phenomena in the complex interplay of many degrees of freedom in strongly correlated insulators are yet poorly understood. This work contributes to some aspects in order to leverage functionality and applicability of devices based on this class of materials.
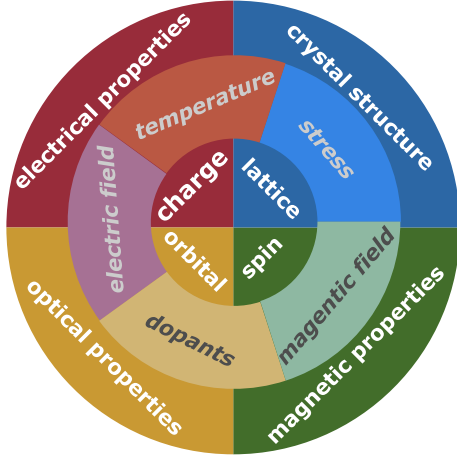
Figure 1.1: Sketch of the complex interplay between different degrees of freedom (inner circle), triggers of phase transitions (middle ring) and physical properties to be changed (outer ring) in strongly correlated insulators. This figure is adapted from [11].

1.2 Strongly correlated insulators

Strongly correlated insulators – as subclass of strongly correlated oxides – attracted considerable research efforts as they are promising candidates for device applications in the emerging field of neuromorphic computing. In fact, strongly correlated insulators are transition metal oxides with partially filled d-bands, that show non-negligible electron-electron correlations [30].

The key feature of strongly correlated insulators is the diverse interplay between internal and external state variables. Figure 1.1 illustrates the connections between various degrees of freedom (inner circle), which can trigger phase transitions (middle ring) and change physical properties (outer ring) of strongly correlated insulators fundamentally. It has to be interpreted as a demonstrative collection of possibilities of the interplay of degrees of freedom in strongly correlated insulators without claiming completeness. For instance, the charge and lattice degrees of freedom can be coupled and via temperature, phase transitions can be triggered, which affect the electrical properties as well as the crystal structure of a sample (see Secs. 1.2.1 and 1.2.2).

This work focuses on actual research questions concerning planar thin film microdevices based on strongly correlated insulators, which undergo temperature-dependent metal-to-insulator transitions (MIT) and insulator-to-metal transitions (IMT). The planarity of the devices allow for optical imaging studies (see Sec. 1.5). The vanadate V_2O_3 (Mott insulator) [31–35] and the rare-earth nickelates $NdNiO_3$ and $SmNiO_3$ (charge transfer insulators) [36, 37] are well-known representatives of this material class.

1.2.1 Mott insulators

Band theory is a basic method to classify materials as metals or insulators. This theory is based on the ansatz of non-interacting delocalized electrons in a periodic lattice of ions. Via the Bloch-theorem, this periodicity leads to distinct regimes in the energy spectrum, the energy bands, which are separated by forbidden regimes of energy, the band gaps [38]. This model implies, that each band – according to the Pauli principle –
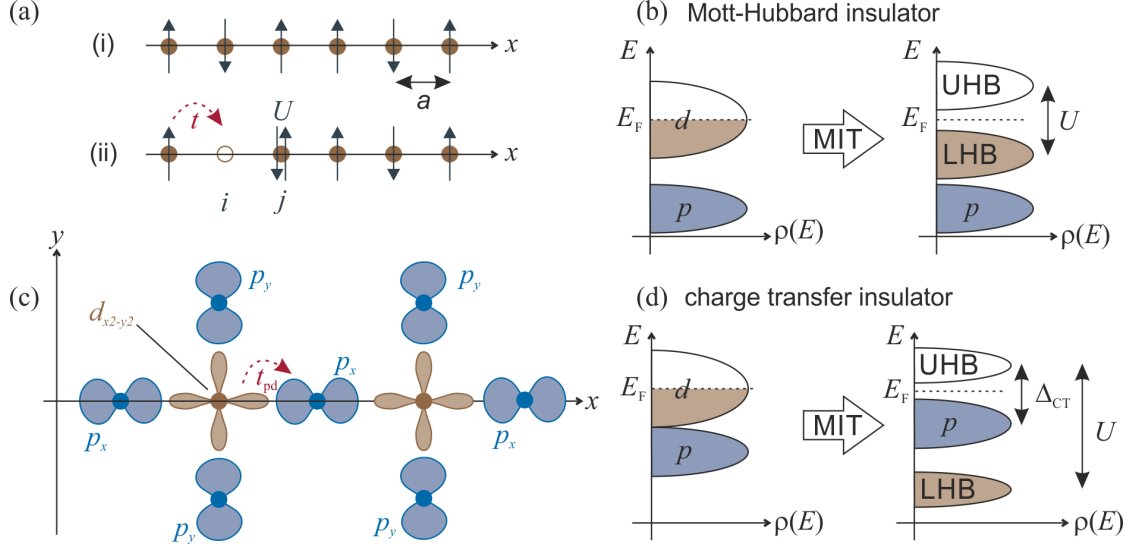
Figure 1.2: Comparison between Mott-Hubbard insulators and charge transfer insulators. (a) 1D lattice illustrating the competition between the hopping energy t and the on-site Coulomb repulsion U. (i) shows one electron per site. (ii) illustrates an excited state: a hole at site i and a doubly occupied site j. (b) Oversimplified band structure illustrating the MIT of a Mott-Hubbard insulator with energy E vs. density of states $\rho(E)$. U separates the empty upper Hubbard band (UHB) from the filled lower Hubbard band (LHB) in the insulating state. E_F denotes the Fermi energy. The blue p band is neglected in the Hubbard model. (c) 2D sketch of a charge transfer insulator: d-orbitals of transition metal sites (brown) are surrounded by p-orbitals of oxygen sites (blue) without distortion. (d) Oversimplified band structure illustrating the MIT of a charge transfer insulator. Δ_{CT} denotes the charge transfer energy, which seperates the empty UHB from the filled oxygen p-band. Figure adapted from [18, 30].

can accommodate $2N$ electrons for N atoms in the crystal. Hence, even numbers of electrons per unit cell or per atom lead to fully filled valence bands, which classifies the material as insulator (or semiconductor, depending on the size of the band gap), whereas odd numbers of electrons per atom lead to partially filled conduction bands, which classifies the material as a metal.

Considering materials, for which the predictions of Bloch theory of energy bands in terms of classification as metal or insulator fails, the Hubbard model introduces electron-electron interaction. The Hubbard model starts from isolated atoms with their specific configurations of electronic orbitals and adds tunneling and hopping of electrons to potential wells of adjacent atoms.

Let's assume the simple case of hydrogen atoms in a 1D lattice equidistantly separated by a lattice constant a (Fig. 1.2(a)). Furthermore, in Fig. 1.2(a)(i), at each site we have one electron in a $1s$-orbital. We can introduce a Hamiltonian, that describes the hopping

of electrons from site to site

$$H_\text{t} = -t \sum_{ij,\sigma} \left(c_{i\sigma}^\dagger c_{j\sigma} + c_{j\sigma}^\dagger c_{i\sigma} \right) , \qquad (1.2.1)$$

where $c_{i\sigma}^\dagger$ and $c_{i\sigma}$ are the creation and annihilation operators at site i with spin σ. The summation goes over nearest neighbors and t is the hopping matrix element. This approach (the tight-binding model) leads to the formation of energy bands as well and classifies the imaginary system "1D hydrogen crystal" as a metal with exactly half-filled conduction band – independent from the lattice constant a. One restriction of this model is evident: if the distance between the atoms is increased, the hopping probability decreases exponentially and the system must turn into an insulator. Taking electron-electron interaction into account, it will cost some amount of energy (the Coulomb repulsion U) to put an electron from site i to an already occupied site j (Fig. 1.2(a)(ii)). This is captured by the Hamiltonian

$$H_\text{U} = U \sum_i n_{i\uparrow} n_{i\downarrow} \qquad (1.2.2)$$

with the electron densities $n_{i\sigma}$ with opposite spins at site i. Combining eq. 1.2.1 and eq. 1.2.2 yields the Hamiltonian of the Hubbard model [39]

$$H_\text{Hubbard} = H_\text{t} + H_\text{U} = -t \sum_{ij,\sigma} \left(c_{i\sigma}^\dagger c_{j\sigma} + c_{j\sigma}^\dagger c_{i\sigma} \right) + U \sum_i n_{i\uparrow} n_{i\downarrow} . \qquad (1.2.3)$$

This model introduces a competition: The total energy gain from electron delocalization of $W = 2zt \propto t$ (which is the bandwidth), where z is the number of nearest neighbors, competes with the on-site Coulomb repulsion U. In simple words, the argument is, that the on-site Coulomb repulsion splits a single band in a lower band with electrons that occupy an empty site and an upper band with electrons that join an already occupied site [18].

For $U/t \gg 1$, the electrons remain localized and the system is a Mott- or Mott-Hubbard insulator [40, 41]. In order to delocalize charge carriers, the system has to overcome the energy gap

$$E_g \propto U - W \approx U . \qquad (1.2.4)$$

Conventionally spoken, in terms of band theory, two Hubbard sub-bands – the lower and upper Hubbard bands (LHB and UHB) – are separated by an energy gap, that is entirely caused by electron-electron interaction, i.e. strong electron correlation (Fig. 1.2(b)). For the opposite case, $U/t \ll 1$, the electrons are delocalized and the material is in the metallic state. A temperature-driven IMT/MIT is commonly known as Mott transition.

The MIT can be induced by changing the electron correlation ratio U/t, for example by a concomitant structural phase transition, which expands the lattice constant and consequently lowers the hopping energy t. This scenario is called bandwidth-controlled
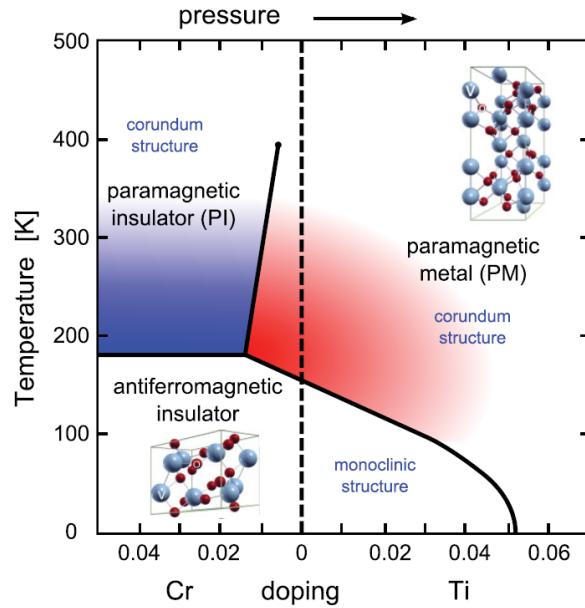
Figure 1.3: Phase diagram of vanadium sesquioxide V_2O_3. Note the double x-axis showing either pressure or doping with Cr and Ti. The insets show unit cells of the corundum and the monoclinic crystal structure, respectively. Used with permission of John Wiley & Sons - Books, from [42]; permission conveyed through Copyright Clearance Center, Inc.

MIT. In contrast to this, by electron or hole doping, the Coulomb repulsion U can be tuned, resulting in a filling-controlled MIT [18].

Of course, the Mott-Hubbard model is restricted: it considers for example only a single energy band, i.e. electrons in a single s-orbit [18]. Strongly correlated insulators like V_2O_3, $NdNiO_3$ and $SmNiO_3$ exhibit rich d-orbital physics, e.g. including orbital degeneracy caused by crystal field splitting or spin-orbit coupling.

Vanadium sesquioxide V_2O_3

A prototypical – even denoted as "veteran" [13] – example of a Mott insulator is vanadium sesquioxide V_2O_3. The phase diagram in Fig. 1.3 shows three distinct phases of V_2O_3 defined by the parameters temperature, pressure and doping (with chromium and titanium): a paramagnetic insulator (PI) phase, a paramagnetic metal (PM) phase and an antiferromagnetic insulator (AFI) phase.

At ambient pressure and room temperature stoichiometric V_2O_3 is in the PM phase with corundum structure. By cooling, it undergoes a sharp MIT at $\sim 150\,\mathrm{K}$ with a change in resistivity of several orders of magnitude (e.g. approximately four orders of magnitude in **publication 2**) to an AFI phase with monoclinic structure [18, 42]. The temperature-driven MIT/IMT is hysteretic and therefore it is classified as a first-order phase transition including phase coexistence during the transition (see Sec. 1.3). Con-

sidering the band structure of V_2O_3, one has to take into account crystal field splitting by trigonal distortion of the oxygen octahedra surrounding vanadium ions, which lifts the degeneracy of vanadium d orbitals [43–47]. The process of phase transition has to be considered as a cooperative effect between lattice and electronic degrees of freedom and is classified as a bandwidth-controlled Mott transition [11, 18]. According to this, the structural phase change (during MIT from corundum to monoclinic structure) was recently found to be coupled robustly to the electronic Mott transition [48]. Nevertheless, the complex interplay between many degrees of freedom during the MIT/IMT in V_2O_3 is still subject of ongoing research [49–51].

Taking into account the strong coupling between lattice and electronic degrees of freedom, it is not surprising, that V_2O_3 thin films grown on substrates are very susceptible to the influence of strain caused by lattice mismatches between thin film and substrate. By strain engineering, the MIT temperatures can be shifted: compressive strain along the c-axis raises the transition temperature in comparison to the bulk [52–55], tensile strain along the c-axis decreases the MIT temperature [53]. V_2O_3 thin films grown on r-cut sapphire are close to the c/a-ratio of the bulk and show only slightly higher transition temperatures compared to the bulk.

Trastoy *et al.* established a procedure to grow V_2O_3 thin films on r-cut sapphire with a thermal quenching step, i.e. decreasing the temperature quickly after growth in order to freeze the oxygen stoichiometry, yielding sharp MIT/IMT with resistivity changes of several orders of magnitude [56]. These desirable properties were realized in the V_2O_3 thin films for **publication 2** and **3**.

The study of McLeod *et al.* [57] marks a milestone in the context of imaging the MIT/IMT in V_2O_3: the researchers were able to image the spontaneous temperature driven phase separation in a 300-nm-thick V_2O_3 thin film via scanning near field optical microscopy (SNOM) (see Fig. 1.4(a)). This imaging technique uses the near-field signal of backscattered infrared laser light, which is focused on an atomic force microscopy tip. The tip is scanned across the sample surface. SNOM allows for imaging the surface optical properties with high spatial resolution, which is solely determined by the tip size – in this study, the authors estimated a spatial resolution of 25 nm. As depicted in a exemplary false color image in Fig. 1.4(b), they observed a strain-induced herringbone domain pattern of clearly distinguishable metallic (red) and insulating (blue) domains, respectively. Due to different absorption coefficients of the metallic and insulating phases [45, 47, 58], it is possible to observe domain patterns via optical microscopy at appropriate wavelengths (see also Sec. 1.5). For this reason, we can distinguish between the metallic and the insulating phase in our optical imaging studies not only in V_2O_3 thin films (**publication 2** and **3**), but also in nickelate thin films (**publication 1**).

1.2.2 Charge transfer insulators

Charge transfer insulators are representatives of a material class, which is described by an extension of the Hubbard model. In compounds like the perovskite rare-earth nickelates, the d-orbitals of the transition metal ions have strong overlap with p-orbitals of the O^{-2} oxygen ion ligands – one cannot neglect the p-d hopping of electrons. Typically, for
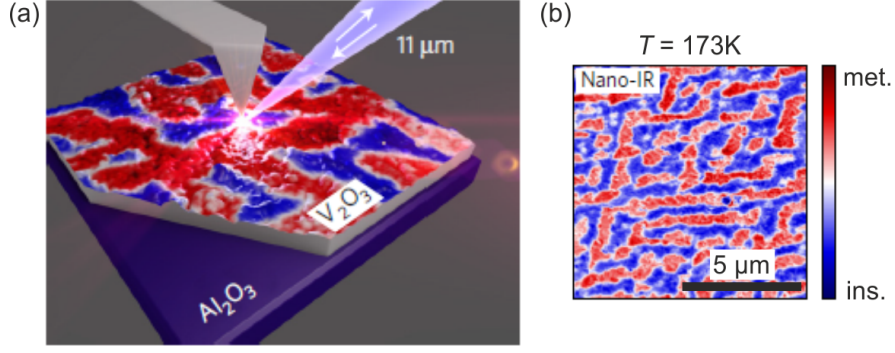
Figure 1.4: (a) Schematic of scanning near field optical microscopy (SNOM). Infrared laser light (wavelength $11\,\mu$m) is focused on the tip of an atomic force microscopy cantilever. Incoming and backscattered light is indicated by the arrows in the beam. (b) Generic example of the imaging of the phase separation in V_2O_3 during IMT via SNOM. Blue regions are in the insulating state, red regions in the metallic state. The domains form a strain-induced herringbone pattern. Used with permission of Springer Nature BV, adapted from [57]; permission conveyed through Copyright Clearance Center, Inc.

example in perovskite RNiO$_3$ (R represents a rare-earth element) compounds we find Ni^{3+} cations in the center of O$_6$ octahedra. Without taking into account distortions like tilting or rotating the octahedra, there are Ni-O-Ni-angles of $180\,^\circ$. Fig. 1.2(c) shows the directional nickel $d_{\mathrm{x}^2-\mathrm{y}^2}$ orbital with surrounding oxygen p-orbitals in the x-y-plane. Any deformation of the NiO$_6$ octahedra strongly influences the interplay between charge, spin and orbital degrees of freedom and consequently, determines the properties of the compound. The standard Hubbard model neglects p-d electron correlation (t_{pd} in Fig. 1.2(c)) and allows only d-d-hopping with energy cost U. Taking into account the oxygen p-orbitals, hopping of a p electron into the d-band producing a hole $\underline{L}$ in the ligand p-band and $n+1$ electrons in the metal d-band, is energetically the most favourable process:

$$d^n \longrightarrow d^{n+1}\underline{L} \, , \tag{1.2.5}$$

with a charge transfer energy cost

$$\Delta E = \Delta_{CT} \, , \tag{1.2.6}$$

which is the charge transfer energy gap. For the case $U \ll \Delta_{CT}$, the material is classified as a Mott-Hubbard insulator, whereas for the opposite case $U \gg \Delta_{CT}$, the material is classified as charge transfer insulator (Fig.1.2(d)). It is possible, that Δ_{CT} is small or even negative, which is the case for transition metal ions with high valence like Ni^{3+} [59, 60]. According to the ZSA-scheme (introduced by Zaanen, Sawatzky and Allen) to distinguish between Mott-Hubbard and charge transfer insulators [61], rare-earth nickelates are predicted to be metallic at low temperatures, which is wrong except for

Figure 1.5: Phase diagram of the rare-earth nickelate family $R\text{NiO}_3$. Note the double x-axis with Ni-O-Ni-angle and the corresponding Goldschmidt tolerance factor t, which is associated with the rare-earth ionic radii. MIT temperatures are marked with black squares, Néel temperatures with black circles. The insets show the crystal structures of the different phases, respectively. Used with permission of IOP Publishing, Ltd., adapted from [37]; permission conveyed through Copyright Clearance Center, Inc.

LaNiO_3. Mizokawa *et al.* extended the ZSA-scheme to negative values of Δ_{CT} [60] and classified rare-earth nickelates as negative charge transfer insulators.

The rare-earth nickelates NdNiO$_3$ and SmNiO$_3$

The compounds NdNiO_3 and SmNiO_3 are as device materials in **publication 1** of particular interest in this work. Figure 1.5 shows the phase diagram of the perovskite rare-earth nickelate family $R\text{NiO}_3$ as function of temperature, the Ni-O-Ni angle and, equivalently, the Goldschmidt tolerance factor [62], which is a measure for the ionic radii of the rare-earth cation, respectively. It indicates three distinct phases for SmNiO_3: PM with orthorhombic crystal structure at high temperatures, PI and AFI both with monoclinic structure at lower temperatures. For NdNiO_3, the MIT temperature and Néel temperature coincide – the transition occurs from PM in orthorhombic structure to AFI in monoclinic structure. As mentioned in Sec. 1.2.2, the properties of a specific $R\text{NiO}_3$ compound is strongly dependent on the distortion of the NiO_6 octahedra, because of different overlaps of the strongly directional nickel d- and oxygen p-orbitals. Additionally, the insulating phase in the monoclinic strucure shows a Ni-O bondlength disproportionation resulting in a breathing mode, which means that two different Ni-O-bondlengths, i.e. a short one and a long one, are realized in a checkerboard arrangement in the lattice [63]. The details of the electronic phase transition in rare-earth nickelates is subject of

many theoretical studies, which unveiled this bondlength disproportionation as a key feature, that controls the MIT [64–71].

The thermally driven MIT/IMT in $NdNiO_3$ exhibits a pronounced hysteresis, which is a sign of a first-order transition [18, 72]. In $SmNiO_3$, close to the transition temperature, there is a small hysteresis in the resistance R vs. temperature T curve as well [73].

Considering thin films of $NdNiO_3$ and $SmNiO_3$, the MIT/IMT temperatures can be controlled by epitaxial strain engineering [74]. Depending on the lattice mismatch with the substrate material, the transition temperature of $NdNiO_3$ can be shifted towards lower temperatures – with increasing strain, it can be even suppressed completely [75].

Generally, $RNiO_3$ thin film samples exhibit lower MIT temperatures compared to bulk samples (Fig. 1.5), e.g. $NdNiO_3$ at $\sim 120\,K$ and $SmNiO_3$ at $\sim 400\,K$ in **publication 1**. $NdNiO_3$ has a sharp MIT/IMT with a large resistivity contrast of around two orders of magnitude, whereas $SmNiO_3$ shows a smooth transition with a resistivity drop of only one order of magnitude.

1.3 Thermodynamical aspects of phase transitions in strongly correlated insulators

Due to the fact, that neuromorphic devices based on strongly correlated insulators are operated in a state of criticality (see Sec. 1.1), i.e. close to the onset of phase transitions, their behavior is affected by the thermodynamics of phase transitions. First of all, it is recognized, that in V_2O_3 as well as in the rare-earth nickelates $NdNiO_3$ and $SmNiO_3$ at the MIT/IMT, several phase transitions are coupled (see Sec. 1.2.1 and Sec. 1.2.2). The details of the coupling between these transitions remain elusive, but the hysteresis in the $R(T)$ curves indicates a first-order nature of the MIT/IMT. In terms of the phenomenological Landau theory of phase transitions, there is an ordered low-temperature phase (insulating) and an unordered high-temperature phase (metallic) [76, 77]. The theory introduces an order parameter and a critical temperature T_c, where the phase transition happens. The free energy of a system is expressed as a Taylor expansion in the order parameter.

Figure 1.6 shows generic free energy vs. order parameter landscapes for different temperatures of a first-order phase transition. A first-order transition inherently exhibits metastable states (local minima of the free energy), which are separated by an energy barrier from the stable state (global minimum of the free energy). Thermodynamically, this is the reason for hysteresis effects including phase coexistence (or else phase separation) during first-order phase transitions. Figure 1.6 depicts metastability during an IMT at three exemplary temperatures. For temperatures $T \ll T_c$, the sample is entirely in the insulating state. Coming closer to T_c by increasing the temperature, as depicted in Fig. 1.6(a), a metastable metallic state in the form of a local minimum occurs. With this, the phase coexistence regime is entered. By further increasing the temperature, passing T_c, where both minima have the same free energy value (Fig. 1.6(b)), the former local minimum becomes global for $T > T_c$ (Fig. 1.6(c)). For even higher temperatures, the metastable state vanishes and the sample is homogeneously metallic.
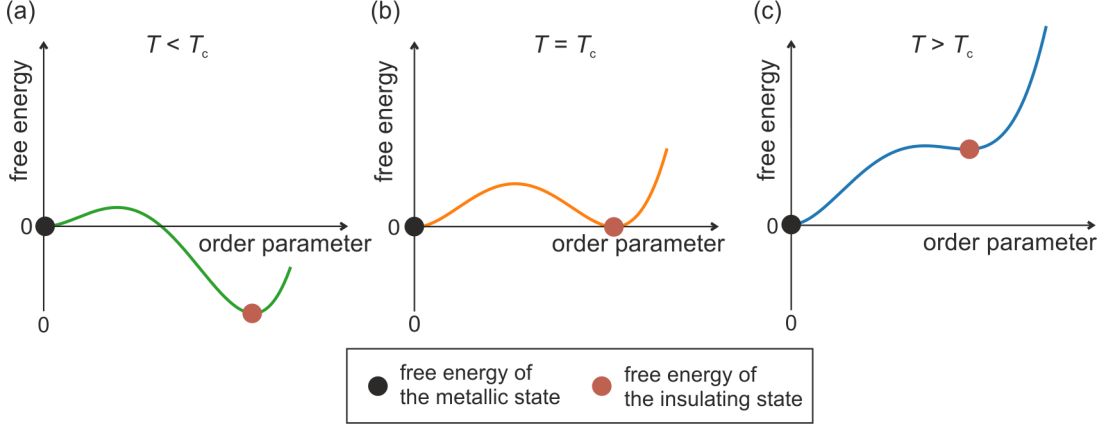
Figure 1.6: Metastability as characteristic feature of a first-order phase transition. The graphs show generic Landau free energy vs. order parameter landscapes for different temperatures during an IMT. (a) $T < T_c$. (b) $T = T_c$. (c) $T > T_c$.

Phase coexistence was theoretically predicted in strongly correlated insulators [78–80] and is well documented for the phase transitions in vanadates [57] as well as in nickelates [81, 82]. It is recognized, that phase separation is connected to a competition between short- and long-range interactions, which determines also the shape of domain patterns [83]. Striped domain patterns for example are found to be dominated by elastic long-range interactions arising from lattice mismatches with the substrate [84, 85].

The thermodynamical description of MIT/IMT in strongly correlated insulators is subject of ongoing research [86–88]. Kotliar *et al.* introduced a Landau-type free energy for Mott transitions

$$f(\eta) = h(T)\eta + p(T)\eta^2 + c\eta^4 , \qquad (1.3.1)$$

where η is the order parameter, $h(T) = h_1 \cdot \frac{T-T_c}{T_c} + h_2$, $p(T) = p_1 \cdot \frac{T-T_c}{T_c} + p_2$, T is the temperature, T_c is the critical temperature and h_1, h_2, p_1, p_2 and c are constants [87]. This approach is established in literature [21, 25], and we used it in **publication 1** and **3** as well. Unfortunately, the Landau approach to Mott transitions is lacking an obvious quantity as order parameter. Qualitatively, one could call it "metallicity" [87], theoretical assumptions are for example the propagation coherence of single-particle excitations [89] or the density of sites with double electron occupancy [86].

Besides this, there are intricate details in the thermodynamical description of strongly correlated insulator thin films. The study of Post *et al.* defies the established binary classification of first- or second-order transitions in the Landau theory and assumes a coexistence of both first- and second-order phase transitions in NdNiO$_3$ [90]. The researchers observe nanoscale domain walls in the insulating state, that undergo a second-order phase transition additionally to the first-order MIT/IMT. They expect coupling of charge and magnetic order parameters to account for this. Additionally, another study suggested the coupling of two order parameters to describe the coupled structural and electronic phase transitions in rare-earth nickelates in terms of Landau theory [71].

Recent studies indicate signs of a spinodal decomoposition, describing the phase separation of a binary mixture of phases in MIT/IMT in strongly correlated insulators [91, 92]. Compatible with that and according to the SNOM imaging study of McLeod *et al.* (see Sec. 1.2.1), the observation of characteristic herringbone domain patterns during the phase transition in V_2O_3 unveils a strong similarity to the numerical solutions of the Cahn-Larché equation, which describes a spinodal decomposition in presence of elastic stress [93].

1.4 Resistive switching in strongly correlated insulators

In order to utilize devices based on strongly correlated insulators in the scope of neuromorphic computing, one takes advantage of resistive switching, i.e. triggering the MIT/IMT by use of a stimulus. Most commonly, electrical stimuli like currents or voltages are applied to devices based on strongly correlated insulators [94–101]. This means, that by ramping up a current or voltage, the resistivity of the device is decreasing abruptly, when a certain threshold is reached. In Mott insulator research, there is an ongoing controversial discussion for years, whether this breakdown of the resistivity is caused purely electrical (electric-field-driven) or electrothermally [102, 103]. Several suggestions were made for purely electrical switching: at very strong electric fields ($\geq 100\,\mathrm{MV/m}$) Landau-Zener tunneling across the Mott gap gives rise to an increase of the concentration of delocalized charge carriers [104–108]. However, after showing resistive switching in Mott insulators at considerably lower electric fields [109], other suggestions were made like midgap tunneling [110, 111], an electric-field-driven collapse of the Mott gap [112] or a spatially inhomogeneous metal-insulator mixed state leading to resistive switching [113].

On the other hand, one has to take into account an electrothermal origin of the resistive switching. Note, that this explanatory approach does not refer directly to Mott-Hubbard physics, however indirectly, because it is based on the strong temperature dependence of the resistivity. Instead, it focuses on more general phenomena like self-heating and electrothermal instability [114–117]. By applying these ideas to devices based on strongly correlated insulators, the strong temperature dependence of the device resistivity during the MIT/IMT is crucial (see Fig. 1.7(a)). Let's imagine a simple two-terminal device, i.e. a strongly correlated insulator thin film between two electrodes in a current-biased measurement arrangement like in Fig. 1.7(c). The thin film is in the insulating state, but at a bias temperature T_b close to the Mott transition. When the current is ramped up, it causes Joule heating, that increases the overall device temperature. The slope of the current-voltage characteristics (IVC) at low current values in Fig.1.7(b) represents the electrical conductance $1/R$ of the insulating state. Small spatial inhomogeneities in current density lead to variations in temperature, which can lead in turn to drastic variations in local resistivity. Currents above a certain threshold can cause a runaway effect, in which the temperature dependence of the resistivity acts as a positive feedback mechanism, resulting in a strong current concentration into a conductive (metallic) filament connecting the electrodes (voltage breakdown from point A to point B in Fig. 1.7(b)).
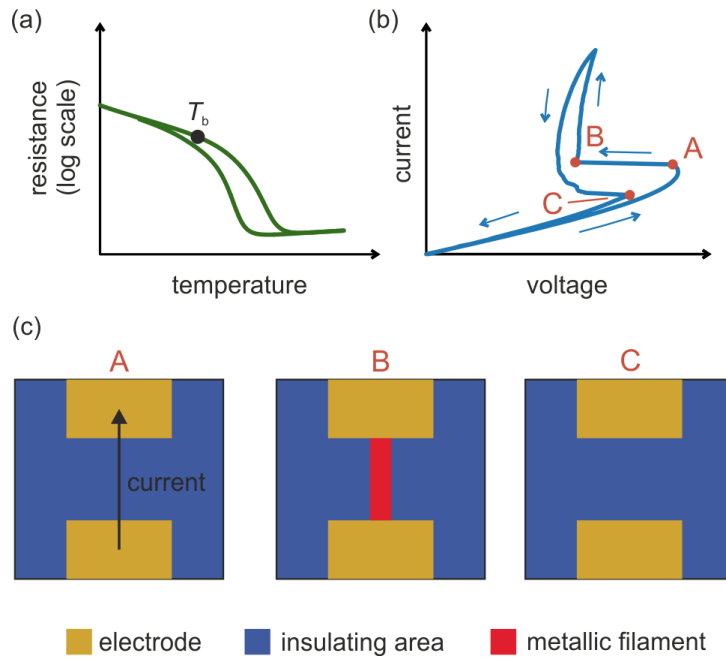
Figure 1.7: Volatile resistive switching. (a) Generic $R(T)$ curve of a two-terminal device based on a strongly correlated insulator (see (c)) with a marked bias temperature T_b in the warming branch close to the IMT. Consequently, at $T = T_b$ the sample is in the insulating state. (b) Generic current-biased current-voltage characteristic (IVC) of the sample at temperature T_b. The capital letters mark characteristic points: Point A is just before the voltage breakdown, point B is just after the voltage breakdown. Point C marks, where the sample just switched back into the initial fully insulating state. (c) Simplified sketches of a two-terminal device during the IVC in (b). The capital letters correspond to the characteristic points in (b).

That is the result of an electrothermal instability accompanied with a region of negative differential resistance just before the resistive breakdown. The switched configuration is sustained by Joule heating, focusing current into the filament and keeping surrounding areas in the insulating state. By decreasing the current, at a certain threshold value, this arrangement becomes unfavorable at point C in Fig.1.7(b) and the device returns to the initial insulating state – obviously, the IVC returns to the initial slope representing the electrical conductance of the insulating state. In this interpretation, the mechanism of resistive switching is a result of spatially inhomogeneous redistribution of current and temperature.

Electrothermal breakdowns in devices based on strongly correlated insulators were suggested and demonstrated by measuring the filament temperature locally [96], by performing fast voltage-pulse measurements [98] or by voltage-induced IMT in vanadium dioxide [118]. However, in order to suppress the impact of self-heating effects, scaling down the device dimensions revealed electronic contributions to the resistive switching in V_2O_3 [103]. A recent study indicates purely non-thermal resistive switching in V_2O_3 nanowires by field-assisted carrier generation [119].

Additionally, it is reported, that resistive switching in strongly correlated insulators can be externally triggered via excitation by laser light [120–123]. Optical stimulation can be used to tune the voltage thresholds of resistive switching [124] and to control the frequency of relaxation oscillators in vanadium dioxide devices [125]. There are numerous studies indicating non-thermal control of resistive switching via ultra-fast optical pump-probe experiments [126–132].

In most of the mentioned studies within this section, integral measurements of the total device resistivity are performed to get information on the resistive switching. However, inherently, the devices feature strongly inhomogeneous current and temperature distributions – a situation which explicitly demands for spatially resolved imaging techniques [57].

Independently from the exact physical explanation of the origin of the triggered change in resistivity, one can distinguish between volatile and non-volatile resistive switching [2, 99]. Volatile resistive switching means, that the sustain of the switched state is dependent on the duration of external stimuli and the initial state is recovered, when these stimuli are removed [25, 133]. In concreto, in Fig. 1.7 we observe a percolative conducting filament formation between two electrodes, when a certain threshold current is reached. This filament vanishes, when the current falls below a threshold, which does not have to be the same as for its formation process. The spatial and temporal dynamics of volatile filament formation are subject of ongoing research and it is found, that their characteristic times of filament nucleation and relaxation are on the order of nanoseconds [133–135].

On the other hand, non-volatile resistive switching describes a change in device properties, which is at least semi-permanent [136–138]. Examples for non-volatile resistive switching are electroforming or electromigration (e.g. ion migration) processes induced by large electric fields ($\sim \mathrm{MV/cm}$), that form conductive filamentary structures as well [139, 140]. These filaments can be controlled by electric field pulses in order to interrupt or reconnect conducting filaments.

There are also attempts to achieve non-volatility with strongly correlated insulators, that naturally exhibit volatile resistive switching, for example in hybrid V_2O_3 devices using controllable ferroelastic strain [141] or by introducing and removing oxygen vacancies in VO_2 devices [142]. Taking advantage of the first-order-nature of the MIT/IMT in strongly correlated insulators (see Sec. 1.3), it is possible to prepare non-volatile states in multistate resistive switching devices [143–145].

1.5 Methods

In the publications of this thesis, we investigate planar thin film devices with simple two-terminal designs. The electric switching fields of our materials under investigation are considerably smaller than for instance in electroforming- or elecromigration-devices (see Sec. 1.4). This allows for devices with larger scales, i.e. electrode spacing of $\sim 20\,\mu$m. Planar devices of these dimensions perfectly concede optical widefield imaging of the entire area of interest.

As already mentioned in Sec. 1.2.1, it is possible to distinguish the metallic from insulating phase in V_2O_3 as well as in $NdNiO_3$ and $SmNiO_3$ via optical microscopy. The band structures of these materials lead to different reflectivities of the phases, which serves as contrast mechanism in our imaging studies. This explains the unexpected effect, that the metallic phases have lower reflectivities at 532-nm-illumination wavelength compared to the insulating ones [45, 47, 58].

The experimental data for my contributions to the publications of this thesis were acquired with a combined low-temperature widefield and scanning laser polarizing microscopy setup, which is an unique instrument in-house built at the Eberhard Karls Universität Tübingen [146, 147]. Note, that the possibility of the acquisition of high-resolution photomicrographs simultaneous to electric transport measurements makes this tool very powerful in the research field of local phase transitions and resistive switching in strongly correlated insulators.

Figure 1.8 shows a simplified schematic of the microscope setup. This modular experimental setup is highly versatile as it provides different imaging modes, that are selectable *in situ* (via a removable mirror). The illumination of the widefield microscope is realized in a Köhler illumination scheme with a monochromatic LED with a wavelength of 532 nm as light source. After passing a beam splitter and being reflected at the removable mirror, the light is focused onto the sample by the objective lens. The sample is mounted on the coldfinger of a liquid Helium continuous flow cryostat providing a temperature range of 4.2 K to 300 K. The objective lens has a high numerical aperture (NA = 0.8) and allows for a high working distance of 1 mm. Wire-bonded samples can easily be imaged within this arrangement. A low noise sCMOS camera serves as detector of the widefield microscope. The entire widefield microscope is polarization sensitive.

The laser scanning microscope illumination is realized with a laser diode of 405 nm wavelength. The collimated laser beam is scanned across the sample by a fast steering mirror and passes the objective lens, which is shared by both imaging modes. The focused laser beam has a spot diameter of 322 nm ($1/e^2$ criterion, assuming a Gaussian
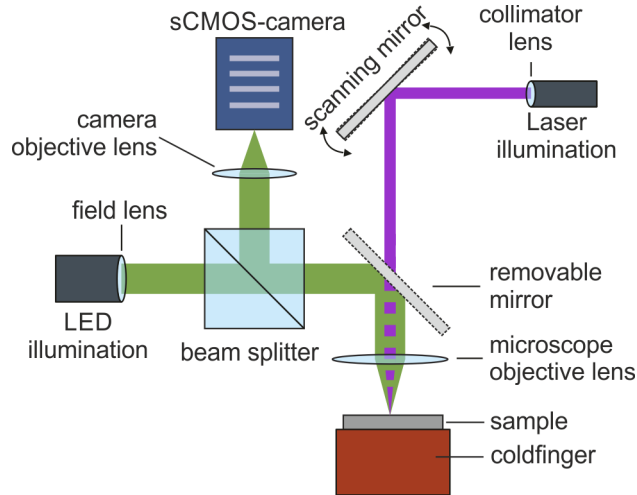
Figure 1.8: Simplified schematic of the combined low-temperature widefield and laser scanning microscopy setup. Figure from supplemental material of **publication 3**.

beam profile) on the sample surface. In the context of the publications of this thesis, the scanning laser microscope is not used as imaging mode, but for focused-laser-irradiation in **publication 3**. This is the reason, why the detector unit as well as the polarization sensitive components of the scanning laser microscope are neglected in Fig. 1.8. The field of view of $500 \times 500\,\mu\mathrm{m}^2$ is identical for both microscopy modes. More details about the experimental setup can be found in Refs. [146, 147].

1.6 Addressed research questions

In the publications of this thesis, relevant questions in the field of strongly correlated insulator research for neuromorphic applications are addressed. One of the most fundamental challenges is the understanding of the resistive switching mechanism in strongly correlated insulators (see Sec. 1.4). Due to the fact, that the electronical transitions are coupled with structural transitions in the materials under test, the question about the impact of the interaction of electronic and structural degrees of freedom on the functionality of devices is raised. This concerns for example the thin film parameters like thickness or epitaxial strain due to lattice mismatch with the substrate material. Moreover, general aspects of the thermodynamical description of the Mott transition remain elusive (see Sec. 1.3). Especially the first-order nature of the transition comprises mostly neglected phenomena like metastability in these materials, which very likely can be fruitfully used for applicable devices. Spatially resolved imaging techniques can yield important information, especially in samples with locally inhomogeneous current or temperature distributions and domain configurations during the phase coexistence regime of first-order phase transitions.

By achieving definite progress in the scope of these big research questions in the publications of this work, we try to contribute to the knowledge, which is key to control the properties of possible devices for neuromorphic applications.

In **publication 1**, we addressed the question of characteristic length scales of conducting filaments in resistive switching devices based on strongly correlated insulators, namely on two members of the rare-earth nickelate family, $NdNiO_3$ and $SmNiO_3$. We investigate the spatial dynamics of resistive switching as an aspect, which has been mostly unnoticed so far. The question of key parameters, that determine the length scales was addressed and the resistivity contrast between metallic and insulating states was identified to be a key property, that sets the size of the conducting filament. With this, we could contribute to complete the picture of filament nucleation dynamics, which is very important for device applications and miniaturization.

In **publication 2**, we addressed a research question at the core of the mechanism of resistive switching in strongly correlated insulators: is the resistive switching caused purely electrical (electric field driven) or eletrothermally? Moreover, the fundamental question about the details of the coupling between lattice and electronic degrees of freedom in V_2O_3 thin films is touched. Indeed, we find signs of electrothermal resistive switching in that study. Further, we could establish a link between the strain-induced herringbone domain pattern and the formation of a metallic filament and support the experimental results with a numerical model. Hence, this is a contribution to the fundamental understanding of resistive switching in devices based on strongly correlated insulator thin films.

Publication 3 is a research contribution in the field of optically induced phase transitions by focused laser beam scanning in V_2O_3 thin films. This work strongly involves thermodynamical aspects of the Mott transition. In particular, the effects of its first-order nature on the electronic properties remained mostly unaddressed so far. By discovering the possibility to drive metastable states during the electronic first-order phase transition into stable ones, i.e. quenching metastability, this paper contributes to the complex and controversial discussion about thermodynamics in strongly correlated insulators (see Sec. 1.3). In contrast to ultrafast pump-probe experiments, we can trigger phase transitions in a quasi-static arrangement and show a novel, likely non-thermal method to set or reset memristive devices locally and, consequently, erase the thermal history of a strongly correlated insulator thin film.

Chapter 2

Summary of the publications

This chapter gives summaries of the appended publications. Each summary is followed by a description of own author contributions.

2.1 Publication 1: Characteristic length scales of the electrically induced insulator-to-metal transition

In this publication, we analyzed and compared the filament formation due to volatile resistive switching in planar two-terminal thin film devices based on the rare-earth nickelates $NdNiO_3$ (NNO) and $SmNiO_3$ (SNO). We studied characteristic length scales of the conducting filaments and find, that the sharper the resistive switching and the larger the resistive drop is, the smaller are the filaments, and the higher is the current density within them.

In order to address the issue of characteristic length scales, we use two complementary types of microscopy: widefield optical microscopy and scattering-type scanning near-field optical microscopy (s-SNOM). Widefield microscopy allows for systematic studies over a large temperature range, but is limited by diffraction (spatial resolution $\sim 500\,\mathrm{nm}$), whereas s-SNOM (see short description in Sec. 1.2) provides high spatial resolution ($\sim 20\,\mathrm{nm}$), but is limited in temperature flexibility.

We fabricated two-terminal microdevies from both materials under investigation. These materials (charge transfer insulators) both undergo MIT/IMT, but show important differences in the properties of the electrical phase transitions, as depicted in Fig. 2.1. NNO provides a sharp temperature-driven IMT at $\sim 120\,\mathrm{K}$ with a resistivity drop of more than two orders of magnitude, while SNO shows a smooth temperature-driven IMT at $\sim 400\,\mathrm{K}$ with a resistivity change of roughly one order of magnitude.

By applying large enough currents, the IMT is triggered and we acquire optical images of the device *in situ*. Taking advantage of the difference of reflectivities of the metallic and insulating phases across the IMT, we are able to visualize the conducting filament between the electrodes.

Figure 2.2 shows the results of the widefield microscopy study. In Fig. 2.2(a) and (d) we show voltage V vs. current I characteristics of NNO and SNO microdevices at three different temperatures below the IMT, respectively. Electrically induced resistive switching by formation of a percolative conducting filament happens after reaching a certain threshold while ramping up the current. At this point, the voltage breaks down
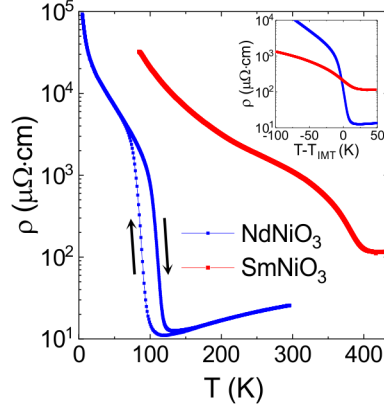
Figure 2.1: Resistivity ρ vs. temperature T relations of NNO (blue) and SNO (red) thin film microdevices. Inset: Resistivity vs. temperature $T - T_{\mathrm{IMT}}$. Only the warming branches are shown, respectively. Figure from appended **publication 1**. Copyright © 2023 by American Physical Society. All rights reserved.

and we can observe a conducting filament (Fig. 2.2(b) and (e)). We can state, that filaments in the NNO case are narrower and sharper than for SNO, and at a fixed bias current $I = 20\,\mathrm{mA}$, the filament widths decrease with decreasing temperature. The Figs. 2.2(c) and (f) show the filament widths in NNO and SNO for more temperatures, respectively.

The s-SNOM images at $T = 18\,\mathrm{K}$ (Fig. 2.3(a)) show single and intense filaments percolating between the electrodes. Complementary to the widefield microscopy study, this imaging technique unveils multi-filament configurations for NNO at $T = 70\,\mathrm{K}$ (Fig. 2.3 (b)). In accordance with the widefield images, we see narrower filaments at lower temperatures at fixed bias currents.

In order to determine the parameters controlling the length scales of the filaments, a numerical model, i.e. a two-dimensional resistor network model was set up. This model is able to reproduce the main features of the experimental results with only a few parameters, namely the resistivity contrast, i.e. the ratio of the insulating (ρ_{ins}) and metallic (ρ_{met}) phase resistivities, and the thermal conductivity of the substrate.

For $\rho_{\mathrm{ins}} \gg \rho_{\mathrm{met}}$, the current is strongly focused into the filament and keeps the regions outside the filament cold. By comparing the resistivity contrast of NNO and SNO, the latter shows a smaller change in resistivity, resulting in wider filaments.

However, considerations on the thermal conductivity of the substrate point in the same direction, because it decreases with increasing temperature. This means, the substrate can transport heat more efficiently at lower temperatures. In turn, this keeps the surrounding areas of the filament cold and the current is focused into a confined filament.

Experimentally, it is impossible to disentangle the thermal properties of the substrate from the contribution of the resistivity contrast across the IMT. In order to face this problem and to verify the resistivity contrast to be a key parameter for the filament length scale, we compare two NNO samples with different IMT qualities (i.e. different
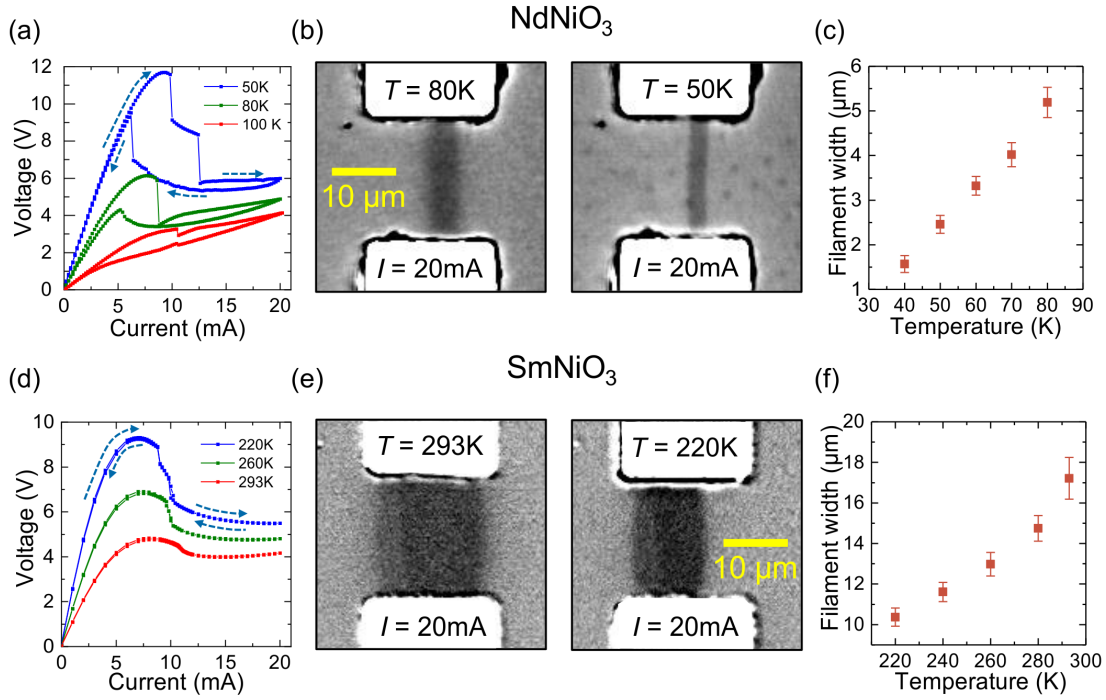
Figure 2.2: Connection between resistive switching properties and filament size. (a) and (d) Voltage vs. current curves for NNO and SNO microdevices, respectively. Several temperatures are plotted for each material. (b) and (e) Widefield optical microscopy images of filaments in NNO and SNO, respectively. $I = 20\,\text{mA}$ for all four images. Two different temperatures are shown for each material. For the NNO images, reflectivity was normalized using a region far from the gap. For SNO, differential images are shown, where at each point, the reflectivity at $I = 0\,\text{mA}$ is subtracted. (c) and (f) Filament width vs. temperature at $I = 20\,\text{mA}$. Figure from appended **publication 1**. Copyright © 2023 by American Physical Society. All rights reserved.
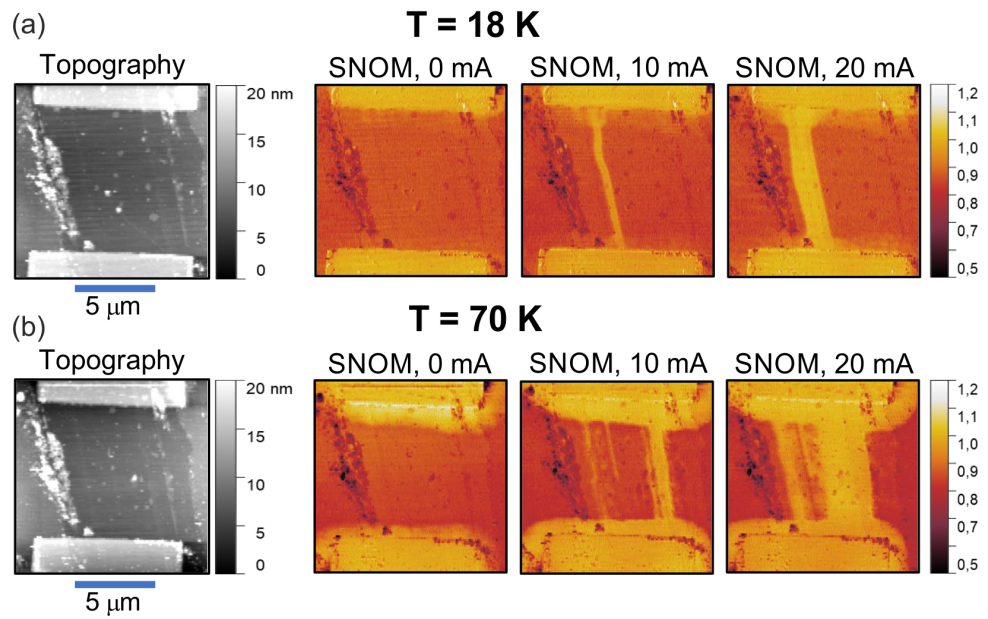
Figure 2.3: High-resolution scattering-type scanning near-field optical microscopy (s-SNOM) imaging and presence of multiple percolating filaments. (a) and (b) Topography and s-SNOM amplitude images for NNO microdevices at $T = 18$ and $70\,\mathrm{K}$, respectively. The s-SNOM signal was normalized using the Pt electrode as reference. s-SNOM data for three different current values is shown. Figure adapted from appended **publication 1**. Copyright © 2023 by American Physical Society. All rights reserved.

resistivity contrasts) on the same substrate material, resulting in a significantly less confined filament for the sample with smaller resistivity change across the IMT.

Concluding this study, we find that the length scales of a conducting filament in NNO and SNO microdevices are controlled by the resistivity contrast of the specific material and the thermal conductivity of the substrate. These mechanisms are simple and general and could be very likely applicable to other resistive switching materials.

Contributions

This publication was a collaboration with the groups of J.-M. Triscone and A. B. Kuzmenko at the University of Geneva, and M. J. Rozenberg at the Université Paris-Saclay. J. del Valle initiated the study, fabricated the nickelate samples and did precharacterizations. A. Bercher conducted the s-SNOM imaging measurements. R. Rocco set up the numerical model for the study. I improved our measurement setup to study relaxation oscillations in NNO and SNO. I conducted the imaging measurements done in Tübingen with assistance of S. Guénon and F. Tahouni-Bonab and I provided the analysis of this part. According figures were created and corresponding parts of the manuscript were written by myself.

2.2 Publication 2: Imaging of Electrothermal Filament Formation in a Mott Insulator

In this publication, we present both the visualization of the temperature-driven spontaneous phase separation and the volatile resistive switching triggered by electric current in a planar two-terminal V_2O_3 thin film microdevice by optical widefield microscopy. There are clear signs of an electrothermal origin of resistive switching in this case.

We fabricated a 300-nm-thick V_2O_3 thin film microdevice (Fig. 2.4(a)), which shows a hysteretic $R(T)$ relation with a change in resistance of four orders of magnitude in the steep part of the MIT/IMT (Fig. 2.4(b), upper panel). Via optical widefield microscopy it is possible to distinguish between metallic and insulating parts of the sample surface, due to a significant change of reflectivity across the MIT/IMT. Figure 2.4(c) shows examples of a photomicrograph series taken during a complete thermal cycle. It is possible to resolve the thermally driven phase separation, manifesting itself in a characteristic herringbone domain structure. Averaging over an area of interest yields the temperature dependence of the reflectivity, that resembles the hysteretic $R(T)$ relation (green line in Fig. 2.4(b), lower panel). If we plot the local reflectivity of a single point vs. temperature, the first-order nature of the phase transition is unveiled by a discontinuous step (red line in Fig. 2.4(b), lower panel).

This way, it is possible to determine the local MIT and IMT temperatures during one complete thermal cycle, yielding a pixel-map of local transition temperatures. The exact distribution of these temperatures as well as the geometry of the domains differ from cycle to cycle due to different strain distribution in the thin film, whereas the overall domain geometry is reproducible.
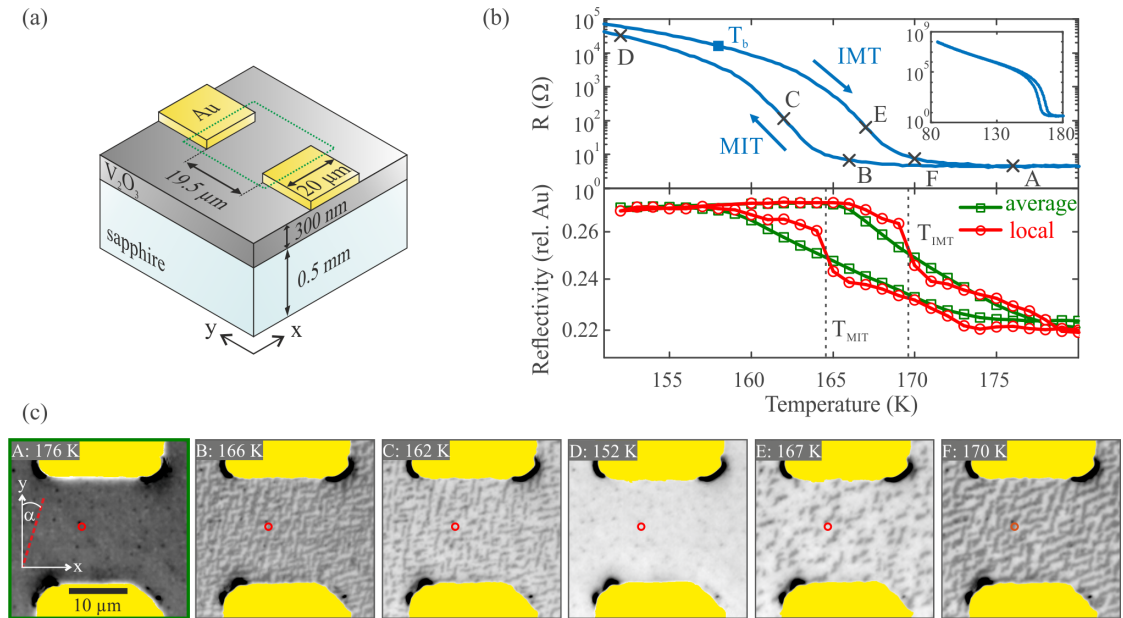
(a)

(b)

(c)

Figure 2.4: (a) A schematic view of the planar V_2O_3 device under investigation. The dotted green line indicates the area of interest (the field of view of the images shown in (c)). (b) Resistively and optically detected MIT/IMT. The upper panel shows the electrical resistance $R(T)$; the arrows indicate the sweep direction of the temperature T. Data points marked by letters correspond to images shown in (c). The inset shows the complete $R(T)$ curve. The lower panel shows the reflectivity versus T of the V_2O_3 film normalized to the reflectivity of the Au electrodes. The green curve represents the average over the area of interest, while the red curve represents the reflectivity of a single pixel at the location indicated by the red circles in (c). The vertical dashed lines indicate the local transition temperatures T_{MIT} and T_{IMT}, determined for the single pixel. (c) A selection of photomicrographs acquired during one thermal cycle. The Au electrodes are indicated by the yellow areas. Figure from appended **publication 2**. Copyright © 2021 by American Physical Society. All rights reserved.
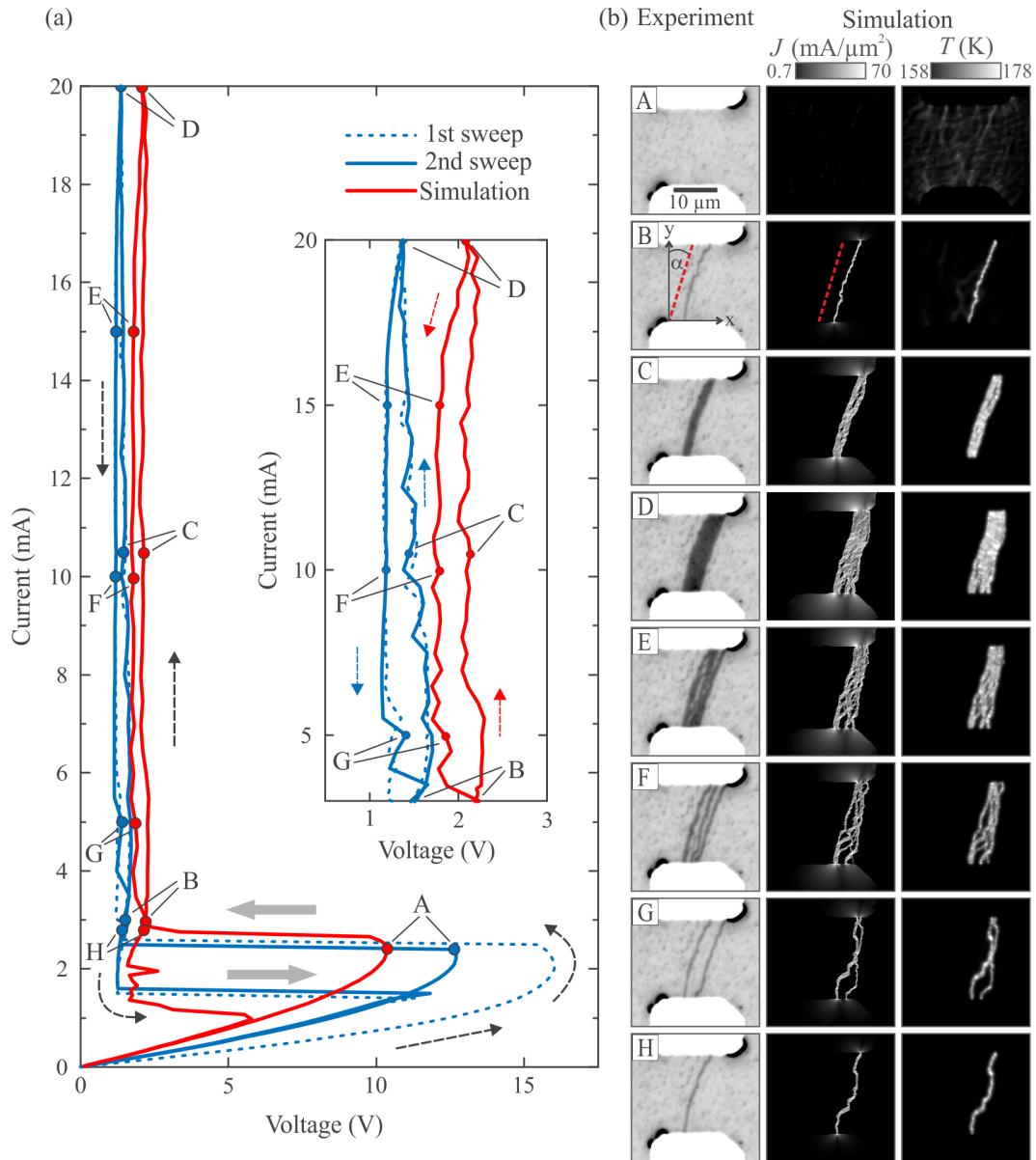
Figure 2.5: The electrical breakdown in a planar V_2O_3 device at a base temperature $T_b = 158\,\text{K}$ at the onset of the IMT. (a) Measured (blue) and simulated (red) IVCs. The letters label data points for which images are shown in (b). The arrows indicate the sweep directions. The thick gray arrows indicate resistive switching to a low- and high-resistance state, respectively. The inset shows a zoom into the high-current section. (b) The left-hand column shows a selection of the photomicrographs acquired during the second current sweep. The middle and right-hand columns show a selection of the simulated spatial distribution of the current density J and the local device temperature T, respectively. Figure from appended **publication 2**. Copyright © 2021 by American Physical Society. All rights reserved.

Figure 2.5(a) shows the electrical transport data with current bias points marked with capital letters. The corresponding photomicrographs are shown in the left-hand panel of Fig. 2.5(b). The current I vs. voltage V characteristics (IVC) follow a specific shape: after a linear low-bias regime, we observe a decrease of the differential resistance, that even leads to back bending of the voltage, i.e. negative differential resistance, followed by an abrupt breakdown of the voltage. By increasing the current further, the voltage remains nearly constant, until the maximum current is reached. During the downsweep of the current, the voltage still remains constant (with a small hysteresis) and jumps back into the high-resistive state abruptly, returning to zero linearly. The abrupt jumps in voltage can be directly correlated with the formation and the disappearance of a conducting filament between the electrodes, which is observable via *in situ* widefield imaging (Fig. 2.5).

There is a strong indication pointing towards an electrothermal origin of the voltage breakdown: it happens at maximum power, not at maximum voltage, i.e. maximum electric field. Nonetheless, there are odd features, that are not explainable solely by the electrothermal hypothesis: first, the filament does not connect the electrodes as short as possible, second, it splits into several branches while decreasing the current and third, there is an unexpected small hysteresis in the low-resistance state at high-bias currents.

For this reason, we developed a numerical model, i.e. a two-dimensional resistor network taking into account the thermal properties of the sample and substrate as well as the experimentally determined values of the local MIT-IMT temperatures T_{MIT} and T_{IMT}. With this approach, the strain-induced variation of the local MIT/IMT is included in the model. The middle and right-hand panels of Fig. 2.5(c) shows the impressive accordance of the model with the experimental results. Remarkably, even the shape and the direction of the filament were reproduced by the model, which indicates, that the filament formation is strongly coupled with the strain distribution in the film.

With these findings, we conclude, that resistive switching in a V_2O_3 thin-film microdevice is induced electrothermally in this case. Furthermore, resistive switching, going along with filament formation, is strongly influenced by local inhomogeneities like strain.

Contributions

This work was a collaboration with the groups of I. K. Schuller at the UC San Diego. Y. Kalcheim fabricated and provided the sample and did characterization measurements. M. Lange supervised and conducted the imaging measurements in Tübingen, analyzed the data and developed the numerical model. S. Guénon wrote the manuscript and took the lead of the entire study. I assisted at the imaging measurements and did parts of the analysis, created and improved the figures of the manuscript.

2.3 Publication 3: Laser-induced quenching of metastability at the Mott-insulator to metal transition

In this publication, we investigated the impact of scanning a focused laser beam across the surface of a V_2O_3 thin-film during the MIT and IMT. During the IMT, mostly the metallic phase is induced, while during MIT, the insulating phase is predominantly induced. This is surprising, because one might expect the main effect of the laser scanning to be heating. We suppose, that the laser scanning drives metastable states during the first-order phase transition into stable states and with that, erases locally the thermal history of the thin film.

We scan a focused laser beam across the surface of a rf-sputtered continuous 300-nm-thick V_2O_3 thin film and acquire photomicrographs before and after the irradiation. The measurement setup is a combined low-temperature laser scanning and widefield microscope, that can be operated either in one or the other mode. Note, that we used the laser scanning mode solely for irradiation in this study – all photomicrographs were acquired by widefield microscopy. We can distinguish metallic and insulating domains by a difference in reflectance of the phases.

Figure 2.6 comprises the striking observation of the study. The capital letters in the $R(T)$ curve in Fig. 2.6(a) indicate the temperatures, at which pristine areas of the V_2O_3 thin film were irradiated by the focused laser beam, as depicted in Fig. 2.6(b). During heating (IMT), predominantly metallic domains are induced (Fig. 2.6(c)), whereas during cooling (MIT) predominantly insulating domains are induced (Fig. 2.6(d)) by laser irradiation. In an additional experiment it was observed, that the resistivity of a V_2O_3 thin film microbridge changes significantly after laser irradiation.

In order to analyze the effect more quantitatively, we modified the laser irradiation procedure to determine power thresholds for laser-induced phase changes. It was found, that the heating branch is more sensitive to laser irradiation than the cooling branch. During the MIT, the required laser power to induce phase changes is considerably smaller than during the IMT. Further, the temperature range, in which laser-induced phase transitons are possible, is smaller during the MIT in comparison with the IMT.

Figure 2.7(a) and (b) show the temperature dependence of the filling factors, i.e. the ratio between the surface area of a particular laser-induced phase and the total surface area. The main message is manifested quantitatively here: the major amount of domains switches from insulating to metallic in the heating branch (Fig. 2.7(a)) and vice-versa in the cooling branch (Fig. 2.7(b)). Additionally, in both cases there is a minor phase (insulating at the IMT and metallic at the MIT) induced as well. In Fig. 2.7(c) we compare the filling factors of the insulating phase before and after laser irradiation. The before-irradiation curves show a hysteresis resembling the shape of the $R(T)$ curve. After irradiation both the heating and cooling curve are almost identical for temperatures at 168 K and below.

Discussing these results, one has to take into account the complexity of the phase transition in V_2O_3. There are three coupled phase transitions: the electronic Mott-Hubbard transition, a magnetic transition from paramagnetic to antiferromagnetic and
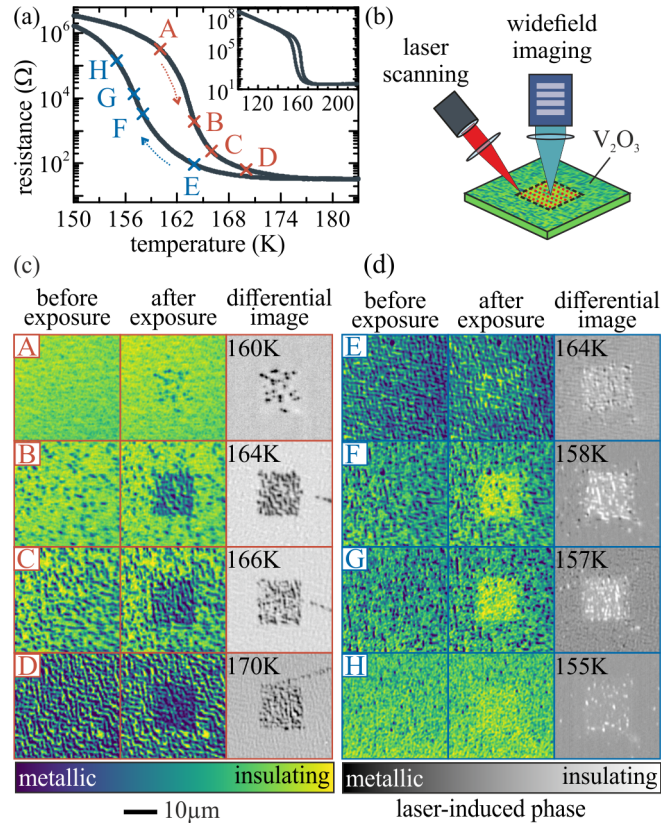
Figure 2.6: (a) Zoom into the phase transition region of the $R(T)$ curve. The red and blue dashed arrows indicate the heating and cooling branch, respectively. Inset: Full $R(T)$ curve of the V_2O_3 thin film sample under investigation with same units as in the main graph. The capital letters mark the set-temperatures in one thermal cycle, at which separated squares in the V_2O_3 thin film were irradiated using the laser scanning mode. (b) Simplified schematic of the measurement setup. Photomicrographs are acquired by widefield microscopy before and after laser scanning within the dashed square of pristine areas. (c) Photomicrograph series demonstrating the laser scanning irradiation effect acquired during one heating run. For the differential images, the image before laser irradiation was subtracted from the image after scanning. The image contrasts were optimized for every temperature. (d) Photomicrograph series acquired during cooling, analogous to (c). Figure from appended **publication 3**.
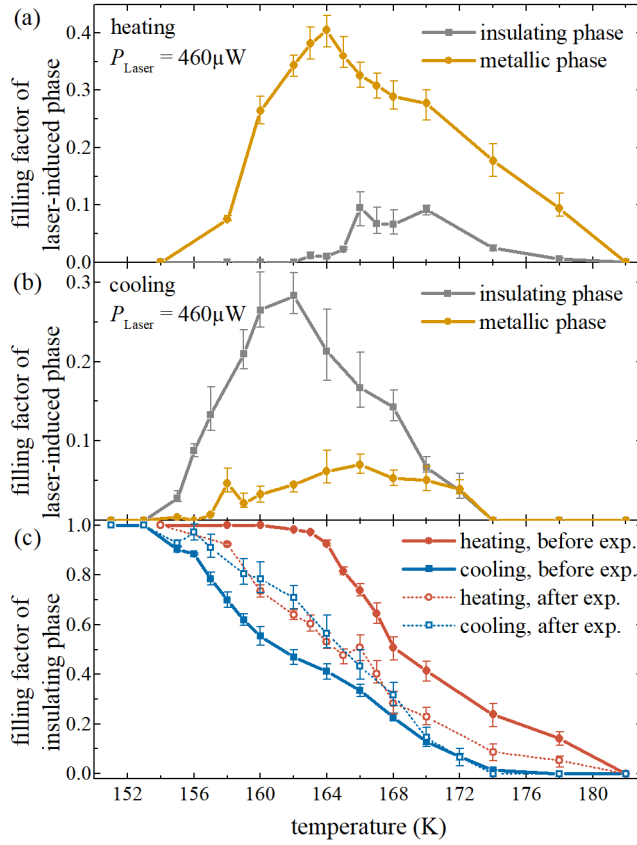
Figure 2.7: Temperature dependence of metal and insulator filling factors affected by laser irradiation of $460\,\mu$W. (a) Filling factors of the metallic and insulating phases induced by laser irradiation during heating. (b) Same filling factors during cooling. (c) Filling factors of the insulating phase during one thermal cycle. Figure from appended **publication 3**.

a structural transition from corundum to a monoclinic crystal structure. Very likely, the V_2O_3 thin film is in a metastable state and the perturbation by the laser scanning drives the system into a stable state.

In a phenomenological numerical model, we were able to reproduce the main features of the experimental results. By increasing the laser intensity in the model, the hysteresis of the filling factors is diminished, in agreement with Fig. 2.7(c).

Concluding this publication, we find that a V_2O_3 thin film is very sensitive to a local perturbation by a focused laser beam. Dependent on the thermal history, laser scanning induces predominantly metallic or insulating domains, respectively. This implies, that laser scanning irradiation erases thermal history and could be used to set or reset memristive devices locally.

Contributions

This study was done in collaboration with the groups of M. J. Rozenberg at the Université Paris-Saclay, Y. Kalcheim at the Technion Haifa, and I. K. Schuller at UC San Diego. The samples were provided by Y. Kalcheim. L. Fratino developed the numerical model. A. Kronman conducted an additional measurement (thermal minor-loops in the supplemental material). The measurements for the main manuscript were conducted at the Eberhard Karls Universität Tübingen. S. Guénon supervised the imaging measurements. F. Tahouni-Bonab conducted parts of the imaging measurements. I improved the measurement setup for better laser stability and developed an adapted measurement software in LabVIEW. I conducted the main part of the laser scanning and widefield imaging measurements and provided the evaluation of the measurement data. In cooperative work with S. Guénon, I created the figures and wrote the manuscript.

Chapter 3

Outlook

As explained in Sec. 1.1, there is a veritable need for applicable material systems and devices, which offer functionalities for bio-mimesis in the emerging field of neuromorphic computing. Within this thesis, thin film devices based on strongly correlated insulators were investigated in order to contribute to this research field. We find signs of an electrothermal origin of the volatile resistive switching in V_2O_3 thin film devices and we are able to correlate local heterogeneities like strain directly to the formation of the conductive filament. Furthermore, we find key parameters, that determine the size of the conductive filaments in planar two-terminal thin film devices based on nickelates. We contribute to the general understanding of the Mott transition by exploring thermodynamical aspects of the first-order transition by local laser-induced perturbations. The presented results advance the research field, in concrete terms, they lead to a better understanding of the resistive switching via formation of conductive filaments and manifest the relevance of metastability during the Mott transition. Proceeding from this, subsequent research questions can be derived.

Besides volatile resistive switching, which is required in order to emulate the behavior of neurons, one needs non-volatile resistive switching for synaptic functionalities like plasticity (see Sec.1.1). At the Eberhard Karls Universität Tübingen, we have preliminary results on $NdNiO_3$ thin film devices, that offer non-volatility. Due to the wide hysteresis and the sharpness of the resistive switching in our high-quality thin films, it is possible to achieve distinguishable resistivity states in a distinct temperature interval. Planar two-terminal thin film devices are prepared in particular resistivity states by performing minor current ramps. Complementary, we can observe the filamentary dynamics simultaneously via widefield microscopy [148].

Combining this phenomenon with our findings of **publication 3**, subsequent questions would be: Can we apply laser-induced quenching of the metastable phase in $NdNiO_3$ thin films as well? And, if yes, can we reset a non-volatile resistive state locally via laser irradiation?

After having explored the spatial dynamics of the filament formation in $NdNiO_3$ and $SmNiO_3$ in **publication 1**, the goal of application-oriented research is to gain more control over the filament. In **publication 2**, we identified local inhomogeneities of the thin film like strain to affect the filament formation and to restrict the path of the filament due to preferred directions. This restriction could be overcome by guiding the filament via focused ion beam (FIB) patterning, most likely due to FIB-induced defects in the thin films. There is a lot of expertise for FIB techniques in the group of Dieter

Koelle and Reinhold Kleiner at the Eberhard Karls Universität Tübingen for the fabrication of Josephson junctions [149–151], which can fruitfully be used for manipulating strongly correlated insulator thin films as well. Trastoy *et al.* demonstrated Helium-ion-irradiation of V_2O_3 [50] and Ghazikhanian *et al.* recently used Gallium-FIB-irradiation in order to manipulate the filament formation in VO_2 and V_2O_3 thin film devices [152]. FIB-irradiation patterning of nickelates and vanadates with Helium- or Neon-FIB is a promising research area to be explored in the future. There were already preliminary works done within this PhD project.

An additional loose end of this work is the comparison of details of the resistive switching dynamics in $NdNiO_3$ and $SmNiO_3$. Complementary to the optical widefield imaging study in **publication 1**, the filament dynamics can be observed via mapping the laser-beam-induced voltage change in an additional mode of the laser scanning microscope [95]. In preliminary studies, we observe different fingerprints of conductive filaments in $NdNiO_3$ and $SmNiO_3$. In $NdNiO_3$, we can associate the conducting filament with a strong homogeneous voltage signal, whereas we observe typical hot spot signals at the edges of filaments in $SmNiO_3$ devices, similar to hot spots in mesas of the strongly correlated oxide $Bi_2Sr_2CaCu_2O_8$ [153]. Systematic and extensive voltage imaging measurement series in combination with theoretical modeling can very likely give more detailed insights into the differences of the filamentary resistive switching in these materials.

Bibliography

[1] I. K. Schuller, R. Stevens, R. Pino, and M. Pechan, *Neuromorphic Computing – From Materials Research to Systems Architecture Roundtable*, 10.2172/1283147, 2015.

[2] J. del Valle, J. G. Ramírez, M. J. Rozenberg, and I. K. Schuller, "Challenges in materials and devices for resistive-switching-based neuromorphic computing", Journal of Applied Physics **124**, 211101 (2018).

[3] A. Hoffmann, S. Ramanathan, J. Grollier, A. D. Kent, M. J. Rozenberg, I. K. Schuller, O. G. Shpyrko, R. C. Dynes, Y. Fainman, A. Frano, E. E. Fullerton, G. Galli, V. Lomakin, S. P. Ong, A. K. Petford-Long, J. A. Schuller, M. D. Stiles, Y. Takamura, and Y. Zhu, "Quantum materials for energy-efficient neuromorphic computing: Opportunities and challenges", APL Materials **10**, 070904 (2022).

[4] T. J. Park, S. Deng, S. Manna, A. N. M. N. Islam, H. Yu, Y. Yuan, D. D. Fong, A. A. Chubykin, A. Sengupta, S. K. R. S. Sankaranarayanan, and S. Ramanathan, "Complex Oxides for Brain-Inspired Computing: A Review", Advanced Materials **35**, 2203352 (2022).

[5] A. Jain, J. Mao, and K. Mohiuddin, "Artificial neural networks: a tutorial", Computer **29**, 31–44 (1996).

[6] Y. LeCun, Y. Bengio, and G. Hinton, "Deep learning", Nature **521**, 436–444 (2015).

[7] H. Markram, W. Gerstner, and P. J. Sjöström, "Spike-Timing-Dependent Plasticity: A Comprehensive Overview", Frontiers in Synaptic Neuroscience **4**, 2 (2012).

[8] F. Tesler, C. Adda, J. Tranchant, B. Corraze, E. Janod, L. Cario, P. Stoliar, and M. Rozenberg, "Relaxation of a Spiking Mott Artificial Neuron", Physical Review Applied **10**, 054001 (2018).

[9] J. del Valle, P. Salev, Y. Kalcheim, and I. K. Schuller, "A caloritronics-based Mott neuristor", Scientific Reports **10**, 4292 (2020).

[10] J. Shi, S. D. Ha, Y. Zhou, F. Schoofs, and S. Ramanathan, "A correlated nickelate synaptic transistor", Nature Communications **4**, 2676 (2013).

[11] Y. Zhou and S. Ramanathan, "Mott Memory and Neuromorphic Devices", Proceedings of the IEEE **103**, 1289–1310 (2015).

[12] B. Keimer and J. E. Moore, "The physics of quantum materials", Nature Physics **13**, 1045–1055 (2017).

[13] D. N. Basov, R. D. Averitt, and D. Hsieh, "Towards properties on demand in quantum materials", Nature Materials **16**, 1077–1088 (2017).

[14] S. Raoux, "Phase Change Materials", Annual Review of Materials Research **39**, 25–48 (2009).

[15] L. Wang, S.-R. Lu, and J. Wen, "Recent Advances on Neuromorphic Systems Using Phase-Change Materials", Nanoscale Research Letters **12**, 347 (2017).

[16] A. K. Geim and I. V. Grigorieva, "Van der Waals heterostructures", Nature **499**, 419–425 (2013).

[17] Z. Zhang, D. Yang, H. Li, C. Li, Z. Wang, L. Sun, and H. Yang, "2D materials and van der Waals heterojunctions for neuromorphic computing", Neuromorphic Computing and Engineering **2**, 032004 (2022).

[18] M. Imada, A. Fujimori, and Y. Tokura, "Metal-insulator transitions", Reviews of Modern Physics **70**, 1039–1263 (1998).

[19] M. D. Pickett, G. Medeiros-Ribeiro, and R. S. Williams, "A scalable neuristor built with Mott memristors", Nature Materials **12**, 114–117 (2012).

[20] M. Ignatov, M. Ziegler, M. Hansen, A. Petraru, and H. Kohlstedt, "A memristive spiking neuron with firing rate coding", Frontiers in Neuroscience **9**, 376 (2015).

[21] P. Stoliar, J. Tranchant, B. Corraze, E. Janod, M.-P. Besland, F. Tesler, M. Rozenberg, and L. Cario, "A Leaky-Integrate-and-Fire Neuron Analog Realized with a Mott Insulator", Advanced Functional Materials **27**, 1604740 (2017).

[22] Z. Xu, A. A. Bernussi, and Z. Fan, "Voltage Pulse Driven VO_2 Volatile Resistive Transition Devices as Leaky Integrate-and-Fire Artificial Neurons", Electronics **11**, 516 (2022).

[23] S. M. Bohaichuk, S. Kumar, G. Pitner, C. J. McClellan, J. Jeong, M. G. Samant, H.-. P. Wong, S. S. P. Parkin, R. S. Williams, and E. Pop, "Fast Spiking of a Mott VO_2-Carbon Nanotube Composite Device", Nano Letters **19**, 6751–6755 (2019).

[24] S. Oh, Y. Shi, J. del Valle, P. Salev, Y. Lu, Z. Huang, Y. Kalcheim, I. K. Schuller, and D. Kuzum, "Energy-efficient Mott activation neuron for full-hardware implementation of neural networks", Nature Nanotechnology **16**, 680–687 (2021).

[25] J. del Valle, P. Salev, F. Tesler, N. M. Vargas, Y. Kalcheim, P. Wang, J. Trastoy, M.-H. Lee, G. Kassabian, J. G. Ramírez, M. J. Rozenberg, and I. K. Schuller, "Subthreshold firing in Mott nanodevices", Nature **569**, 388–392 (2019).

[26] S. Kumar, J. P. Strachan, and R. S. Williams, "Chaotic dynamics in nanoscale NbO_2 Mott memristors for analogue computing", Nature **548**, 318–321 (2017).

[27] W. Yi, K. K. Tsang, S. K. Lam, X. Bai, J. A. Crowell, and E. A. Flores, "Biological plausibility and stochasticity in scalable VO_2 active memristor neurons", Nature Communications **9**, 4661 (2018).

[28] M. Jerry, K. Ni, A. Parihar, A. Raychowdhury, and S. Datta, "Stochastic Insulator-to-Metal Phase Transition-Based True Random Number Generator", IEEE Electron Device Letters **39**, 139–142 (2018).

[29] J. d. del Valle, P. Salev, S. Gariglio, Y. Kalcheim, I. K. Schuller, and J.-M. Triscone, "Generation of Tunable Stochastic Sequences Using the Insulator-Metal Transition", Nano Letters **22**, 1251–1256 (2022).

[30] D. Khomskii, *Transition metal compounds* (Cambridge University Press, 2014).

[31] F. J. Morin, "Oxides Which Show a Metal-to-Insulator Transition at the Neel Temperature", Physical Review Letters **3**, 34–36 (1959).

[32] D. B. McWhan, A. Menth, J. P. Remeika, W. F. Brinkman, and T. M. Rice, "Metal-Insulator Transitions in Pure and Doped V_2O_3", Physical Review B **7**, 1920–1931 (1973).

[33] D. B. McWhan and J. P. Remeika, "Metal-Insulator Transition in $(V_{1-x}Cr_x)_2O_3$", Physical Review B **2**, 3734–3750 (1970).

[34] A. Georges, G. Kotliar, W. Krauth, and M. J. Rozenberg, "Dynamical mean-field theory of strongly correlated fermion systems and the limit of infinite dimensions", Reviews of Modern Physics **68**, 13–125 (1996).

[35] P. Limelette, A. Georges, D. Jerome, P. Wzietek, P. Metcalf, and J. M. Honig, "Universality and Critical Behavior at the Mott Transition", Science **302**, 89–92 (2003).

[36] J. Torrance, P. Lacorre, A. Nazzal, E. Ansaldo, and C. Niedermayer, "Systematic study of insulator-metal transitions in perovskites RNiO$_3$ (R=Pr,Nd,Sm,Eu) due to closing of charge-transfer gap", Physical Review B **45**, 8209–8212 (1992).

[37] S. Catalano, M. Gibert, J. Fowlie, J. Íñiguez, J.-M. Triscone, and J. Kreisel, "Rare-earth nickelates RNiO$_3$: thin films and heterostructures", Reports on Progress in Physics **81**, 046501 (2018).

[38] F. Bloch, "Über die Quantenmechanik der Elektronen in Kristallgittern", Zeitschrift für Physik **52**, 555–600 (1929).

[39] J. Hubbard and B. Flowers, "Electron correlations in narrow energy bands", Proceedings of the Royal Society of London. Series A. Mathematical and Physical Sciences **276**, 238–257 (1963).

[40] N. F. Mott, "Metal-Insulator Transition", Reviews of Modern Physics **40**, 677–683 (1968).

[41] N. F. Mott, *Metal-Insulator Transitions*, 2nd ed. (CRC Press, 1990).

[42] P. Hansmann, A. Toschi, G. Sangiovanni, T. Saha-Dasgupta, S. Lupi, M. Marsi, and K. Held, "Mott-Hubbard transition in V_2O_3 revisited", Physica Status Solidi B **250**, 1251–1264 (2013).

[43] P. D. Dernier and M. Marezio, "Crystal Structure of the Low-Temperature Antiferromagnetic Phase of V_2O_3", Physical Review B **2**, 3771–3776 (1970).

[44] P. Hansmann, M. W. Haverkort, A. Toschi, G. Sangiovanni, F. Rodolakis, J. P. Rueff, M. Marsi, and K. Held, "Atomic and itinerant effects at the transition-metal x-ray absorption K pre-edge exemplified in the case of V_2O_3", Physical Review B **85**, 115136 (2012).

[45] A. I. Poteryaev, J. M. Tomczak, S. Biermann, A. Georges, A. I. Lichtenstein, A. N. Rubtsov, T. Saha-Dasgupta, and O. K. Andersen, "Enhanced crystal-field splitting and orbital-selective coherence induced by strong correlations in V_2O_3", Physical Review B **76**, 085127 (2007).

[46] M. M. Qazilbash, A. A. Schafgans, K. S. Burch, S. J. Yun, B. G. Chae, B. J. Kim, H. T. Kim, and D. N. Basov, "Electrodynamics of the vanadium oxides VO_2 and V_2O_3", Physical Review B **77**, 115121 (2008).

[47] M. K. Stewart, D. Brownstead, S. Wang, K. G. West, J. G. Ramirez, M. M. Qazilbash, N. B. Perkins, I. K. Schuller, and D. N. Basov, "Insulator-to-metal transition and correlated metallic state of V_2O_3 investigated by optical spectroscopy", Physical Review B **85**, 205113 (2012).

[48] Y. Kalcheim, N. Butakov, N. M. Vargas, M.-H. Lee, J. del Valle, J. Trastoy, P. Salev, J. Schuller, and I. K. Schuller, "Robust Coupling between Structural and Electronic Transitions in a Mott Material", Physical Review Letters **122**, 057601 (2019).

[49] B. A. Frandsen, Y. Kalcheim, I. Valmianski, A. S. McLeod, Z. Guguchia, S. C. Cheung, A. M. Hallas, M. N. Wilson, Y. Cai, G. M. Luke, Z. Salman, A. Suter, T. Prokscha, T. Murakami, H. Kageyama, D. N. Basov, I. K. Schuller, and Y. J. Uemura, "Intertwined magnetic, structural, and electronic transitions in V_2O_3", Physical Review B **100**, 235136 (2019).

[50] J. Trastoy, A. Camjayi, J. del Valle, Y. Kalcheim, J.-P. Crocombette, D. A. Gilbert, J. A. Borchers, J. E. Villegas, D. Ravelosona, M. J. Rozenberg, and I. K. Schuller, "Magnetic field frustration of the metal-insulator transition in V_2O_3", Physical Review B **101**, 245109 (2020).

[51] E. Barazani, D. Das, C. Huang, A. Rakshit, C. Saguy, P. Salev, J. del Valle, M. C. Toroker, I. K. Schuller, and Y. Kalcheim, "Positive and Negative Pressure Regimes in Anisotropically Strained V_2O_3 Films", Advanced Functional Materials **33**, 2211801 (2023).

[52] H. Schuler, S. Klimm, G. Weissmann, C. Renner, and S. Horn, "Influence of strain on the electronic properties of epitaxial V_2O_3 thin films", Thin Solid Films **299**, 119–124 (1997).

[53] S. Yonezawa, Y. Muraoka, Y. Ueda, and Z. Hiroi, "Epitaxial strain effects on the metal-insulator transition in V_2O_3 thin films", Solid State Communications **129**, 245–248 (2004).

[54] S. Autier-Laurent, B. Mercey, D. Chippaux, P. Limelette, and C. Simon, "Strain-induced pressure effect in pulsed laser deposited thin films of the strongly correlated oxide V_2O_3", Physical Review B **74**, 195109 (2006).

[55] J. Sakai, P. Limelette, and H. Funakubo, "Transport properties and c/a ratio of V_2O_3 thin films grown on C- and R-plane sapphire substrates by pulsed laser deposition", Applied Physics Letters **107**, 107 (2015).

[56] J. Trastoy, Y. Kalcheim, J. del Valle, I. Valmianski, and I. K. Schuller, "Enhanced metal-insulator transition in V_2O_3 by thermal quenching after growth", Journal of Materials Science **53**, 9131–9137 (2018).

[57] A. S. McLeod, E. van Heumen, J. G. Ramirez, S. Wang, T. Saerbeck, S. Guenon, M. Goldflam, L. Anderegg, P. Kelly, A. Mueller, M. K. Liu, I. K. Schuller, and D. N. Basov, "Nanotextured phase coexistence in the correlated insulator V_2O_3", Nature Physics **13**, 80–86 (2016).

[58] S.-K. Mo, J. D. Denlinger, H.-D. Kim, J.-H. Park, J. W. Allen, A. Sekiyama, A. Yamasaki, K. Kadono, S. Suga, Y. Saitoh, T. Muro, P. Metcalf, G. Keller, K. Held, V. Eyert, V. I. Anisimov, and D. Vollhardt, "Prominent Quasiparticle Peak in the Photoemission Spectrum of the Metallic Phase of V_2O_3", Physical Review Letters **90**, 186403 (2003).

[59] A. E. Bocquet, T. Mizokawa, T. Saitoh, H. Namatame, and A. Fujimori, "Electronic structure of $3d$-transition-metal compounds by analysis of the $2p$ core-level photoemission spectra", Physical Review B **46**, 3771–3784 (1992).

[60] T. Mizokawa, A. Fujimori, H. Namatame, K. Akeyama, and N. Kosugi, "Electronic structure of the local-singlet insulator $NaCuO_2$", Physical Review B **49**, 7193–7204 (1994).

[61] J. Zaanen, G. A. Sawatzky, and J. W. Allen, "Band gaps and electronic structure of transition-metal compounds", Physical Review Letters **55**, 418–421 (1985).

[62] V. M. Goldschmidt, "Die Gesetze der Krystallochemie", Die Naturwissenschaften **14**, 477–485 (1926).

[63] R. J. Green, M. W. Haverkort, and G. A. Sawatzky, "Bond disproportionation and dynamical charge fluctuations in the perovskite rare-earth nickelates", Physical Review B **94**, 195127 (2016).

[64] H. Park, A. J. Millis, and C. A. Marianetti, "Site-Selective Mott Transition in Rare-Earth-Element Nickelates", Physical Review Letters **109**, 156402 (2012).

[65] S. Johnston, A. Mukherjee, I. Elfimov, M. Berciu, and G. A. Sawatzky, "Charge Disproportionation without Charge Transfer in the Rare-Earth-Element Nickelates as a Possible Mechanism for the Metal-Insulator Transition", Physical Review Letters **112**, 106404 (2014).

[66] A. Subedi, O. E. Peil, and A. Georges, "Low-energy description of the metal-insulator transition in the rare-earth nickelates", Physical Review B **91**, 075128 (2015).

[67] J. Varignon, M. N. Grisolia, J. Íñiguez, A. Barthélémy, and M. Bibes, "Complete phase diagram of rare-earth nickelates from first-principles", npj Quantum Materials **2**, 21 (2017).

[68] S. Prosandeev, L. Bellaiche, and J. Íñiguez, "*Ab initio* study of the factors affecting the ground state of rare-earth nickelates", Physical Review B **85**, 214431 (2012).

[69] S. Yamamoto and T. Fujiwara, "Symmetry consideration and e_g bands in NdNiO$_3$ and YNiO$_3$", Journal of Physics and Chemistry of Solids **63**, 1347–1351 (2002).

[70] A. Hampel and C. Ederer, "Interplay between breathing mode distortion and magnetic order in rare-earth nickelates RNiO$_3$ within DFT+U", Physical Review B **96**, 165130 (2017).

[71] O. E. Peil, A. Hampel, C. Ederer, and A. Georges, "Mechanism and control parameters of the coupled structural and metal-insulator transition in nickelates", Physical Review B **99**, 245127 (2019).

[72] M. L. Medarde, "Structural, magnetic and electronic properties of RNiO$_3$ perovskites (R = rare earth)", Journal of Physics: Condensed Matter **9**, 1679–1707 (1997).

[73] J. Pérez-Cacho, J. Blasco, J. García, M. Castro, and J. Stankiewicz, "Study of the phase transitions in SmNiO$_3$", Journal of Physics: Condensed Matter **11**, 405–415 (1999).

[74] S. Catalano, M. Gibert, V. Bisogni, O. E. Peil, F. He, R. Sutarto, M. Viret, P. Zubko, R. Scherwitzl, A. Georges, G. A. Sawatzky, T. Schmitt, and J.-M. Triscone, "Electronic transitions in strained SmNiO$_3$ thin films", APL Materials **2**, 116110 (2014).

[75] J. Liu, M. Kargarian, M. Kareev, B. Gray, P. J. Ryan, A. Cruz, N. Tahir, Y.-D. Chuang, J. Guo, J. M. Rondinelli, J. W. Freeland, G. A. Fiete, and J. Chakhalian, "Heterointerface engineered electronic and magnetic phases of NdNiO$_3$ thin films", Nature Communications **4**, 2714 (2013).

[76] L. Landau, "The Theory of Phase Transitions", Nature **138**, 840–841 (1936).

[77] L. Landau and E. Lifshitz, *Statistical physics*, Vol. 5 (Elsevier Science, 2013).

[78] C. B. Muratov, "Theory of domain patterns in systems with long-range interactions of Coulomb type", Physical Review E **66**, 066108 (2002).

[79] A. Macridin, M. Jarrell, and T. Maier, "Phase separation in the Hubbard model using the dynamical cluster approximation", Physical Review B **74**, 085104 (2006).

[80] C.-H. Yee and L. Balents, "Phase Separation in Doped Mott Insulators", Physical Review X **5**, 021007 (2015).

[81] A. M. Alsaqqa, S. Singh, S. Middey, M. Kareev, J. Chakhalian, and G. Sambandamurthy, "Phase coexistence and dynamical behavior in $NdNiO_3$ ultrathin films", Physical Review B **95**, 125132 (2017).

[82] R. S. Bisht, S. Samanta, and A. K. Raychaudhuri, "Phase coexistence near the metal-insulator transition in a compressively strained $NdNiO_3$ film grown on $LaAlO_3$: scanning tunneling, noise, and impedance spectroscopy studies", Physical Review B **95**, 115147 (2017).

[83] M. Seul and D. Andelman, "Domain Shapes and Patterns: The Phenomenology of Modulated Phases", Science **267**, 476–483 (1995).

[84] A. M. Bratkovsky, S. C. Marais, V. Heine, and E. K. H. Salje, "The theory of fluctuations and texture embryos in structural phase transitions mediated by strain", Journal of Physics: Condensed Matter **6**, 3679–3696 (1994).

[85] Y. Gao, W. Lu, and Z. Suo, "A mesophase transition in a binary monolayer on a solid surface", Acta Materialia **50**, 2297–2308 (2002).

[86] C. Castellani, C. D. Castro, D. Feinberg, and J. Ranninger, "New Model Hamiltonian for the Metal-Insulator Transition", Physical Review Letters **43**, 1957–1960 (1979).

[87] G. Kotliar, E. Lange, and M. J. Rozenberg, "Landau Theory of the Finite Temperature Mott Transition", Physical Review Letters **84**, 5180–5183 (2000).

[88] M. I. Díaz, J. E. Han, and C. Aron, "Electrically driven insulator-to-metal transition in a correlated insulator: Electronic mechanism and thermal description", Physical Review B **107**, 195148 (2023).

[89] G. Kotliar and A. E. Ruckenstein, "New Functional Integral Approach to Strongly Correlated Fermi Systems: The Gutzwiller Approximation as a Saddle Point", Physical Review Letters **57**, 1362–1365 (1986).

[90] K. W. Post, A. S. McLeod, M. Hepting, M. Bluschke, Y. Wang, G. Cristiani, G. Logvenov, A. Charnukha, G. X. Ni, P. Radhakrishnan, M. Minola, A. Pasupathy, A. V. Boris, E. Benckiser, K. A. Dahmen, E. W. Carlson, B. Keimer, and D. N. Basov, "Coexisting first- and second-order electronic phase transitions in a correlated oxide", Nature Physics **14**, 1056–1061 (2018).

[91] T. Bar, S. K. Choudhary, M. A. Ashraf, K. S. Sujith, S. Puri, S. Raj, and B. Bansal, "Kinetic Spinodal Instabilities in the Mott Transition in V_2O_3: Evidence from Hysteresis Scaling and Dissipative Phase Ordering", Physical Review Letters **121**, 045701 (2018).

[92] S. Kundu, T. Bar, R. K. Nayak, and B. Bansal, "Critical Slowing Down at the Abrupt Mott Transition: When the First-Order Phase Transition Becomes Zeroth Order and Looks Like Second Order", Physical Review Letters **124**, 095703 (2020).

[93] H. Garcke and U. Weikard, "Numerical approximation of the Cahn-Larché equation", Numerische Mathematik **100**, 639–662 (2005).

[94] J. Kim, C. Ko, A. Frenzel, S. Ramanathan, and J. E. Hoffman, "Nanoscale imaging and control of resistance switching in VO_2 at room temperature", Applied Physics Letters **96**, 213106 (2010).

[95] S. Guénon, S. Scharinger, S. Wang, J. G. Ramírez, D. Koelle, R. Kleiner, and I. K. Schuller, "Electrical breakdown in a V_2O_3 device at the insulator-to-metal transition", EPL (Europhysics Letters) **101**, 57003 (2013).

[96] A. Zimmers, L. Aigouy, M. Mortier, A. Sharoni, S. Wang, K. G. West, J. G. Ramirez, and I. K. Schuller, "Role of Thermal Heating on the Voltage Induced Insulator-Metal Transition in VO_2", Physical Review Letters **110**, 056601 (2013).

[97] S. Kumar, M. D. Pickett, J. P. Strachan, G. Gibson, Y. Nishi, and R. S. Williams, "Local Temperature Redistribution and Structural Transition During Joule-Heating-Driven Conductance Switching in VO_2", Advanced Materials **25**, 6128–6132 (2013).

[98] J. S. Brockman, L. Gao, B. Hughes, C. T. Rettner, M. G. Samant, K. P. Roche, and S. S. P. Parkin, "Subnanosecond incubation times for electric-field-induced metallization of a correlated electron oxide", Nature Nanotechnology **9**, 453–458 (2014).

[99] E. Janod, J. Tranchant, B. Corraze, M. Querré, P. Stoliar, M. Rozenberg, T. Cren, D. Roditchev, V. T. Phuoc, M.-P. Besland, and L. Cario, "Resistive Switching in Mott Insulators and Correlated Systems", Advanced Functional Materials **25**, 6287–6305 (2015).

[100] S. Shen, M. Williamson, G. Cao, J. Zhou, J. Goodenough, and M. Tsoi, "Non-destructive reversible resistive switching in Cr doped Mott insulator Ca_2RuO_4: Interface vs bulk effects", Journal of Applied Physics **122**, 245108 (2017).

[101] J. del Valle, Y. Kalcheim, J. Trastoy, A. Charnukha, D. N. Basov, and I. K. Schuller, "Electrically Induced Multiple Metal-Insulator Transitions in Oxide Nanodevices", Physical Review Applied **8**, 054041 (2017).

[102] G. Gopalakrishnan, D. Ruzmetov, and S. Ramanathan, "On the triggering mechanism for the metal-insulator transition in thin film VO_2 devices: electric field versus thermal effects", Journal of Materials Science **44**, 5345–5353 (2009).

[103] I. Valmianski, P. Y. Wang, S. Wang, J. G. Ramirez, S. Guénon, and I. K. Schuller, "Origin of the current-driven breakdown in vanadium oxides: Thermal versus electronic", Physical Review B **98**, 195144 (2018).

[104] T. Oka, R. Arita, and H. Aoki, "Breakdown of a Mott Insulator: A Nonadiabatic Tunneling Mechanism", Physical Review Letters **91**, 066406 (2003).

[105] H. Yamakawa, T. Miyamoto, T. Morimoto, T. Terashige, H. Yada, N. Kida, M. Suda, H. M. Yamamoto, R. Kato, K. Miyagawa, K. Kanoda, and H. Okamoto, "Mott transition by an impulsive dielectric breakdown", Nature Materials **16**, 1100–1105 (2017).

[106] T. Oka and H. Aoki, "Ground-State Decay Rate for the Zener Breakdown in Band and Mott Insulators", Physical Review Letters **95**, 137601 (2005).

[107] M. Eckstein, T. Oka, and P. Werner, "Dielectric Breakdown of Mott Insulators in Dynamical Mean-Field Theory", Physical Review Letters **105**, 146404 (2010).

[108] F. Heidrich-Meisner, I. González, K. A. Al-Hassanieh, A. E. Feiguin, M. J. Rozenberg, and E. Dagotto, "Nonequilibrium electronic transport in a one-dimensional Mott insulator", Physical Review B **82**, 205110 (2010).

[109] R. Kumai, Y. Okimoto, and Y. Tokura, "Current-Induced Insulator-Metal Transition and Pattern Formation in an Organic Charge-Transfer Complex", Science **284**, 1645–1647 (1999).

[110] W.-R. Lee and K. Park, "Dielectric breakdown via emergent nonequilibrium steady states of the electric-field-driven Mott insulator", Physical Review B **89**, 205126 (2014).

[111] N. Sugimoto, S. Onoda, and N. Nagaosa, "Field-induced metal-insulator transition and switching phenomenon in correlated insulators", Physical Review B **78**, 155104 (2008).

[112] G. Mazza, A. Amaricci, M. Capone, and M. Fabrizio, "Field-Driven Mott Gap Collapse and Resistive Switch in Correlated Insulators", Physical Review Letters **117**, 176401 (2016).

[113] J. Li, C. Aron, G. Kotliar, and J. E. Han, "Electric-Field-Driven Resistive Switching in the Dissipative Hubbard Model", Physical Review Letters **114**, 226403 (2015).

[114] E. Spenke, "Eine anschauliche Deutung der Abzweigtemperatur scheibenförmiger Heißleiter", Archiv für Elektrotechnik **30**, 728–736 (1936).

[115] E. Spenke, "Zur technischen Beherrschung des Wärmedurchschlages von Heißleitern", in *Wissenschaftliche Veröffentlichungen aus den Siemens-Werken* (Springer Berlin Heidelberg, 1936), pp. 92–121.

[116] H. Lueder, W. Schottky, and E. Spenke, "Zur technischen Beherrschung des Wärmedurchschlags", Die Naturwissenschaften **24**, 61–61 (1936).

[117] A. V. Gurevich and R. G. Mints, "Self-heating in normal metals and superconductors", Reviews of Modern Physics **59**, 941–999 (1987).

[118] V. I. Polozov, S. S. Maklakov, A. L. Rakhmanov, S. A. Maklakov, and V. N. Kisel, "Blow-up overheating instability in vanadium dioxide thin films", Physical Review B **101**, 214310 (2020).

[119] Y. Kalcheim, A. Camjayi, J. del Valle, P. Salev, M. Rozenberg, and I. K. Schuller, "Non-thermal resistive switching in Mott insulator nanowires", Nature Communications **11**, 2985 (2020).

[120] B.-J. Kim, G. Seo, and Y. W. Lee, "Bidirectional laser triggering of planar device based on vanadium dioxide thin film", Optics Express **22**, 9016 (2014).

[121] J. Kim, S. J. Jeong, B.-J. Kim, and Y. W. Lee, "Laser-triggered current gating based on photothermal effect in VO_2 thin-film device using CO_2 laser", Applied Physics B **124**, 67 (2018).

[122] G. Seo, B.-J. Kim, Y. Wook Lee, and H.-T. Kim, "Photo-Assisted Bistable Switching Using Mott Transition in Two-Terminal VO_2 Device", Applied Physics Letters **100**, 011908 (2012).

[123] G. Li, D. Xie, H. Zhong, Z. Zhang, X. Fu, Q. Zhou, Q. Li, H. Ni, J. Wang, E.-j. Guo, M. He, C. Wang, G. Yang, K. Jin, and C. Ge, "Photo-Induced Non-Volatile VO_2 Phase Transition for Neuromorphic Ultraviolet Sensors", Nature Communications **13**, 1729 (2022).

[124] Y.-W. Lee, E.-S. Kim, B.-S. Shin, and S.-M. Lee, "High-Performance Optical Gating in Junction Device based on Vanadium Dioxide Thin Film Grown by Sol-Gel Method", Journal of Electrical Engineering and Technology **7**, 784–788 (2012).

[125] G. Seo, B.-J. Kim, H.-T. Kim, and Y. W. Lee, "Photo-Assisted Electrical Oscillation in Two-Terminal Device Based on Vanadium Dioxide Thin Film", Journal of Lightwave Technology **30**, 2718–2724 (2012).

[126] A. Ronchi, P. Homm, M. Menghini, P. Franceschini, F. Maccherozzi, F. Banfi, G. Ferrini, F. Cilento, F. Parmigiani, S. S. Dhesi, M. Fabrizio, J.-P. Locquet, and

C. Giannetti, "Early-stage dynamics of metallic droplets embedded in the nanotextured Mott insulating phase of V_2O_3", Physical Review B **100**, 075111 (2019).

[127] A. Ronchi, P. Franceschini, P. Homm, M. Gandolfi, G. Ferrini, S. Pagliara, F. Banfi, M. Menghini, J.-. Locquet, and C. Giannetti, "Light-assisted Resistance Collapse in a V_2O_3-Based Mott-Insulator Device", Physical Review Applied **15**, 044023 (2021).

[128] A. Ronchi, P. Franceschini, A. De Poli, P. Homm, A. Fitzpatrick, F. Maccherozzi, G. Ferrini, F. Banfi, S. S. Dhesi, M. Menghini, M. Fabrizio, J.-P. Locquet, and C. Giannetti, "Nanoscale self-organization and metastable non-thermal metallicity in Mott insulators", Nature Communications **13**, 3730 (2022).

[129] F. Giorgianni, J. Sakai, and S. Lupi, "Overcoming the thermal regime for the electric-field driven Mott transition in vanadium sesquioxide", Nature Communications **10**, 1159 (2019).

[130] A. Cavalleri, C. Tóth, C. W. Siders, J. A. Squier, F. Ráksi, P. Forget, and J. C. Kieffer, "Femtosecond Structural Dynamics in VO_2 during an Ultrafast Solid-Solid Phase Transition", Physical Review Letters **87**, 237401 (2001).

[131] S. Wall, S. Yang, L. Vidas, M. Chollet, J. M. Glownia, M. Kozina, T. Katayama, T. Henighan, M. Jiang, T. A. Miller, D. A. Reis, L. A. Boatner, O. Delaire, and M. Trigo, "Ultrafast disordering of vanadium dimers in photoexcited VO_2", Science **362**, 572–576 (2018).

[132] M. R. Otto, L. P. René de Cotret, D. A. Valverde-Chavez, K. L. Tiwari, N. Émond, M. Chaker, D. G. Cooke, and B. J. Siwick, "How optical excitation controls the structure and properties of vanadium dioxide", Proceedings of the National Academy of Sciences **116**, 450–455 (2018).

[133] J. del Valle, N. M. Vargas, R. Rocco, P. Salev, Y. Kalcheim, P. N. Lapa, C. Adda, M.-H. Lee, P. Y. Wang, L. Fratino, M. J. Rozenberg, and I. K. Schuller, "Spatiotemporal characterization of the field-induced insulator-to-metal transition", Science **373**, 907–911 (2021).

[134] Y. Zhou, X. Chen, C. Ko, Z. Yang, C. Mouli, and S. Ramanathan, "Voltage-Triggered Ultrafast Phase Transition in Vanadium Dioxide Switches", IEEE Electron Device Letters **34**, 220–222 (2013).

[135] J. del Valle, R. Rocco, C. Domínguez, J. Fowlie, S. Gariglio, M. J. Rozenberg, and J.-M. Triscone, "Dynamics of the electrically induced insulator-to-metal transition in rare-earth nickelates", Physical Review B **104**, 165141 (2021).

[136] R. Waser, R. Dittmann, G. Staikov, and K. Szot, "Redox-Based Resistive Switching Memories – Nanoionic Mechanisms, Prospects, and Challenges", Advanced Materials **21**, 2632–2663 (2009).

[137] H.-S. P. Wong, H.-Y. Lee, S. Yu, Y.-S. Chen, Y. Wu, P.-S. Chen, B. Lee, F. T. Chen, and M.-J. Tsai, "Metal-Oxide RRAM", Proceedings of the IEEE **100**, 1951–1970 (2012).

[138] D. Ielmini, "Resistive switching memories based on metal oxides: mechanisms, reliability and scaling", Semiconductor Science and Technology **31**, 063002 (2016).

[139] R. Waser and M. Aono, "Nanoionics-based resistive switching memories", Nature Materials **6**, 833–840 (2007).

[140] M. T. Greiner, L. Chai, M. G. Helander, W.-M. Tang, and Z.-H. Lu, "Transition Metal Oxide Work Functions: The Influence of Cation Oxidation State and Oxygen Vacancies", Advanced Functional Materials **22**, 4557–4568 (2012).

Bibliography

[141] P. Salev, J. del Valle, Y. Kalcheim, and I. K. Schuller, "Giant nonvolatile resistive switching in a Mott oxide and ferroelectric hybrid", Proceedings of the National Academy of Sciences **116**, 8798–8802 (2019).

[142] A. Moatti, R. Sachan, and J. Narayan, "Volatile and non-volatile behavior of metal-insulator transition in VO_2 through oxygen vacancies tunability for memory applications", Journal of Applied Physics **128**, 045302 (2020).

[143] T. Driscoll, H.-T. Kim, B.-G. Chae, M. Di Ventra, and D. N. Basov, "Phase-transition driven memristive system", Applied Physics Letters **95**, 043503 (2009).

[144] A. Rana, C. Li, G. Koster, and H. Hilgenkamp, "Resistive switching studies in VO_2 thin films", Scientific Reports **10**, 3293 (2020).

[145] X. Gao, C. M. M. Rosário, and H. Hilgenkamp, "Multi-level operation in VO_2-based resistive switching devices", AIP Advances **12**, 015218 (2022).

[146] M. M. Lange, S. Guénon, F. Lever, R. Kleiner, and D. Koelle, "A High-Resolution Combined Scanning Laser and Widefield Polarizing Microscope for Imaging at Temperatures from 4 K to 300 K", Review of Scientific Instruments **88**, 123705 (2017).

[147] M. M. Lange, "A High-Resolution Polarizing Microscope for Cryogenic Imaging: Development and Application to Investigations on Twin Walls in $SrTiO_3$ and the Metal-Insulator Transition in V_2O_3", PhD thesis (Universität Tübingen, 2018).

[148] F. Tahouni-Bonab et al., "Microscopic study of non-volatile resistive swiching in $NdNiO_3$ thin film devices (working title)", in preparation.

[149] B. Müller, M. Karrer, F. Limberger, M. Becker, B. Schröppel, C. Burkhardt, R. Kleiner, E. Goldobin, and D. Koelle, "Josephson Junctions and SQUIDs Created by Focused Helium-Ion-Beam Irradiation of $YBa_2Cu_3O_7$", Physical Review Applied **11**, 044082 (2019).

[150] K. Uhl, D. Hackenbeck, D. Koelle, R. Kleiner, and D. Bothner, "Extracting the current-phase-relation of a monolithic three-dimensional nano-constriction using a DC-current-tunable superconducting microwave cavity", (2024), arXiv:2402.10276v1 `[cond-mat.mes-hall]`.

[151] T. Griener et al., "Dayem Bridges Fabricated in Superconducting Thin Films via Ga-, Ne-, and He-Focused Ion Beam Irradiation (working title)", in preparation.

[152] N. Ghazikhanian, J. del Valle, P. Salev, R. El Hage, Y. Kalcheim, C. Adda, and I. K. Schuller, "Resistive switching localization by selective focused ion beam irradiation", Applied Physics Letters **123**, 123505 (2023).

[153] H. B. Wang, S. Guénon, J. Yuan, A. Iishi, S. Arisawa, T. Hatano, T. Yamashita, D. Koelle, and R. Kleiner, "Hot Spots and Waves in $Bi_2Sr_2CaCu_2O_8$ Intrinsic Josephson Junction Stacks: A Study by Low Temperature Scanning Laser Microscopy", Physical Review Letters **102**, 017006 (2009).

Appended Publications

Publication 1

Characteristic length scales of the electrically induced insulator-to-metal transition

Theodor Luibrand,[1,*] Adrien Bercher,[2,*] Rodolfo Rocco ,[3,*] Farnaz Tahouni-Bonab ,[1] Lucia Varbaro ,[2]
Carl Willem Rischau ,[2] Claribel Domínguez,[2] Yixi Zhou,[2] Weiwei Luo,[2] Soumen Bag ,[3] Lorenzo Fratino ,[3,4]
Reinhold Kleiner,[1] Stefano Gariglio ,[2] Dieter Koelle ,[1] Jean-Marc Triscone,[2] Marcelo J. Rozenberg,[3]
Alexey B. Kuzmenko,[2] Stefan Guénon ,[1] and Javier del Valle [2,5,†]

[1]*Physikalisches Institut, Center for Quantum Science (CQ) and LISA⁺, Eberhard Karls Universität Tübingen,
Auf der Morgenstelle 14, Tübingen 72076, Germany*
[2]*Department of Quantum Matter Physics, University of Geneva, 24 Quai Ernest-Ansermet, 1211 Geneva, Switzerland*
[3]*Université Paris-Saclay, CNRS Laboratoire de Physique des Solides, 91405, Orsay, France*
[4]*Laboratoire de Physique Théorique et Modélisation, CNRS UMR 8089, CY Cergy Paris Université, 95302 Cergy-Pontoise Cedex, France*
[5]*Department of Physics, University of Oviedo, C/ Federico García Lorca 18, 33007 Oviedo, Spain*

Some correlated materials display an insulator-to-metal transition as the temperature is increased. In most cases, this transition can also be induced electrically, resulting in volatile resistive switching due to the formation of a conducting filament. While this phenomenon has attracted much attention due to potential applications, many fundamental questions remain unaddressed. One of them is its characteristic lengths: What sets the size of these filaments, and how does this impact resistive switching properties? Here, we use a combination of wide-field and scattering-type scanning near-field optical microscopies to characterize filament formation in $NdNiO_3$ and $SmNiO_3$ thin films. We find a clear trend: Smaller filaments increase the current density, yielding sharper switching and a larger resistive drop. With the aid of numerical simulations, we discuss the parameters controlling the filament width and, hence, the switching properties.

I. INTRODUCTION

Many correlated materials, such as the vanadate and rare-earth nickelate families, are well-known for their insulator-to-metal transition (IMT) [1–3]. The transition into the metallic state can be induced by increasing temperature, adding dopants, or applying high pressures [4–6], but it can also be triggered electrically [7–12]. A large enough applied voltage or current can create a percolative metallic filament due to Joule heating [13], drastically reducing the resistance of the system [14–20]. We must note that this filament is not caused by the diffusion of ions under strong electric fields, as commonly observed in resistive random access memories [21], but rather by a local phase transition from insulator to metal. When the voltage (current) is removed, the filament disappears, resulting in volatile resistive switching [22]. This phenomenon has attracted a lot of attention due to promising applications in emerging technologies, such as emulating neuronal spiking for neuromorphic computing [23–29], probabilistic bits for stochastic computing [30–32], or serving as electro-optical switches for optoelectronics [33–37]. Despite

this, many fundamental aspects of the electrically induced IMT are poorly understood. One of the most salient issues is the typical length scale of this process: What sets the size of the metallic filaments or the number of them? Similarly, how do these characteristic lengths affect the resistive switching properties, i.e., the sharpness of the switch ($\partial V/\partial I$) or the total resistive drop? Understanding this is not only of fundamental interest but also key for designing device applications.

Here, we use a combination of wide-field optical microscopy [38] and scattering-type scanning near-field optical microscopy (s-SNOM) [39] to characterize filament length scales during the electrically induced IMT in $NdNiO_3$ and $SmNiO_3$ microdevices. These compounds are two well-known members of the rare-earth nickelate family [2,6]. They both display an IMT concomitant with a structural phase transition, but there are rather important differences between the two. $NdNiO_3$ has a sharp IMT ∼120 K (depending on epitaxial strain) with a resistivity drop of more than two orders of magnitude [Fig. 1(a)]. $SmNiO_3$ on the other hand, displays a smooth IMT ∼400 K, with an order of magnitude resistivity change [2,6]. Such different IMTs allow us to contrast the results from both materials and to determine which parameters govern filament length scales.

II. METHODS

We fabricated two-terminal microdevices on top of our $NdNiO_3$ and $SmNiO_3$ films, as depicted in Fig. 1(b). The nickelate films (∼40 nm thick, Fig. 6 in the Supplemental Material [40]) were grown on $LaAlO_3$ (001) substrates

---

*These authors contributed equally to this work.
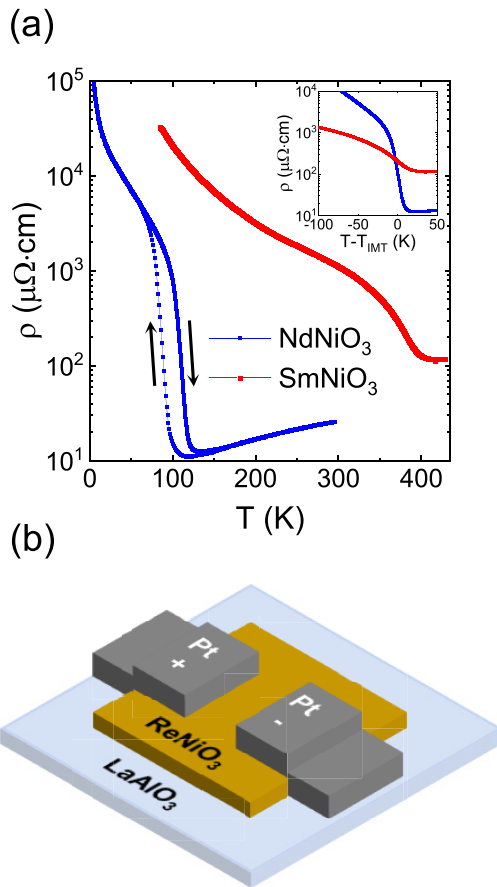
†javier.delvalle@uniovi.es

(a)

(b)

FIG. 1. Sample characteristics. (a) Resistivity vs temperature for ~40-nm-thick NdNiO$_3$ (blue) and SmNiO$_3$ (red) thin films. Inset: Resistivity plotted as a function of T-T_{IMT}. T_{IMT} was calculated finding the maximum of $\partial \log(\rho)/\partial T$, where ρ is the resistivity. Only the warmup branch is shown. (b) Schematic representation of the two-terminal devices. Nickelate islands (brown) were patterned on top of a LaAlO$_3$ substrate (blue). Two platinum electrodes (gray) were used to electrically trigger the insulator-to-metal transition (IMT). The schematic is not at scale.

using off-axis magnetron sputtering. We used a combination of optical lithography and ion etching to define isolated 360 × 130 μm nickelate islands, on top of which we patterned two planar Pt electrodes using a second optical lithography and on-axis Pt sputtering (see Appendix A). The electrodes are 20 μm wide, with a 20 μm gap between them (10 × 10 μm for the s-SNOM experiments). The IMT can be triggered by applying a large enough voltage or current across the gap. To image this phenomenon, we take advantage of the large reflectivity change across the IMT [10]. We use optical microscopy to capture the distribution of metallic/insulating domains in the gap between electrodes [18]. We do so *in operando*, i.e., while applying a variable bias current, which allows us to capture clear images of the percolating filament (see Appendix B).

III. EXPERIMENTAL RESULTS

Figure 2(a) shows the voltage V as a function of the current I in a NdNiO$_3$ microdevice at several temperatures below

the IMT temperature, i.e., the film is in the insulating state when no current is applied. As the current is ramped up, the voltage rises steeply until a threshold is reached, after which a steep voltage reduction takes place. Such a drop marks the moment when the electrically induced IMT occurs and a filament percolates between the electrodes. This is a well-known phenomenon [14–20], and it can be readily observed with our imaging setup. The filament widens when current is further increased, shrinks for decreasing current, and disappears at low enough current values (see Appendix D and the Supplemental Material [40]), in accordance with the volatile V-I curves in Fig. 2(a). We must note that some of the V-I curves feature two discontinuities. In the current range between them, the system is not stationary but rapidly oscillates between a high and a low resistance state, as further discussed in Appendix E. As expected, we find the filament width to be strongly dependent on the bias current, like what has been reported in previous works [15,16,18]. The bulk of this paper focuses on how other factors, such as temperature or material properties, also play a key role at setting filament size.

Figure 2(a) shows a clear trend: The voltage drop becomes sharper and larger as the temperature is lowered. This feature is also observed in SmNiO$_3$ microdevices [Fig. 2(d)], where resistive switching at room temperature is modest, very gradual, and without discontinuities. As the temperature is lowered, the drop becomes steeper and discontinuous. Comparing NdNiO$_3$ and SmNiO$_3$, resistive switching is sharper for the former. Figures 2(b) and 2(e) show optical microscopy images of filaments in NdNiO$_3$ and SmNiO$_3$, respectively, for the same applied current, $I = 20$ mA. Images at two different temperatures are displayed for each material, showing distinctively thinner filaments at lower temperatures in both cases. This is better appreciated in Figs. 2(c) and 2(f), where filament width (for $I = 20$ mA) is plotted as a function of temperature. Lower temperatures yield thinner filaments and, therefore, higher current densities. Moreover, comparing NdNiO$_3$ and SmNiO$_3$, we can see that filaments are much thinner in NdNiO$_3$. Therefore, for a fixed bias current, the filament size is strongly dependent on the material and the base temperature. Figure 2 as a whole establishes a strong connection between filament size and V-I characteristics: Thinner filaments (higher current densities) lead to sharper and larger resistive switching.

While optical microscopy is a versatile tool to visualize metallic/insulating areas at multiple temperatures and currents, its spatial resolution is limited by diffraction. To get more detailed images, we performed *in operando* cryogenic s-SNOM measurements in NdNiO$_3$ devices, using a setup such as the one depicted in Fig. 3(a). The spatial resolution of this atomic force microscopy (AFM)-based technique is limited only by the tip radius (~20 nm) [39], allowing us to obtain high-resolution AFM and near-field images of the filaments. Figures 3(b) and 3(c) show topography and s-SNOM images at 18 and 70 K, respectively. Images for 0, 10, and 20 mA are displayed. For similar currents, filaments are thinner at lower temperatures, in accordance with wide-field optical images in Fig. 2. Moreover, s-SNOM allows us to resolve clear qualitative differences between both temperatures. Images taken at 18 K show a single, intense filament percolating between electrodes, while at higher temperature multiple filaments appear.
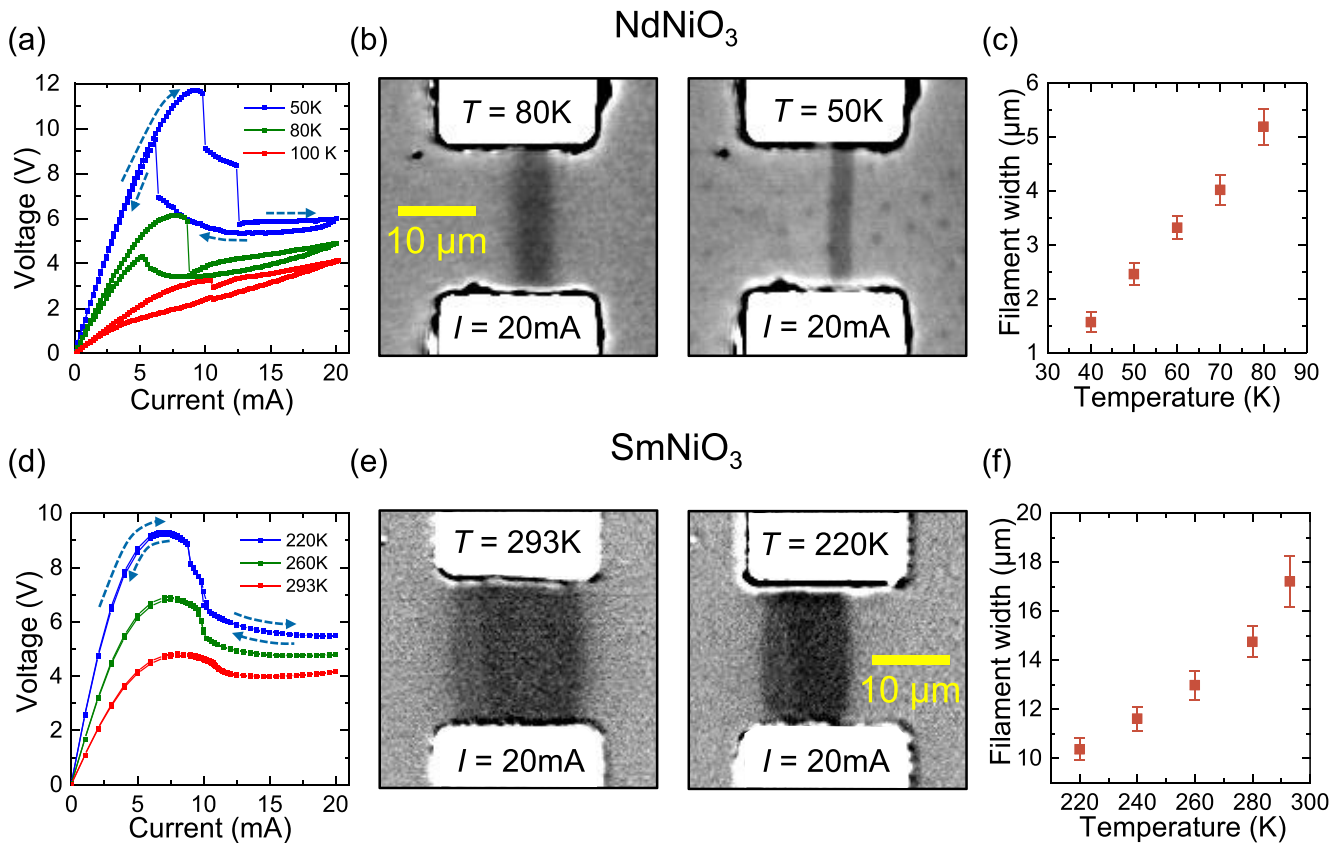
FIG. 2. Connection between resistive switching properties and filament size. (a) and (d) Voltage vs current curves for NdNiO$_3$ and SmNiO$_3$ microdevices, respectively. Several temperatures are plotted for each material. (b) and (e) Wide-field optical microscopy images of filaments in NdNiO$_3$ and SmNiO$_3$, respectively. Current is 20 mA for all four images. Two different temperatures are shown for each material. For the NdNiO$_3$ images, reflectivity was normalized using a region far from the gap. For SmNiO$_3$, differential images are shown, where at each point, the reflectivity at $I = 0$ mA is subtracted. (c) and (f) Filament width vs temperature at $I = 20$ mA. The width was determined using a Gaussian fitting of line scans perpendicular to the filament direction, taking the full width at half maximum as filament width. The error bars show the standard deviation of the distribution of widths.

Thus, lower temperatures favor a winner-takes-all situation in which a single filament carries all the current.

IV. RESISTOR NETWORK SIMULATIONS

To understand these results, we performed numerical simulations in which we model our system as a two-dimensional resistor network [Fig. 4(a)] [10,25]. Each node in the network can be either metallic or insulating, depending on the local temperature and a Landau free energy functional that mimics the IMT. The insulating state resistivity increases as the temperature is decreased, following a variable range hopping dependence [inset of Fig. 4(b)]. Currents and voltages at each node are calculated by solving Kirchhoff's laws. Local temperature is updated in each simulation time step, considering Joule heating and heat conduction. Each node of the network dissipates heat horizontally to its neighbors and vertically to the underlying substrate. We keep the substrate temperature constant, without gradients, which means we do not consider horizontal heat flow through the substrate. However, this contribution can also be captured by our model since it would effectively result in a renormalization of the lateral heat con-

ductivity through the film. A more detailed description of the simulations can be found in Appendix C. This simple model reproduces experimental results with only a few parameters [Fig. 4(b)], allowing us to identify which ones play a key role.

Figure 4(c) shows simulated two-dimensional resistivity maps of the devices for three different values of current and base temperature. As expected, filaments are strongly dependent on the bias current. Also, like the experiments, filaments become narrower as the base temperature is lowered. The material confines current flow into a smaller region at lower temperatures. This in turn induces higher current densities, increasing local Joule heating and greatly affecting the temperature distribution across the device, as can be seen in Fig. 4(d). As the filament narrows, its inner temperature increases. Therefore, thinner filaments induce a stronger current-temperature feedback, which is a key factor controlling switching dynamics [10,19,30]. Strong feedback makes the device susceptible to runaway effects which manifest as discontinuities in the experimental V-I curves [30]. As a result, the thinner the filament and the higher its current-temperature feedback, the larger the discontinuities in the V-I curves. Experimentally, such
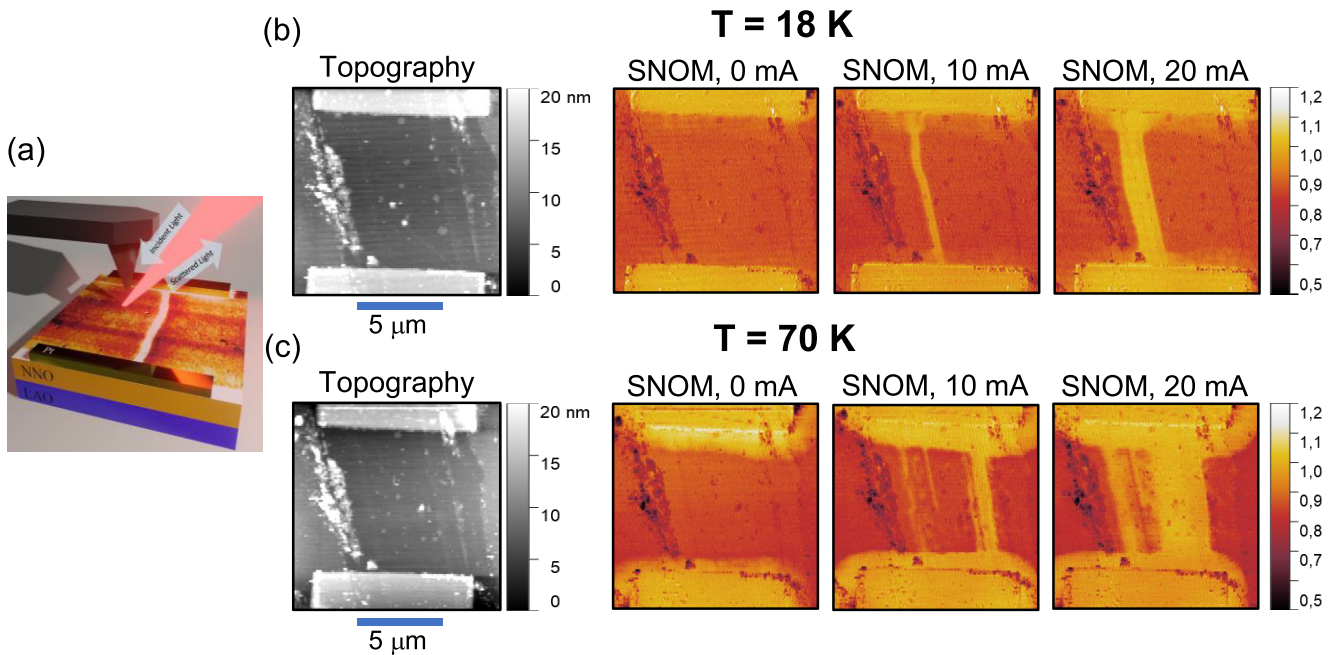
FIG. 3. High-resolution scattering-type scanning near-field optical microscopy (s-SNOM) imaging and presence of multiple percolating filaments. (a) Schematic representation of the s-SNOM setup. Infrared light (wavelength 10 µm) is focused at a metal-coated atomic force microscopy (AFM) tip, which further focuses light into an area comparable to the tip radius (∼20 nm). The tip-scattered signal is determined by the optical conductivity of the area of the material directly underneath the tip, allowing us to get high-resolution images of metallic (high signal) and insulating (low signal) domains. The AFM works in tapping mode and the s-SNOM signal is detected at the third and second harmonic to filter out the far-field component, as described in Appendix B. (b) and (c) Topography and s-SNOM amplitude images for $NdNiO_3$ microdevices at $T = 18$ and 70 K, respectively. The s-SNOM signal was normalized using the Pt electrode as reference. s-SNOM data for three different current values is shown. At 70 K, the $NdNiO_3$ surrounding the Pt electrodes exhibits an enhanced conductivity even in the absence of current, likely caused by a slight T_{IMT} depression in that area. Although we do not know for certain, this could be caused by the lithographic process or by electrode-induced strain or doping [41].

discontinuities are observed to be bigger and more frequent at lower temperatures, especially for $NdNiO_3$. These are the same conditions in which the thinnest filaments are observed.

V. DISCUSSION

Since filament size determines switching properties, it is key to identify which parameters control the ability of the material to confine current into smaller or larger areas. Here, we analyze two contributions: the resistivity difference across the IMT and the thermal conductivity of the substrate. The resistivity contrast between the insulating (ρ_{ins}) and metallic (ρ_{met}) phases is expected to play a major role since it corresponds to the resistivities outside and inside the filament. When $\rho_{ins} \gg \rho_{met}$, the current is strongly focused into the filament, reducing Joule heating outside. This keeps the insulating areas cold and confines the filament in a small region. However, as ρ_{ins} decreases, the insulator becomes leaky, allowing current flow and power dissipation outside the filament and reducing its confinement.

The temperature dependence of the resistivity implies that, as temperature increases, so does power dissipation outside the filament, increasing its width. For instance, the voltage at $I = 5$ a.u. is half as large for $T = 90$ a.u. than for $T = 18$ a.u. [Fig. 4(b)], but the insulating resistivity is ∼8 times smaller. As a result, power dissipation outside the filament

is increased by a factor of 2 at $T = 90$ a.u. vs $T = 18$ a.u. These differences in resistivity explain not only the temperature dependence of the filament size but also the differences observed between $NdNiO_3$ and $SmNiO_3$. The former has a larger resistivity change across the IMT [Fig. 1(a)] [6] and is therefore expected to focus current into thinner filaments. Furthermore, the presence of single or multiple percolating filaments (Fig. 3) can be understood in a similar light. For $\rho_{ins} \gg \rho_{met}$, the current will crowd through the first hotspot that metallizes, favoring a winner-takes-all scenario.

However, the resistivity drop across the IMT is not the only mechanism that can explain the differences in filament size. Thermal properties are also expected to play a crucial role, and they can provide a similarly satisfactory explanation. The thermal conductivity of $LaAlO_3$ is not constant but decreases from 60–70 W/(m K) at 60 K to ∼15 W/(m K) at 300 K [42]. This means that the substrate can more efficiently evacuate heat at lower temperatures, keeping the areas surrounding the filament cold. The filament is therefore confined to a smaller region, as simulations have recently shown [19]. Therefore, thermal properties can also explain the smaller filament size at lower temperatures, as well as accounting for the overall differences between $NdNiO_3$ and $SmNiO_3$, which have IMTs in very different temperature ranges.

Unfortunately, it is difficult to disentangle the contributions due to the resistivity change across the IMT and the substrate thermal conductivity. Both parameters decrease as
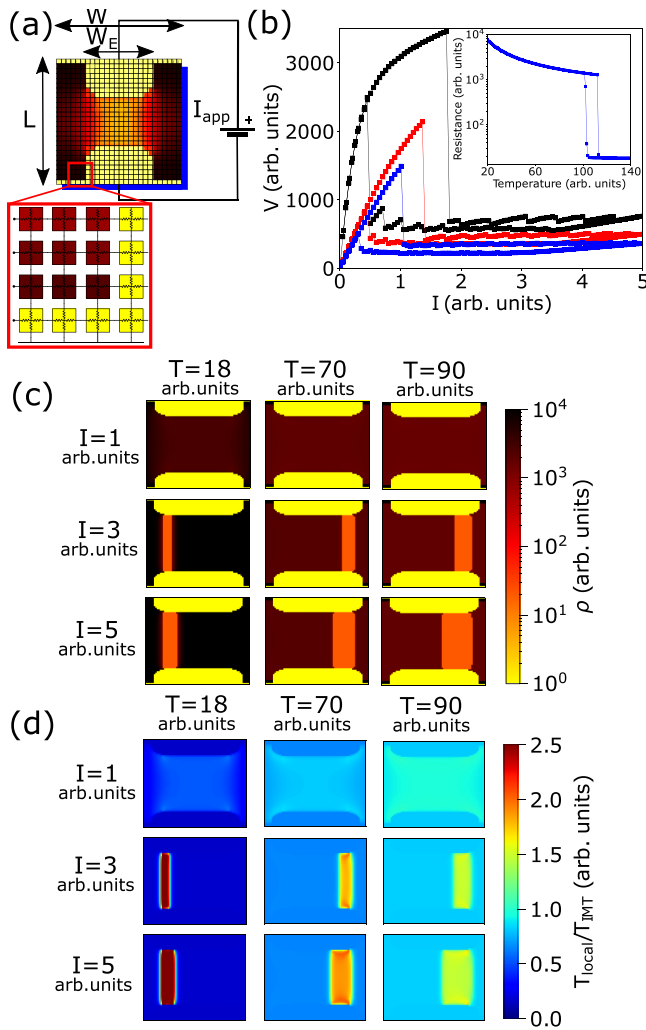
FIG. 4. Resistor network simulations and current focusing effect. (a) Schematic representation of the simulated resistor network (size $W \times L$). Low-resistance electrodes (yellow) define an oxide gap where individual nodes could be either metallic (orange) or insulating (dark brown), as described in Appendix C. (b) Simulated voltage vs current curves for three different temperatures: 18 a.u. (black), 70 a.u. (red), and 90 a.u. (blue). Inset: Simulated resistance vs temperature of the device. (c) Simulated, two-dimensional resistivity plots for all combinations of three currents (1, 3, and 5 a.u.) and three device base temperatures (18, 70, and 90 a.u.). Resistivity is plotted in logarithmic color scale. (d) Simulated, two-dimensional temperature plots for all combinations of three currents (1, 3, and 5 a.u.) and three device base temperatures (18, 70, and 90 a.u.). Temperature is plotted in linear color scale and normalized to the transition temperature (120 a.u.).

temperature is increased. Within the nickelate family, it is observed that, as the transition temperature increases (with the reduction of the rare-earth ion radius), the resistivity drop across the IMT decreases [2,6]. A similar trend is observed in the V_2O_3, VO_2, and V_3O_5 family [10]. Therefore, it is not feasible to compare a material featuring a high-temperature IMT with a large resistivity change with another system having a low-temperature IMT with a small resistivity change.

A way to overcome this drawback is to compare, for the same material, samples with different IMT quality. We fab-

ricated two $NdNiO_3$ films: one with a high-quality IMT and a second one subjected to a 120 °C, 30 min annealing in vacuum. The annealing creates oxygen vacancies, reducing the resistivity change across the IMT, as seen in Fig. 5(a). This has clear consequences in the resistive switching properties, which are smoother for the annealed sample [Fig. 5(b)]. Furthermore, there are notable differences in the filament, as can be seen in Figs. 5(c) and 5(d). The annealed device shows much less contrast and homogeneity within the metallic area, perhaps due to the formation of multiple filaments. This differs from the well-defined, intense filament for the nonannealed sample and points to less metallization and current focusing. This confirms that the resistivity change across the IMT is a key parameter controlling resistive switching and filament characteristics, although it does not rule out important contributions from thermal conductivity.

VI. CONCLUSIONS

In summary, we have used a combination of *in operando* standard and scanning near-field optical microscopies to study the characteristic lengths of filament formation during the electrically induced IMT. We found that, in addition to bias current, filament width is strongly dependent on base temperature and the specific material. Lower setup temperatures yield thinner filaments, increasing current density and local temperature, leading to sharper resistive switching properties. With the aid of resistor network simulations, we discussed the material properties that control filament size, underlining the importance of the resistivity drop across the IMT as well as the thermal conductivity of the substrate.

Our results support recent works concerning another fundamental aspect of the electrically induced IMT: switching dynamics [10,11]. It was proposed that a large resistivity ratio between insulator and metal would induce higher current focusing, increasing local Joule heating within the filament and explaining the different switching timescales observed in V_2O_3, VO_2, V_3O_5, $NdNiO_3$, and $SmNiO_3$. However, direct evidence of this has been lacking so far. In this paper, we provide a systematic study of the characteristic length scales of the electrically induced IMT, unveiling a strong connection between resistivity, thermal properties, filament size, and resistive switching characteristics. The mechanisms outlined here are simple and general and could be applicable to other types of resistive switching, such as ReRAM. Considered together with recent developments in the field [10,11,22], it completes a simple and unified picture of the length and time scales of filament nucleation, growth and relaxation, as well as underlining their importance for developing technologies based on the IMT.
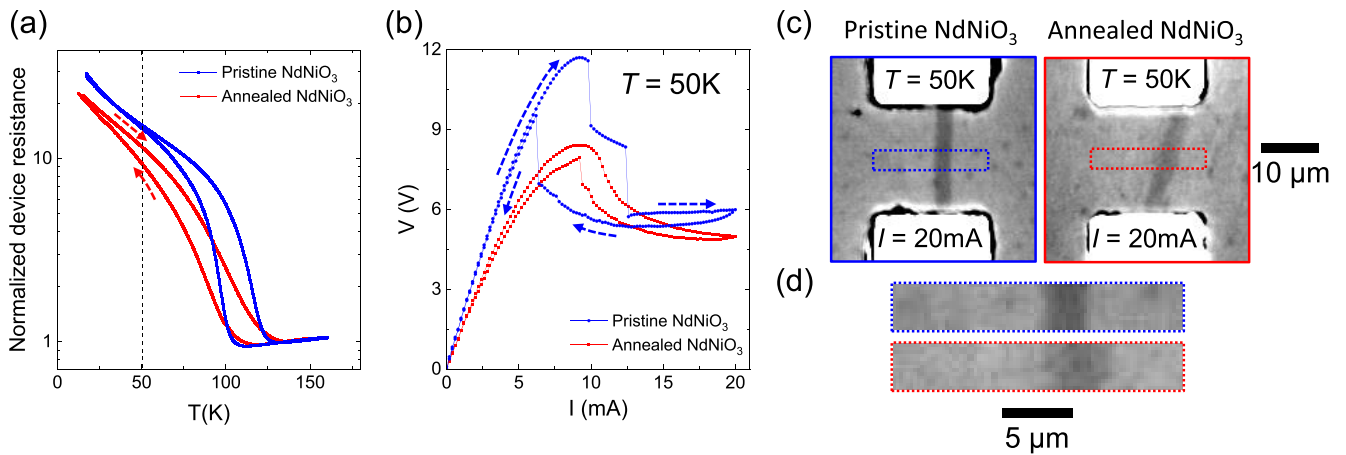
FIG. 5. Resistive switching and filament characteristic in pristine and annealed NdNiO$_3$. (a) Two-probe device resistance vs temperature on pristine (blue) and annealed (red) NdNiO$_3$ films. (b) Voltage vs current at $T = 50$ K for a pristine (blue) and annealed (red) sample. (c) Wide-field microscopy image of filament formation in pristine (left) and annealed (right) NdNiO$_3$. $T = 50$ K and $I = 20$ mA in both cases. Reflectivity was normalized using an area far from the gap region. (d) Zoomed image into the central part of the filament for pristine (top) and annealed (bottom) NdNiO$_3$. $T = 50$ K and $I = 20$ mA in both cases.

APPENDIX A: DEVICE AND THIN FILM STRUCTURE AND FABRICATION

We grew NdNiO$_3$ and SmNiO$_3$ oxide films on (001)-oriented LaAlO$_3$ substrates using off-axis magnetron sputtering in an Ar:O$_2$ (3.5:1) mixture at a pressure of 180 mTorr and substrate temperature of 460 °C. Films are ~40–45 nm thick and grow epitaxially, as can be seen using x-ray diffraction (XRD) [Figs. 6(c) and 6(d)].

For microdevice fabrication, a combination of techniques was used. First, we patterned isolated NdNiO$_3$ and SmNiO$_3$ islands using optical lithography and Ar ion beam milling. This allows us to measure each device independently since it is electrically isolated from the others. After this, we patterned Pt electrodes on top of these islands. For that, we used optical lithography followed by on-axis Pt sputtering at room temperature and a lift-off in acetone. Pt thickness is ~40 nm. and the gap size is 20×20 μm. For the s-SNOM measurements, a further lithographic step was used. Optical lithography does not create smooth electrode edges. This is very challenging for SNOM since the tip is tripped by the electrode irregularities. To improve this, we used electron beam lithography and a second Pt evaporation to define 10×10 μm electrodes with smooth edges.

APPENDIX B: MICROSCOPY TECHNIQUES

We used an optical wide-field microscope that facilitates simultaneous imaging and electrical transport measurements [38]. The device under investigation is mounted in vacuum, on the cold finger of a liquid Helium continuous flow cryostat with a temperature range between 4.2 and 300 K. The microscope has a spatial resolution of 500 nm, the illumination is a monochromatic LED with a wavelength of 532 nm, and the maximum field of view is ~500×500 μm. The electric transport properties were measured in a two-probe configuration. For NdNiO$_3$, we used a Keithley 2400 SourceMeter configured as a current source, whereas we used a highly stable self-built current source for SmNiO$_3$.

Image Processing: For NdNiO$_3$, the gray values were normalized to a NdNiO$_3$ area that is not influenced by the resistive switching (not between the electrodes). For SmNiO$_3$, all the images are differential—the image with zero bias current is subtracted for each current.

A cryogenic s-SNOM system (cryo-neaSNOM from neaspec/attocube GmbH) was used for nanoscopic imaging of the filaments in the devices. Infrared radiation from a Quantum Cascade Laser (Daylight Solutions) was focused at a metal-coated AFM tip (ARROW-NCPt-50 from NanoAndMore GmbH), which was grounded to reduce the electrostatic interaction between the tip and the sample. Despite that, we had to avoid applying voltages >10 V in the microdevices, as it would disturb the AFM in tapping mode. The tip size determines the spatial resolution (20 nm in this case). Pseudo-heterodyne detection allows separating far-field and near-field contributions to the signal by using higher-order tapping harmonics (the ratio between the intensity of the third and second harmonics is used in this paper). The detected near-field signal has an excellent spatial contrast between the insulating and metallic phases because of the large change of the optical
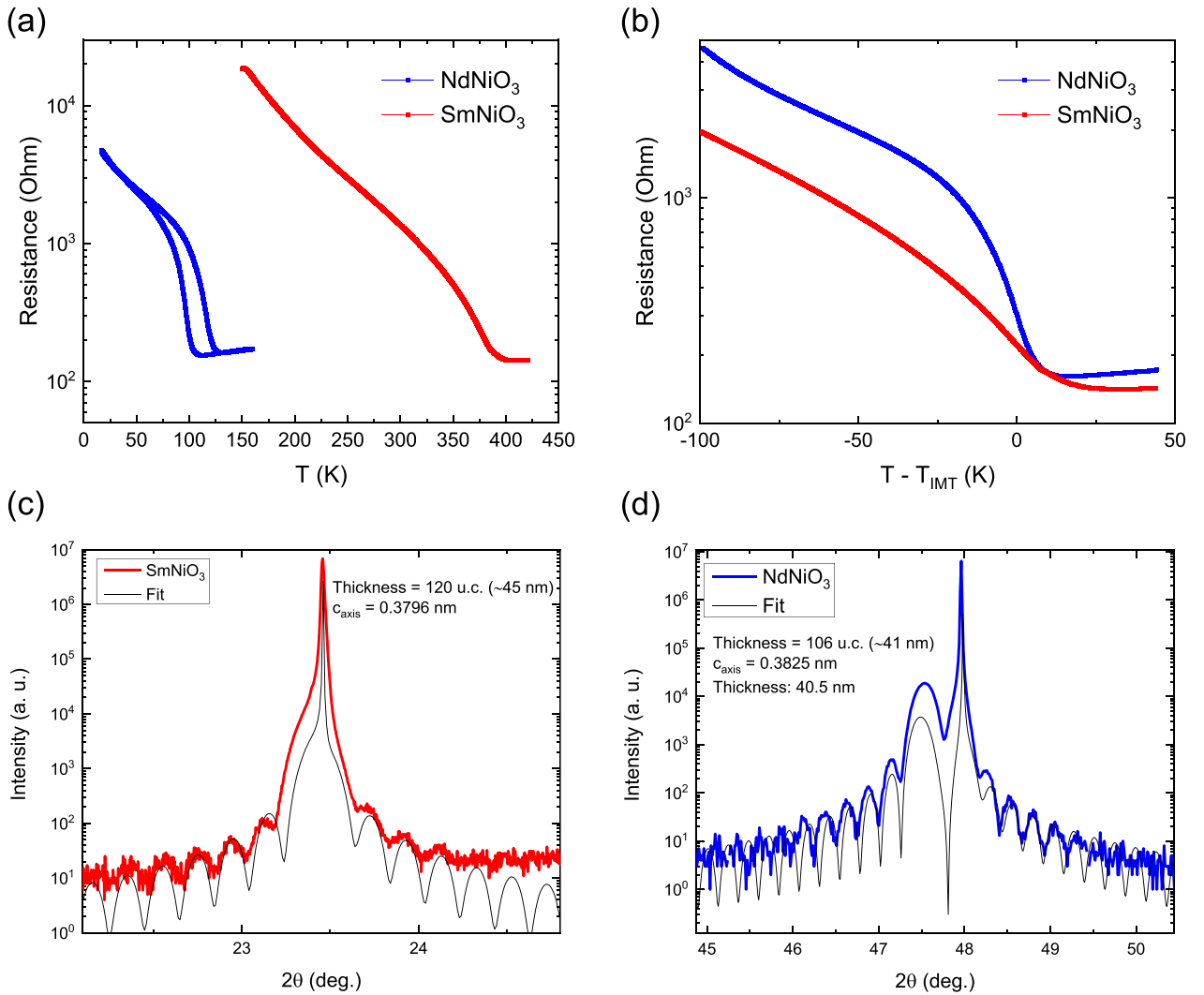
FIG. 6. Structural and transport properties of nickelate films and microdevices. (a) Two-probe resistance vs temperature characteristics of NdNiO$_3$ and SmNiO$_3$ microdevices, respectively. (b) Two-probe resistance plotted as a function of T-T_{IMT}. T_{IMT} was calculated finding the maximum of $\partial \log(\rho)/\partial T$, where ρ is the resistivity. Only the warmup branch is shown. NdNiO$_3$ shows a much sharper insulator-to-metal transition (IMT). (c) and (d) θ-2θ scans of the SmNiO$_3$ and NdNiO$_3$ films, respectively. Scans were performed around the (001) LaAlO$_3$ peak. Finite-sized oscillations are very visible, allowing us to determine the film thickness. Data were manually fitted using the InteractiveXRDfit software [43] and is shown in the plots as continuous dark lines. X-ray diffraction (XRD) shows high-quality epitaxial films with thicknesses ~40–45 nm.

conductivity across the IMT. More information about the s-SNOM operation can be found in Ref. [44].

APPENDIX C: RESISTOR NETWORK SIMULATIONS DETAILS

In the simulations presented in this paper, we use a phenomenological mesoscopic model known as the Mott Resistors Network [19,45]. The model describes the material as a matrix of cells, each containing four resistors, which connect the cell to its four nearest neighbors. Each cell corresponds to a small region of the material of the order of 10 nm. This scale is chosen to define a phase for the cell, which can be insulating or metallic. At first, all the resistors are initialized to a high insulating value, and all the cells are in the insulator phase. A voltage is applied to the mesh through the

metallic electrodes that are situated at the top and the bottom, and currents begin to circulate in the resistor network. These currents can be computed, knowing the initial resistance and the applied voltage, using Kirchhoff laws. When the current I flows through the resistors R_{ij}, these generate heat according to Joule's law, with power $P = I^2R$. The heat generated by a cell is given by the sum of the contributions of its four resistors:

$$P_{ij}(t) = \left[I_1^2(t) + I_2^2(t) + I_3^2(t) + I_4^2(t) \right] R_{ij}(t),$$

where t indicates time in units of the simulation time step, ij are the indexes which identify the cell, P_{ij} is the power generated by the cell, R_{ij} is the resistance of the four resistors (which are always assumed to share the same value), and $I_1, I_2, I_3,$ and I_4 are the four currents flowing through them. Setting to unity the geometrical dimension of the cell, we can
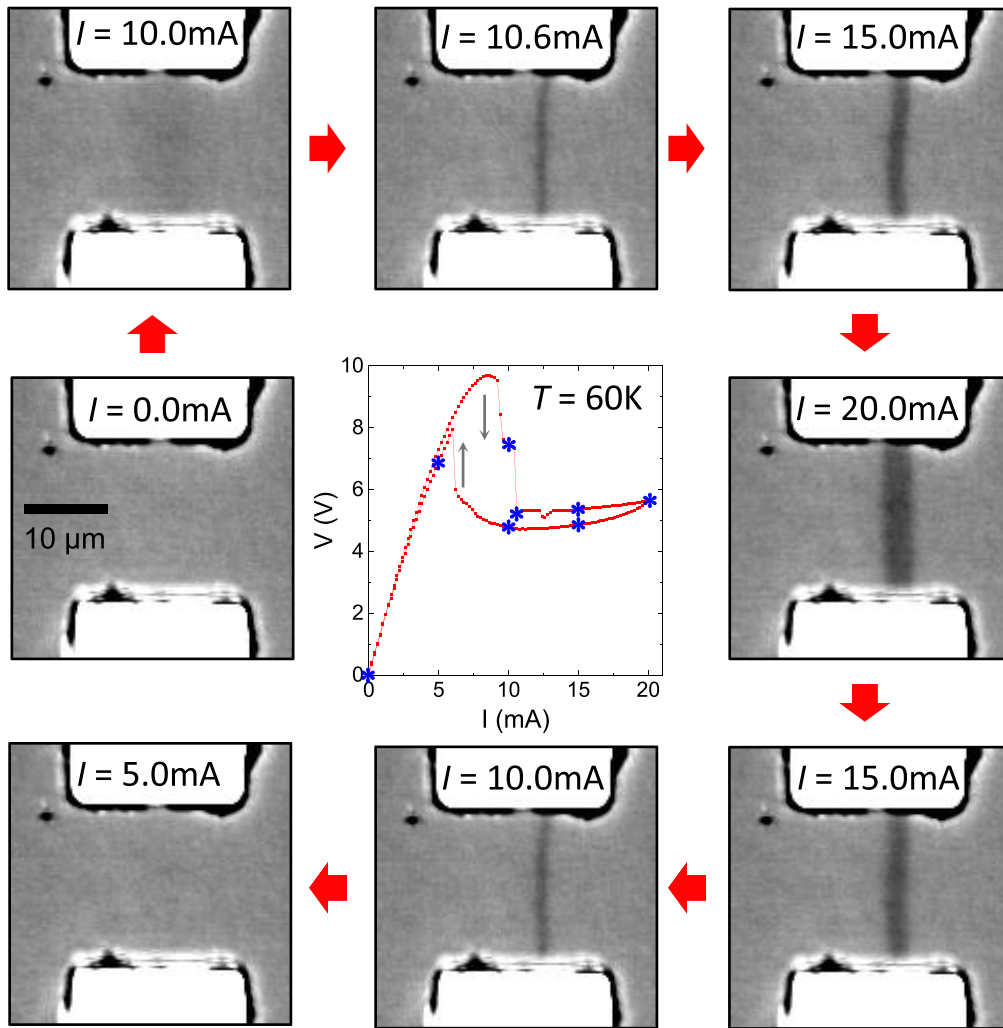
FIG. 7. Filament size dependence on applied current. Central panel: *V*-*I* characteristics of a NdNiO$_3$ microdevice at $T = 60$ K. Blue asterisks mark currents at which the outer panels where captured. Outer panels: Standard optical microscope images of the devices at different applied currents.

identify the resistivity of the cell with R_{ij}. The temperature of the cell will be the result of two contributions: Joule heating and a dissipative term that includes the dissipation to the nearest-neighbor cells and the dissipation to a substrate at a fixed temperature T_0, with which all the cells are in contact. Therefore, using the heat transfer equation, we can write the temperature of the cell as follows:

$$T_{ij}(t) = T_{ij}(t-1) + \frac{P_{ij}(t)}{C}$$
$$- \frac{K}{C}\left[5T_{ij}(t-1) - \sum_{kl}^{NN} T_{kl}(t-1) - T_0\right],$$

where K is the thermal conductivity, C the thermal capacity, and the sum with indexes kl runs over the nearest-neighbor cells. We note that we have made the nonessential assumption of choosing the same thermal conductivity for the dissipation to the substrate and to the nearest neighbors and that the time step of the simulation Δt is set to unity.

The first-order transition of a cell from the insulator-to-metal phase (and vice versa) is described as a thermally

activated behavior with a probability that depends on the temperature of the cell according to the following Arrhenius-like law:

$$p_{ij}^{a \to b}(t) = \exp\left[\frac{-E_B^{a \to b}(T_{ij})}{T_{ij}(t)}\right],$$

where a and b are the states of cell (insulator or metal), and E_B is the energy barrier that separates the two corresponding local minima as described by the following Landau-type free energy (which is appropriate for a first-order thermally driven transition):

$$f(\eta) = h\eta + p\eta^2 + c\eta^4,$$
$$h = h_1 \frac{T - T_C}{T_C} + h_2,$$
$$p = p_1 \frac{T - T_C}{T_C} + p_2.$$

Here, η is the order parameter, and T_C, h_1, h_2, p_1, and p_2 are constants. The resistivity of the cell is then chosen according

to the state of the cell: low and constant (ρ_{met}) in the metal state and high and temperature dependent in the insulator state [$\rho_{\text{ins}}(T)$]. We choose Mott's equation for variable range hopping [46] to describe the temperature dependence of the resistivity in the insulating state since it has already been used to fit the resistivity of NdNiO$_3$ samples [47,48]:

$$\rho_{\text{ins}}(T) = \rho_0 \exp\left[\Delta\left(\frac{1}{T} - \frac{1}{T_{\text{IMT}}}\right)^{1/4}\right],$$

where Δ is a constant, T_{IMT} is the metal-insulator transition temperature, and $\rho_0 = \rho(T_{\text{IMT}})$ is the resistivity at the transition temperature. Nevertheless, the specific choice of the functional form does not change the main qualitative features of the results. Once the resistivity of the cell has been computed, we can update the resistance of the resistors within it. When all the cells have been updated, the time step is increased by one, and the simulation continues as described above, starting again from the computation of Kirchhoff currents.

APPENDIX D: FILAMENT WIDTH DEPENDENCE ON CURRENT

Apart from temperature and specific material choice (the focus of this paper), filament size depends strongly on the applied current. This is a well-known effect [14–18] (see Supplemental Material [40]). A specific example is given in Fig. 7, which shows images of a NdNiO$_3$ microdevice at different points of a V-I measurement cycle, for a temperature $T = 60$ K. As can be seen, the filament width grows with applied current, appearing and disappearing at the discontinuities of the ramp-up and ramp-down V-I curves, respectively.

APPENDIX E: DEVICE SELF-OSCILLATIONS

Interpretation of filament size is not straightforward for all currents. As can be seen in Figs. 2(a) and 2(d), for some temperatures, there are two voltage discontinuities when current is ramped up (for instance, at $T = 50$ K in NdNiO$_3$). Between the two, there is a range of currents where the V-I curve
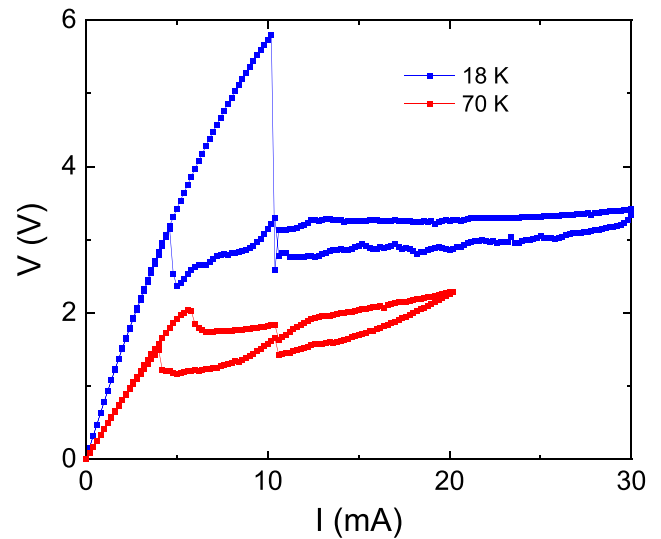

FIG. 8. Voltage vs current in NdNiO$_3$ microdevices, measured in the scattering-type scanning near-field optical microscopy (s-SNOM) setup. The characteristic features caused by device self-oscillation are absent.

is smooth and monotonically decreasing. In that range, the system is not stationary but rather oscillates between two configurations, one with a percolating filament and one without it. These self-oscillations, which are in the 10 kHz range, are a well-known effect [20,49], and they can be observed with an oscilloscope. The parasitic capacitance and the slow reaction time of current source are the main factors determining the oscillation regime. We must note that devices measured in the SNOM setup do not show the V-I characteristics associated with self-oscillations (Fig. 8). This difference is likely due to two main factors: (i) the different device geometry and (ii) the different wiring and parasitic capacitance of both setups.

All the analysis about filament size at different temperatures and materials shown in the paper is done for $I = 20$ mA. This is well above the self-oscillation range, where the system is stationary again, so it does not affect our conclusions.

[1] F. J. Morin, Oxides which Show a Metal-to-Insulator Transition at the Neel Temperature, Phys. Rev. Lett. **3**, 34 (1959).

[2] J. B. Torrance, P. Lacorre, A. I. Nazzal, E. J. Ansaldo, and C. Niedermayer, Systematic study of insulator-metal transitions in perovskites RNiO$_3$ (R = Pr, Nd, Sm, Eu) due to closing of charge-transfer gap, Phys. Rev. B **45**, 8209 (1992).

[3] M. Imada, A. Fujimori, and Y. Tokura, Metal-insulator transitions, Rev. Mod. Phys. **70**, 1039 (1998).

[4] S. Lupi, L. Baldassarre, B. Mansart, A. Perucchi, A. Barinov, P. Dudin, E. Papalazarou, F. Rodolakis, J. P. Rueff, J. P. Itié *et al.*, A microscopic view on the Mott transition in chromium-doped V$_2$O$_3$, Nat. Commun. **1**, 105 (2010).

[5] J. H. Park, J. M. Coy, T. Serkan Kasirga, C. Huang, Z. Fei, S. Hunter, and D. H. Cobden, Measurement of a solid-state triple point at the metal–insulator transition in VO$_2$, Nature (London) **500**, 431 (2013).

[6] S. Catalano, M. Gibert, J. Fowlie, J. Iñiguez, J. M. Triscone, and J. Kreisel, Rare-earth nickelates RNiO$_3$: Thin films and heterostructures, Rep. Prog. Phys. **81**, 046501 (2018).

[7] G. Stefanovich, A. Pergament, and D. Stefanovich, Electrical switching and Mott transition in VO$_2$, J. Phys. Condens. Matter **12**, 8837 (2000).

[8] G. Seo, B. J. Kim, C. Ko, Y. Cui, Y. W. Lee, J. H. Shin, S. Ramanathan, and H. T. Kim, Voltage-pulse-induced switching dynamics in VO$_2$, IEEE Electron Device Lett. **32**, 1582 (2011).

[9] P. Diener, E. Janod, B. Corraze, M. Querré, C. Adda, M. Guilloux-Viry, S. Cordier, A. Camjayi, M. Rozenberg, M. P. Besland *et al.*, How a dc Electric Field Drives Mott Insulators Out of Equilibrium, Phys. Rev. Lett. **121**, 016601 (2018).

[10] J. del Valle, N. M. Vargas, R. Rocco, P. Salev, Y. Kalcheim, P. N. Lapa, C. Adda, M.-H. Lee, P. Y. Wang, L. Fratino *et al.*,

Spatiotemporal characterization of the field-induced insulator-to-metal transition, Science **373**, 907 (2021).

[11] J. Del Valle, R. Rocco, C. Domínguez, J. Fowlie, S. Gariglio, M. J. Rozenberg, and J. M. Triscone, Dynamics of the electrically induced insulator-to-metal transition in rare-earth nickelates, Phys. Rev. B **104**, 165141 (2021).

[12] S. K. Das, S. Kumar Nandi, C. Verbel Marquez, A. Rúa, M. Uenuma, E. Puyoo, S. K. Nath, D. Albertini, N. Baboux, T. Lu *et al.*, Physical origin of negative differential resistance in V_3O_5 and its application as a solid-state oscillator, Adv. Mater. 2208477 (2022).

[13] A. Zimmers, L. Aigouy, M. Mortier, A. Sharoni, S. Wang, K. G. West, J. G. Ramirez, and I. K. Schuller, Role of Thermal Heating on the Voltage Induced Insulator-Metal Transition in VO_2, Phys. Rev. Lett. **110**, 056601 (2013).

[14] S. Kumar, M. D. Pickett, J. P. Strachan, G. Gibson, Y. Nishi, and R. S. Williams, Local temperature redistribution and structural transition during joule-heating-driven conductance switching in VO_2, Adv. Mater. **25**, 6128 (2013).

[15] S. Guénon, S. Scharinger, S. Wang, J. G. Ramírez, D. Koelle, R. Kleiner, and I. K. Schuller, Electrical breakdown in a V_2O_3 device at the insulator-to-metal transition, Europhys. Lett. **101**, 57003 (2013).

[16] H. Madan, M. Jerry, A. Pogrebnyakov, T. Mayer, and S. Datta, Quantitative mapping of phase coexistence in Mott-Peierls insulator during electronic and thermally driven phase transition, ACS Nano **9**, 2009 (2015).

[17] S. Kumar and R. S. Williams, Separation of current density and electric field domains caused by nonlinear electronic instabilities, Nat. Commun. **9**, 2030 (2018).

[18] M. Lange, S. Guénon, Y. Kalcheim, T. Luibrand, N. M. Vargas, D. Schwebius, R. Kleiner, I. K. Schuller, and D. Koelle, Imaging of Electrothermal Filament Formation in a Mott Insulator, Phys. Rev. Appl. **16**, 054027 (2021).

[19] R. Rocco, J. Del Valle, H. Navarro, P. Salev, I. K. Schuller, and M. Rozenberg, Exponential Escape Rate of Filamentary Incubation in Mott Spiking Neurons, Phys. Rev. Appl. **17**, 024028 (2022).

[20] C. Adda, M.-H. Lee, Y. Kalcheim, P. Salev, R. Rocco, N. M. Vargas, N. Ghazikhanian, C.-P. Li, G. Albright, M. Rozenberg *et al.*, Direct Observation of the Electrically Triggered Insulator-Metal Transition in V_3O_5 far below the Transition Temperature, Phys. Rev. X **12**, 011025 (2022).

[21] J. J. Yang, D. B. Strukov, and D. R. Stewart, Memristive devices for computing, Nat. Nanotechnol. **8**, 13 (2013).

[22] J. del Valle, P. Salev, F. Tesler, N. M. Vargas, Y. Kalcheim, P. Wang, J. Trastoy, M. H. Lee, G. Kassabian, J. G. Ramírez *et al.*, Subthreshold firing in Mott nanodevices, Nature (London) **569**, 388 (2019).

[23] M. D. Pickett, G. Medeiros-Ribeiro, and R. S. Williams, A scalable neuristor built with Mott memristors, Nat. Mater. **12**, 114 (2013).

[24] M. Ignatov, M. Ziegler, M. Hansen, A. Petraru, and H. Kohlstedt, A memristive spiking neuron with firing rate coding, Front. Neurosci. **9**, 376 (2015).

[25] P. Stoliar, J. Tranchant, B. Corraze, E. Janod, M.-P. P. Besland, F. Tesler, M. Rozenberg, and L. Cario, A leaky-integrate-and-fire neuron analog realized with a Mott insulator, Adv. Funct. Mater. **27**, 1604740 (2017).

[26] J. del Valle, P. Salev, Y. Kalcheim, and I. K. Schuller, A caloritronics-based Mott neuristor, Sci. Rep. **10**, 4292 (2020).

[27] W. Yi, K. K. Tsang, S. K. Lam, X. Bai, J. A. Crowell, and E. A. Flores, Biological plausibility and stochasticity in scalable VO_2 active memristor neurons, Nat. Commun. **9**, 4661 (2018).

[28] S. M. Bohaichuk, S. Kumar, G. Pitner, C. J. McClellan, J. Jeong, M. G. Samant, H. S. P. Wong, S. S. P. Parkin, R. S. Williams, and E. Pop, Fast spiking of a Mott VO_2–carbon nanotube composite device, Nano Lett. **19**, 6751 (2019).

[29] S. Oh, Y. Shi, J. del Valle, P. Salev, Y. Lu, Z. Huang, Y. Kalcheim, I. K. Schuller, and D. Kuzum, Energy-efficient Mott activation neuron for full-hardware implementation of neural networks, Nat. Nanotechnol. **16**, 680 (2021).

[30] S. Kumar, J. P. Strachan, and R. S. Williams, Chaotic dynamics in nanoscale NbO_2 Mott memristors for analogue computing, Nature (London) **548**, 318 (2017).

[31] M. Jerry, K. Ni, A. Parihar, A. Raychowdhury, and S. Datta, Stochastic insulator-to-metal phase transition-based true random number generator, IEEE Electron Device Lett. **39**, 139 (2018).

[32] J. del Valle, P. Salev, S. Gariglio, Y. Kalcheim, I. K. Schuller, and J.-M. Triscone, Generation of tunable stochastic sequences using the insulator–metal transition, Nano Lett. **22**, 1251 (2022).

[33] S. Cueff, J. John, Z. Zhang, J. Parra, J. Sun, R. Orobtchouk, S. Ramanathan, and P. Sanchis, VO_2 nanophotonics, APL Photonics **5**, 110901 (2020).

[34] G. Li, D. Xie, H. Zhong, Z. Zhang, X. Fu, Q. Zhou, Q. Li, H. Ni, J. Wang, E. jia Guo *et al.*, Photo-induced non-volatile VO_2 phase transition for neuromorphic ultraviolet sensors, Nat. Commun. **13**, 1729 (2022).

[35] I. Olivares, J.-P. Locquet, J. Parra, L. D. Sánchez, M. Menghini, P. Sanchis, and P. Homm, Experimental demonstration of a tunable transverse electric pass polarizer based on hybrid VO_2/silicon technology, Opt. Lett. **43**, 3650 (2018).

[36] K. J. Miller, K. A. Hallman, R. F. Haglund Jr, and S. M. Weiss, Silicon waveguide optical switch with embedded phase change material, Opt. Express **25**, 26527 (2017).

[37] D. Lee, J. Lee, K. Song, F. Xue, S. Y. Choi, Y. Ma, J. Podkaminer, D. Liu, S. C. Liu, B. Chung *et al.*, Sharpened VO_2 phase transition via controlled release of epitaxial strain, Nano Lett. **17**, 5614 (2017).

[38] M. Lange, S. Guénon, F. Lever, R. Kleiner, and D. Koelle, A high-resolution combined scanning laser and widefield polarizing microscope for imaging at temperatures from 4 K to 300 K, Rev. Sci. Instrum. **88**, 123705 (2017).

[39] K. W. Post, A. S. McLeod, M. Hepting, M. Bluschke, Y. Wang, G. Cristiani, G. Logvenov, A. Charnukha, G. X. Ni, P. Radhakrishnan *et al.*, Coexisting first- and second-order electronic phase transitions in a correlated oxide, Nat. Phys. **14**, 1056 (2018).

[40] See Supplemental Material at http://link.aps.org/supplemental/10.1103/PhysRevResearch.5.013108 for videos showing the current dependence at different temperatures.

[41] E. Sediva, W. J. Bowman, J. C. Gonzalez-Rosillo, and J. L. M. Rupp, Investigation of the eightwise switching mechanism and its suppression in $SrTiO_3$ modulated by humidity and interchanged top and bottom platinum and $LaNiO_3$ electrode contacts, Adv. Electron. Mater. **5**, 1800566 (2018).

[42] W. Schnelle, R. Fischer, and E. Gmelin, Specific heat capacity and thermal conductivity of $NdGaO_3$ and $LaAlO_3$ single crystals at low temperatures, J. Phys. D: Appl. Phys. **34**, 846 (2001).

[43] C. Lichtensteiger, InteractiveXRDFit: A new tool to simulate and fit X-ray diffractograms of oxide thin films and heterostructures, J. Appl. Crystallogr. **51**, 1745 (2018).

[44] X. Chen, D. Hu, R. Mescall, G. You, D. N. Basov, Q. Dai, and Mengkun Liu, Modern scattering-type scanning near-field optical microscopy for advanced material research, Adv. Mater. **31**, 1804774 (2019).

[45] P. Stoliar, L. Cario, E. Janod, B. Corraze, C. Guillot-Deudon, S. Salmon-Bourmand, V. Guiot, J. Tranchant, and M. Rozenberg, Universal electric-field-driven resistive transition in narrow-gap Mott insulators, Adv. Mater. **25**, 3222 (2013).

[46] N. F. Mott, *Metal-Insulator Transitions* (Taylor & Francis, London, 1990).

[47] J. Blasco, M. Castro, and J. Garcia, Structural, electronic, magnetic and calorimetric study of the metal-insulator transition in $NdNiO_{3-\delta}$, J. Phys.: Condens. Matter **6**, 5875 (1994).

[48] G. Catalan, R. M. Bowman, and J. M. Gregg, Metal-insulator transitions in $NdNiO_3$ thin films, Phys. Rev. B **62**, 7892 (2000).

[49] Y. W. Lee, B.-J. Kim, J.-W. Lim, S. J. Yun, S. Choi, B.-G. Chae, G. Kim, and H.-T. Kim, Metal-insulator transition-induced electrical oscillation in vanadium dioxide thin film, Appl. Phys. Lett. **92**, 162903 (2008).

Publication 2

Imaging of Electrothermal Filament Formation in a Mott Insulator

Matthias Lange,[1] Stefan Guénon,[1,][*] Yoav Kalcheim,[2,3] Theodor Luibrand,[1]
Nicolas M. Vargas,[2] Dennis Schwebius,[1] Reinhold Kleiner,[1] Ivan K. Schuller,[2] and
Dieter Koelle[1]

[1]*Physikalisches Institut, Center for Quantum Science (CQ) and LISA+, Eberhard Karls Universität Tübingen,
Auf der Morgenstelle 14, Tübingen 72076, Germany*

[2]*Center for Advanced Nanoscience, Department of Physics, University of California—San Diego,
9500 Gilman Drive, La Jolla, California 92093-0319, USA*

[3]*Department of Materials Science and Engineering, Technion—Israel Institute of Technology, Technion City,
Haifa 32000, Israel*

Resistive switching—the current- and voltage-induced change of electrical resistance—is at the core of memristive devices, which play an essential role in the emerging field of neuromorphic computing. This study is about resistive switching in a Mott insulator, which undergoes a thermally driven metal-to-insulator transition. Two distinct switching mechanisms are reported for such a system: electric-field-driven resistive switching and electrothermal resistive switching. The latter results from an instability caused by Joule heating. Here, we present the visualization of the reversible resistive switching in a planar V_2O_3 thin-film device using high-resolution wide-field microscopy in combination with electric transport measurements. We investigate the interaction of the electrothermal instability with the strain-induced spontaneous phase separation in the V_2O_3 thin film at the Mott transition. The photomicrographs show the formation of a narrow metallic filament with a minimum width $\lesssim 500$ nm. Although the filament formation and the overall shape of the current-voltage characteristics (IVCs) are typical of an electrothermal breakdown, we also observe atypical effects such as oblique filaments, filament splitting, and hysteretic IVCs with sawtoothlike jumps at high currents in the low-resistance regime. We are able to reproduce the experimental results in a numerical model based on a two-dimensional resistor network. This model demonstrates that resistive switching in this case is indeed electrothermal and that the intrinsic heterogeneity is responsible for the atypical effects. This heterogeneity is strongly influenced by strain, thereby establishing a link between switching dynamics and structural properties.

I. INTRODUCTION

The strongly correlated electron system V_2O_3 is a prototypical Mott-Hubbard insulator [1]. At room temperature, stoichiometric V_2O_3 is a paramagnetic metal with corundum structure, which undergoes a metal-to-insulator transition (MIT) in cooling below about 160 K. The insulating phase is antiferromagnetic with monoclinic structure. Upon heating, the insulating phase undergoes a thermally driven insulator-to-metal transition (IMT) [2–4].

In recent years, there has been a growing interest in utilizing the MIT-IMT in devices based on strongly correlated oxides [5]. One area of application is optical elements, where the MIT-IMT influences the photonic properties [6,7]. Another area of application is resistive switching, where an applied electric current or field induces the IMT and changes the resistance of the device [8,9]. Two technological problems fuel the research in resistive

switching. First, there is growing interest in resistive random access memories (RRAMs) as next-generation energy-efficient nonvolatile computer memories. Here, high- and low-resistive states in memristive elements store the data [10–12]. Second, the era of "Big Data" requires methods to access huge data-storage capacities efficiently, which fuels the research field of in-memory computing—combining data storage and logical operations in one chip. At the core of this technology are again memristive elements [13–15]. A subfield of in-memory computing is neuromorphic computing—the search for physical phenomena and concepts that allow the building of artificial neural networks with some of the essential functions of their biological counterparts. Again, memristive elements utilizing resistive switching play a vital role in this emerging research field [16–22].

Several mechanisms have been suggested for resistive switching in Mott insulators. At very high fields ($\gtrsim 100$ MV/m), Landau-Zener tunneling across the Mott gap increases the free-carrier concentration, which

*stefan.guenon@uni-tuebingen.de

eventually destabilizes the insulating state, leading to the IMT [23–27]. However, switching with considerably lower fields has been observed in some cases [28–30]. The low-field switching has been attributed to midgap tunneling [31,32], to an electric-field-driven Mott-gap collapse [33], or to a spatially inhomogeneous metal-insulator mixed state [34].

In addition to these mechanisms, in materials exhibiting a thermally driven IMT, a universal electrothermal break-down must be considered. This instability is not directly related to the Mott-Hubbard physics, but is the result of an electrothermal instability created by the strong temperature dependence of the electric resistivity at the IMT [35–40]. Such an electrothermal instability can lead to resistive switching. When current passes through a highly resis-tive (insulating) device, Joule heating increases the device temperature. Consequently, small spatial variations in the current density may lead to spatial variations of the local device temperature. The sharp decrease in the resistivity with increasing temperature (at the IMT) acts as a positive-feedback mechanism, which amplifies the evolution of a spatially inhomogeneous state. For electric currents above a certain threshold, this may lead to a runaway effect where more and more current is concentrated in a small section of the device, considerably increasing the local temperature. This runaway effect results in the formation of a highly conductive (metallic) filament connecting the device elec-trodes. The filament is sustained in the metallic state by the Joule heating concentrated within it, while its surroundings remain in the insulating state at the lower base temperature. In this case, resistive switching is the result of current and temperature redistribution in the device (for an extensive discussion of this phenomenon, see Ref. [41]).

Considering V_2O_3 devices, it is possible to suppress the electrothermal effects and enter a purely electronic regime in ultrafast pump-probe experiments [42]. In a study on V_2O_3 nanodevices, where size effects and electrode cool-ing reduced Joule heating, evidence for a dielectric break-down has been found [30] and, in a recent study, the authors have found that defects in the V_2O_3 thin films enhance the efficiency of field-assisted carrier genera-tion and considerably reduce the threshold for a dielectric (nonthermal) breakdown [43]. Electrothermal switching is therefore expected in large and highly pure devices where cooling from the contacts is inefficient and defects do not play a substantial role in the switching process. More-over, we note that due to the elastic strain and coupling between the structural and the electronic degrees of free-dom, V_2O_3 thin films on single-crystal substrates have very rich physics on their own [44–49]. Of particular impor-tance is the spontaneous phase separation with herringbone domain structures at the submicrometer scale due to strain minimization at the MIT-IMT [50]; this in turn is likely to also affect resistive switching at the IMT.

Despite major research efforts, the details of the resistive-switching mechanism remain elusive. In partic-ular, for systems with a thermally driven IMT, the ques-tion of purely electrically versus electrothermally induced resistive switching has been debated over recent years [9,30,34,36,37,43,51–54]. A fundamental problem for understanding voltage- or current-induced switching is based on the fact that in experiments, the switching is ana-lyzed by electric transport measurements. Naturally, those measurements are only sensitive to the total resistance change of the device. However, the system is inherently strongly inhomogeneous, eventually including a strongly inhomogeneous spatial distribution of current density and temperature. Consequently, knowledge of the spatial dis-tribution of those properties that are relevant for resistive switching is crucial. Hence, it should be highly rewarding to combine electric transport measurements with imag-ing of filament formation on the submicrometer scale. This may, in particular, provide insights into the relation between strain-induced domain formation and switching-induced filament formation at the MIT-IMT that have hitherto proved to be inaccessible.

In this study, we combine electric transport measure-ments with cryogenic optical wide-field microscopy (with a spatial resolution of about 0.5 μm) on V_2O_3 thin-film devices. Due to different reflectivity, the photomicrographs yield a strong contrast between metallic and insulating regions, which allows for imaging of the metal-insulator spontaneous phase separation at the MIT-IMT and for the determination of the spatial distribution of local MIT and IMT temperatures. Furthermore, we image the evo-lution of the formation of highly conducting (metallic) filaments that accompany resistive switching upon sweep-ing an applied current in the insulating state and recording simultaneously the current-voltage characteristics (IVCs). In this way, the characteristics of the electric transport measurements can be related to the formation, growth, and extinction of metallic filament features at the sub-micron scale. We find that both the IVCs and the pho-tomicrographs have many characteristics of electrothermal resistive switching due to Joule-heating filament forma-tion. However, we also observe details that we assume to result from the interaction of Joule-heating filaments with the strain-induced varying MIT-IMT temperatures. We develop a numerical model based on a two-dimensional (2D) resistor network, which takes into account the exper-imentally determined spatial distribution of the local MIT-IMT temperatures. With this model, we calculate the IVCs and the spatial distribution of the current density and tem-perature upon electrothermal resistive switching and find excellent agreement with experimentally determined IVCs and optically detected filament formation. These results provide a deep understanding of the details of the resistive-switching mechanism at play. In particular, comparing

the spontaneously formed metal-insulator domain structure with the filamentary structures resulting from electrothermal switching also reveals a hitherto unknown interplay between strain and switching.

This paper is organized as follows. After Sec. II, on sample fabrication and the experimental setup, we discuss in Sec. III the thermally driven MIT-IMT in the planar V_2O_3 thin-film device under investigation. In addition to resistance R versus temperature T data (Sec. III A), we present photomicrographs at the MIT-IMT, which show characteristic insulator-metal herringbone domain structures (Sec. III B). Then, in Sec. III C, we derive maps of spatially resolved transition temperatures.

The main results are presented in Sec. IV, on resistive switching by current-induced MIT. There, we show IVCs in combination with photomicrographs at the IMT onset (Secs. IV A and IV B) and discuss the experimental results (Sec. IV C). We then present a numerical model (Sec. IV D), based on a 2D resistor network, which shows good agreement in comparison with the experimental results (Sec. IV E). Section V concludes this work.

II. SAMPLE FABRICATION AND EXPERIMENTAL SETUP

A 300-nm-thick V_2O_3 thin film is grown by rf magnetron sputtering of a V_2O_3 target on an r plane (10$\bar{1}$2) sapphire substrate (for details, see Ref. [55,56]). Subsequently, by an optical lithography lift-off process, we prepare several 100-nm-thick Au contact pads on top of the unpatterned V_2O_3 film, to define 12 devices on the chip. Each device consists of a 19.5-μm-long gap between two 20-μm-wide Au electrodes [see Fig. 1(a)].

We use a wide-field optical microscope [57] with the device mounted in vacuum, in a continuous He gas-flow cryostat. This configuration facilitates electrical transport measurements simultaneously with optical imaging of the device. The microscope has a spatial resolution of about 0.5 μm. The illumination is monochromatic with a wavelength of 528 nm and the field of view is 500 μm $\times$ 500 μm. Optical microscopy allows for imaging the phase separation in the V_2O_3 thin film, because the metallic and insulating phases have different reflectivities
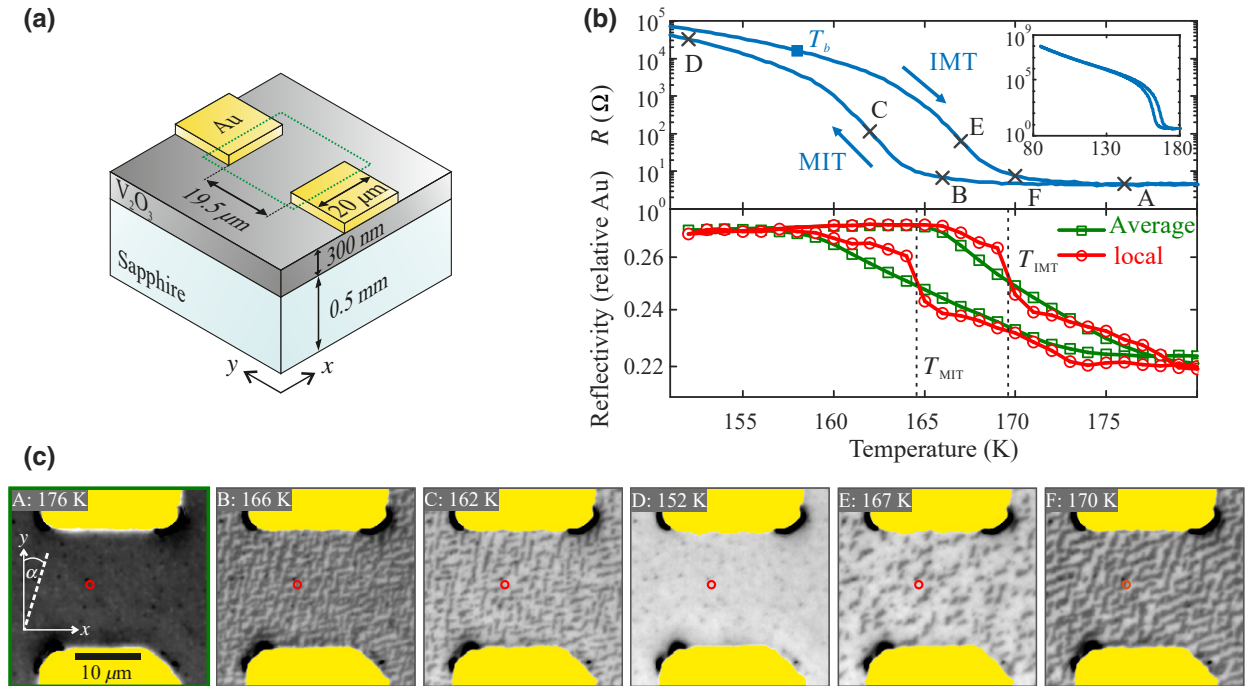

FIG. 1. (a) A schematic view of the planar V_2O_3 device under investigation. The two Au electrodes serve as combined current-voltage taps for two-probe electric transport measurements. The dotted green line indicates the area of interest (the field of view of the images is shown in (c)). (b) Resistively and optically detected MIT-IMT. The upper panel shows the electrical resistance $R(T)$ (measured with $I = 5\ \mu$A); the arrows indicate the sweep direction of the temperature T. Data points marked by letters correspond to images shown in (c). T_b indicates the base temperature set for the measurements presented in Fig. 3. The inset shows $R(T)$, including the lowest temperature of the thermal cycle. The lower panel shows the reflectivity versus T of the V_2O_3 film normalized to the reflectivity of the Au electrodes. The green curve represents the average over the area of interest, while the red curve represents the reflectivity of a single pixel at the location indicated by the red circles in (c). The vertical dashed lines indicate the local transition temperatures T_{MIT} and T_{IMT}, determined for the single pixel. (c) A selection of photomicrographs acquired during one thermal cycle. The Au electrodes are indicated by the yellow areas.

[see Fig. 1(c)]. Note that, counterintuitively, the insulating phase has a higher reflectivity than the metallic phase. The reason for this is that the monochromatic illumination at 528 nm is above the plasma frequency for both phases and therefore the reflectivity contrast is not caused by the concentration of free charge carriers. Instead, e_g^π to a_{1g} (lower Hubbard band) [58,59] interband transitions dominate the insulating-phase reflectivity, while transitions from the quasiparticle peak to the a_{1g} upper Hubbard band [55] dominate the metallic phase reflectivity.

We measure the electric transport properties in a two-point configuration with a Keithley 2400 SourceMeter configured as a current source. IVCs are taken from 0 to 20 mA and back to 0 (between 0 and 3.5 mA, the step size is 0.1 mA and then the step size is increased to 0.5 mA, while between 3.0 and 0 mA, the step size is reduced to 0.1 mA).

III. THERMALLY DRIVEN MIT-IMT

A. Device resistance

The upper panel of Fig. 1(b) shows the electrical resistance R versus temperature T of the device, acquired with a bias current $I = 5$ μA. The large resistance change at the MIT, by 4 orders of magnitude, is indicative of a high-quality V_2O_3 thin film with few defects. Due to the first-order nature of the MIT-IMT, the $R(T)$ curve is hysteretic, with a MIT temperature T_{MIT} about 5 K below the IMT temperature T_{IMT}. Consequently, for the IVC measurements and imaging presented below, it is vital to prepare a well-defined initial state in order to obtain reproducible results. This is achieved by thermal cycling, i.e., by cooling or by heating to temperatures at which the V_2O_3 is in a pure insulating or metallic state, before heating or cooling to the targeted temperature.

B. Phase separation at the MIT-IMT

We acquire a temperature series of wide-field microscopy images during one thermal cycle with a 1-K step size across the MIT-IMT. Figure 1(c) shows a selection of images from this series. An extended photomicrograph series is included in Appendix A1 (Fig. 5). Capital letters indicate the corresponding temperatures in the $R(T)$ curve [Fig. 1(b), upper panel]. By averaging over the area of interest, we obtain the temperature dependence of the reflectivity of the V_2O_3 film, normalized to the reflectivity of the Au electrodes [see Fig. 1(b), lower panel]. The hysteresis in the $R(T)$ curve is well reproduced by the normalized reflectivity versus T. The photomicrographs acquired in the hysteretic temperature regime show spontaneous insulator-metal phase separation with herringbone domains [50]. Domain patterns bearing a strong resemblance to those observed here can be found by numerical approximations to the Cahn-Larché equation,

which describes the phase separation of a binary mixture in the presence of elastic stress (see Fig. 6 in Ref. [60]). A fast-Fourier-transform (FFT) analysis of the domain pattern is included in Appendix A2 (Fig. 6). The FFT analysis reveals that the domains have two preferred directions; one is at an angle $\alpha \approx 9°$ at the MIT, which switches to $\alpha \approx 22°$ at the IMT, and the second is at $\alpha \approx 79°$, at both the MIT and the IMT. α is the angle between the y axis and the preferred direction [see the coordinates in Fig. 1(c)]. By comparing two optical images taken at the same temperature ($T = 168$ K) in the heating branch (IMT) for two consecutive thermal cycles (see Fig. 7 in Appendix A3), we find that the overall domain geometry (domain size and orientation) for repeated measurements is reproducible, as deduced from the FFT of the images. In real space, however, the domains may form in different locations in every heating cycle, despite a certain level of reproducibility. Interestingly, the heating and cooling cycles show significant differences in domain geometry. These results show that while there is some domain pinning, the local transition temperature depends strongly on cycle-dependent domain nucleation and growth, which changes the local strain distribution. This indicates that the phase separation is not due to growth-induced local inhomogeneities (in, e.g., chemical composition) of the thin film and that the domain configuration is plastic to a certain degree.
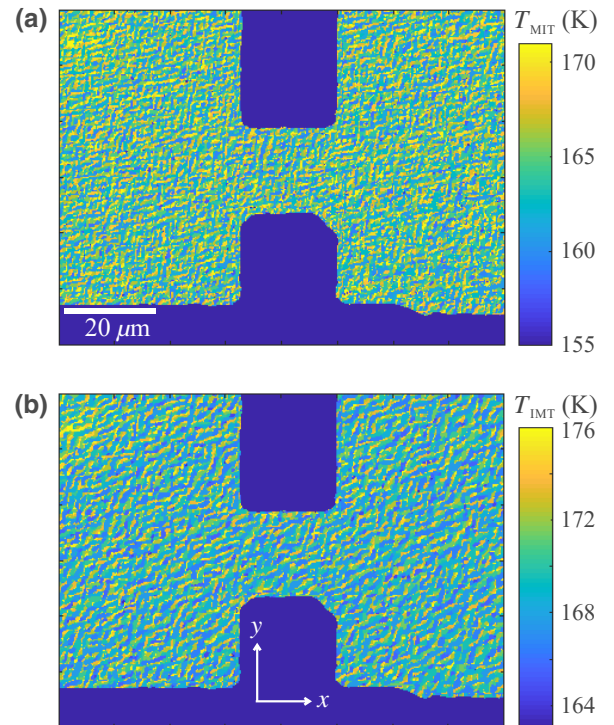

FIG. 2. The local transition temperatures of the V_2O_3 thin-film device: (a) T_{MIT} map; (b) T_{IMT} map. The large dark blue areas indicate Au electrodes.

In the lower panel of Fig. 1(b), we also include the reflectivity versus T curve for a single pixel, indicated by a red circle in the photomicrographs. The discontinuous steps in reflectivity at the MIT and IMT are indicative of a first-order phase transition [50].

C. Spatially resolved transition temperatures

By analyzing the steps in reflectivity for every pixel of the photomicrograph temperature series, maps of the local MIT and IMT temperatures T_{MIT} and T_{IMT}, respectively, with a resolution of 1 K can be derived (see Fig. 2). The maps of T_{MIT} [Fig. 2(a)] and T_{IMT} [Fig. 2(b)] show different patches with different transition temperatures, the shape and form of which resemble the herringbone domains in the photomicrographs. We note that the transition temperature maps shown in Fig. 2 constitute a single instance of the local MIT-IMT temperature variation, representing the strain-induced domain structure, but not an actual deterministic transition temperature map. These maps allow us, in the numerical analysis (discussed below), to consider how the strain-induced variation in local MIT-IMT temperatures affects the electrothermal breakdown.

IV. CURRENT-INDUCED IMT—RESISTIVE SWITCHING

In Fig. 3, we present electric transport data and simultaneously recorded photomicrographs for the current-induced IMT. We also include the results of numerical simulations for direct comparison. Note that we include an animation in Appendix C (Video 1) visualizing the resistive switching for every bias point.

A. Current-voltage characteristics

Before the measurement, the device is brought into the heating branch [at the base temperature $T_b = 158$ K; cf. Fig. 1(b)] via thermal cycling. Then IVCs are acquired for two consecutive current sweeps [see Fig. 3(a)]. During one sweep, the current increases from 0 mA to the maximum value of 20 mA and decreases back to 0 mA. The arrows in Fig. 3(a) indicate the sweep direction. Starting at the origin of the graph, the IVCs progress almost linearly up to $I \approx 0.5$ mA, which indicates an almost Ohmic resistance. Upon further increase of I, the slope of the IVCs increases significantly, i.e., the differential resistance decreases. A section with negative differential resistance follows. A horizontal jump indicative of an instantaneous (within the measurement time scale) reduction of the device resistance interrupts the IVCs at $I \approx 2.5$ mA. In other words, an electrical breakdown of the device causes resistive switching to a low-resistance state. After the jump, the IVCs progress almost vertically with a further increase of I. When the current is reduced from its maximum value, the IVCs progress almost vertically down to $I \approx 1.8$ mA, which is below the

value of the first horizontal jump. At this bias point, there is a second horizontal jump, indicative of an instantaneous increase of the device resistance, i.e., the device switches back to a high-resistance state. A section with a decreasing slope and a linear section follows.

The IVCs of the first and second sweeps are qualitatively similar. However, the maximum voltage, reached before the voltage jump appears in the upsweep, is reduced for the second sweep. For sweeps following the second sweep (not shown), the maximum voltage does not change any more and the IVCs are almost identical. Thermal cycling restores the IVC of the first sweep. We infer from the reproducibility of the IVC measurements that the observed resistive switching is nondestructive.

In addition to the very pronounced hysteresis in the low-bias-current regime where resistive switching occurs, we observe a small hysteresis in the high-bias regime; i.e., the downsweep branches have lower voltages than the upsweep branches [see the inset to Fig. 3(a)]. Furthermore, in this high-bias regime, the IVCs show small sawtoothlike jumps [see the inset to Fig. 3(a)].

B. Imaging filaments

Simultaneously with recording IVCs during a current sweep, photomicrographs are acquired. We present a selection of these photomicrographs in Fig. 3(b) (left-hand column) for the second current sweep. The animation in Appendix C (Video 1) shows a movie of the full current sweep.

The following remarks are crucial for interpreting the results. As deduced from the images acquired during the temperature sweeps, metallic and insulating domains have different optical reflectivities, allowing us to assign metallic and insulating resistivities to dark and bright regions of the device, respectively. From Fig. 1(c), we learn that dark areas in the photomicrograph indicate a metallic V_2O_3 phase, while the bright areas indicate an insulating phase.

Photomicrograph A in Fig. 3(b) is acquired at bias point A on the upsweep branch of the second current sweep, just before the large voltage jump appears. The photomicrographs acquired between zero bias and bias point A are all identical (see the animation in Video 1 of Appendix C). The V_2O_3 thin film between the electrodes is insulating (bright) with several small metallic (dark) inclusions and the device is in a high-resistance state. The metallic inclusions appear after the voltage jump of the first current sweep. Photomicrograph B corresponds to bias point B, immediately after the large voltage jump, indicating an abrupt switching of the device to a low-resistance state. A narrow metallic (dark) filament connects the electrodes at an oblique angle α, shunting the insulating film. With further increase of the current, the filament width increases (see photomicrographs B–D) by growing to the right. Bias point D is at $I = 20$ mA, which terminates the upsweep branch. When the current is reduced, the filament splits
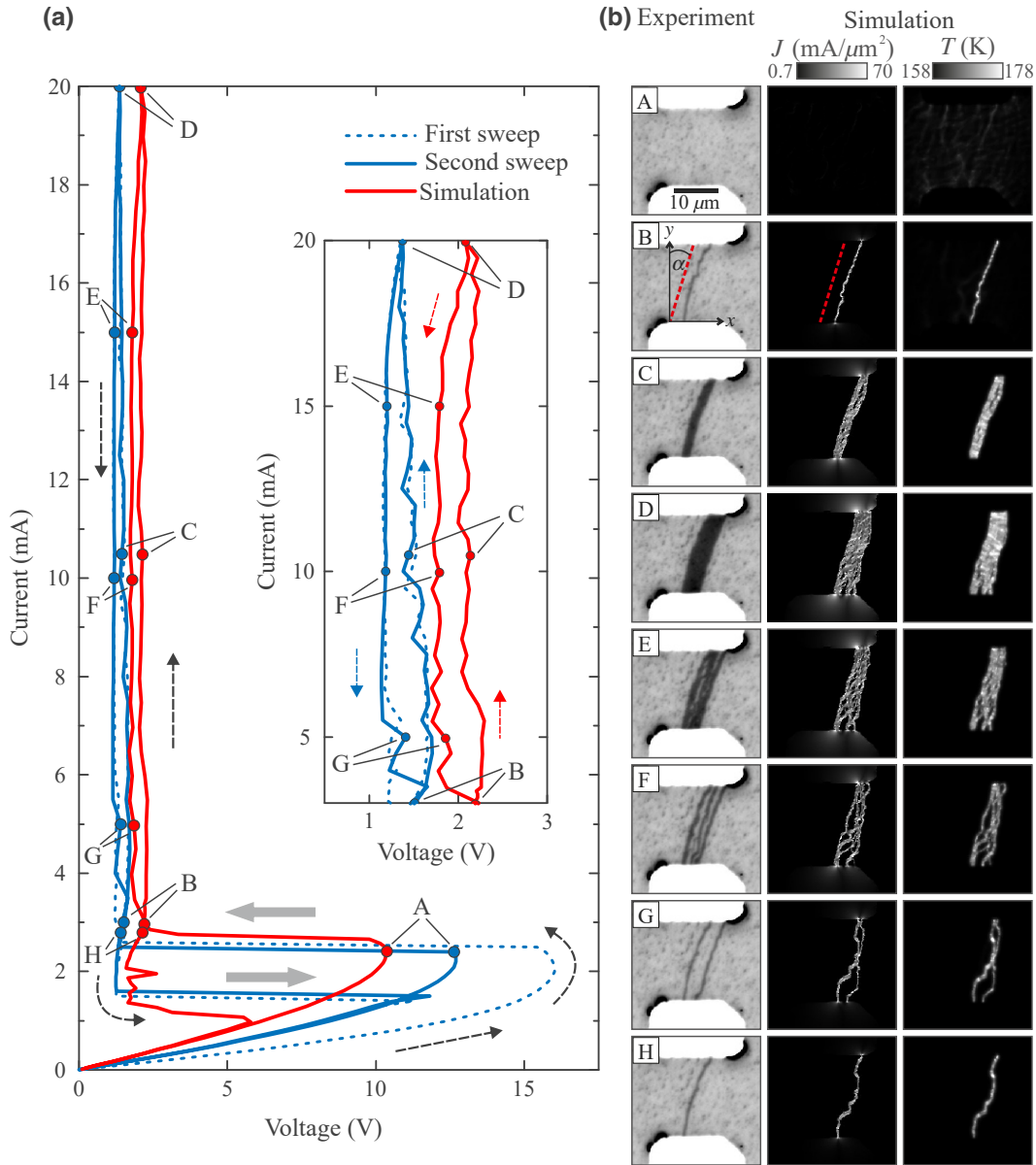
FIG. 3. The electrical breakdown in a planar V_2O_3 device at a base temperature $T_b = 158$ K at the onset of the IMT. (a) Measured (blue) and simulated (red) IVCs. The letters label data points for which images are shown in (b). The arrows indicate the sweep directions. The thick gray arrows indicate resistive switching to a low- and high-resistance state, respectively. The inset shows an enlargement of the high-current section. (b) The left-hand column shows a selection of the photomicrographs acquired during the second current sweep. The middle and right-hand columns show a selection of the simulated spatial distribution of the current density J and the local device temperature T, respectively. The dashed red lines for images B indicate an $\alpha \approx 17°$ inclination of the filament with respect to the y direction.

into several branches (photomicrograph E). When the current is reduced further, the splitting results in multiple parallel filaments (photomicrograph F). These filaments then disappear one after the other (photomicrographs F–H). Photomicrographs H and B are taken at almost the same current value and are almost identical. Finally, when the current is reduced to a bias point just below the second voltage jump, indicating an abrupt increase of the device

resistance, the last remaining filament disappears and the device returns to an insulating high-resistance state (see the animation in Video 1 of Appendix C).

C. Discussion of experimental results

We derive additional relations (Fig. 4) from the IVC and photomicrographs of the second current sweep, which
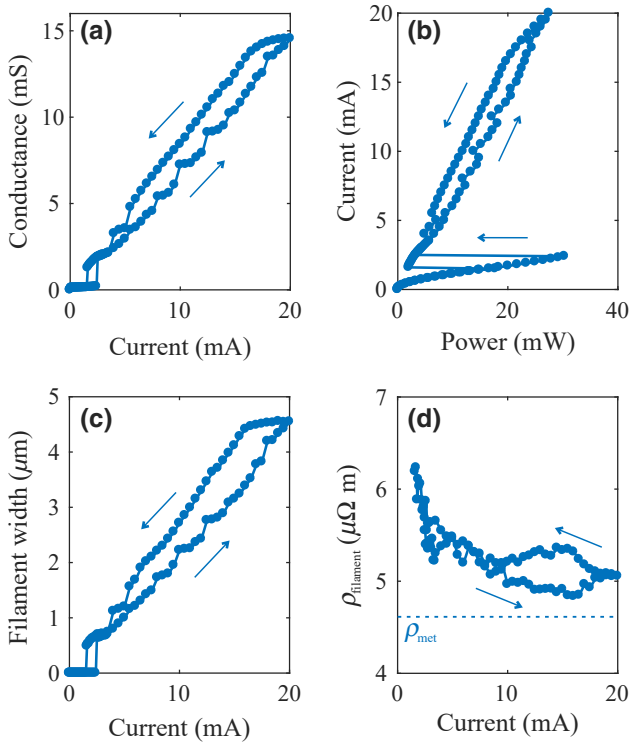
FIG. 4. The relations derived from the IVC and photomicrographs of the second current sweep in Fig. 3: (a) the conductance versus the current; (b) the current versus the power; (c) the estimated total filament width versus the current; (d) the resistivity of the metallic phase, estimated from the filament width, versus the current. The horizontal line indicates the resistivity of the metallic phase ρ_{met} used in the numerical simulations to obtain agreement with the experimentally measured resistance in the metallic phase.

help us to interpret the results. The derivation of the conductance ($G = I/V$) versus current and the current versus power ($P = I \times V$) relations [Figs. 4(a) and 4(b), respectively] is straightforward. In Fig. 4(c), the filament width is estimated by dividing the dark filament area in the photomicrographs by the filament length, which is estimated by approximating the filament as a straight line. The filament resistivity $\rho_{filament}$ is derived similarly, assuming that the filament extends throughout the thickness of the V_2O_3 film.

Now, we revisit the IVCs and the photomicrographs shown in Fig. 3. The overall behavior of the device is characteristic of an electrothermal breakdown [41]. The increasing slope after the linear (Ohmic) section in the low-bias-current regime, before switching to the high-resistance state, can be explained by a decrease of the device resistance due to Joule heating. According to the $R(T)$ curve shown in Fig. 1(b), close to the IMT an increase in the device temperature results in a considerable decrease in the device resistance. This effect produces the observed

back bending of the IVC. The system then becomes electrothermally unstable and the horizontal jump is the result of the formation of an electrothermal filament. Image B of Fig. 3(b) clearly shows the appearance of this metallic filament. The vertical progression of the IVC with increasing I after switching to the low-resistance state is associated with an increase in the filament width [see Fig. 3(b), images B–D]. The second horizontal jump during the return current sweep indicates an abrupt increase of the device resistance associated with the disappearance of the conducting filament (see the animation in Video 1 of Appendix C).

From Fig. 4(b), we learn that resistive switching occurs at maximum power. Considering the IVC of the second sweep [Fig. 3(a)], there is a slight back bending before the jump, indicating resistive switching. In the IVC of the first sweep, this back bending is more pronounced. If resistive switching were purely electric driven, the resistive switching would occur at maximum voltage, which is not the case. This is further evidence for an electrothermal breakdown. According to Fig. 4, in the high-bias regime after resistive switching, the device conductance, power, and filament width have an overall linear current dependence, while the filament resistivity is almost constant. Again, these dependencies are characteristic of an electrothermal breakdown, where the device current flows in a metallic filament and the current controls the width of this filament via Joule heating. Figure 4(d) shows good agreement of the filament resistivity with the resistivity of the metallic phase ρ_{met} used for numerical simulations (see Sec. IV D). We note that the initial steep decrease of $\rho_{filament}$ versus I in Fig. 4(d) might be due to the possibility that right after its formation (or before its extinction), the filament does not yet expand throughout the entire film thickness and/or that the filament width is below the spatial resolution of the microscope. In both cases, we would slightly overestimate $\rho_{filament}$. However, we also note that the independently determined conductance versus current [Fig. 4(a); from IVCs] and filament width versus current [Fig. 4(c); from images] curves match very closely, including the jumps at distinct current values. This indicates that the minimum filament width is very likely not much smaller than what we observe by imaging. Moreover, this again clearly demonstrates how the overall device resistance in the low-resistance state is governed by the optically detected filamentary structures.

We observe atypical effects, which can only be explained by features that are not included in the most simple electrothermal model. First, the filament is not straight along the y axis but, rather, connects the electrodes at an oblique angle α of approximately $17°$ with respect to the y direction [see image B in Fig. 3(b)]. In a homogeneous medium, one would expect that the shortest possible current path is preferred and the filament should follow the y direction. Second, during the downsweep, the filament first

splits into several branches and then it divides into multiple parallel filaments [see images E and F in Fig. 3(b)]. Because adjacent regions in the film are thermally coupled in the lateral direction, for a homogeneous medium one would expect that, as current decreases, the filament shrinks from its sides, since the filament temperature is highest in its center, so that the colder sides will transition into the insulating state more readily. Third, for high bias currents in the low-resistance state, there is hysteresis in the IVC [see the inset to Fig. 3(a)] and in the conductance, power, and filament width versus current relations (Fig. 4). However, after an electrothermal breakdown in a homogeneous medium without thermal hysteresis, the current should control these parameters without hysteresis in the IVC.

D. Numerical model

We develop a numerical model to investigate whether the electrical breakdown is electrothermal and whether the phenomena that are atypical for an electrothermal breakdown in a homogeneous medium without thermal hysteresis result from the strain-induced spatial variation of the MIT-IMT temperatures (see Fig. 2). A detailed description, based on Ref. [61], is given in Appendix B.

The numerical model is based on a 2D resistor network (see Fig. 8 of Appendix B1), for which the current distribution is solved via mesh-current analysis, while the thermal properties are modeled with a finite-difference approximation of the time-dependent heat equation. The heat conduction is incorporated using the backward Euler method. Latent heat is included. We account for the thermal coupling to the cryostat cold plate.

The four (or three) resistors of every cell in the 2D network have an individual hysteretic $R(T)$ dependence with the MIT-IMT temperatures corresponding to the experimentally determined values of Fig. 2. Deep in the insulating state, we assume the same resistivity $\rho_{\mathrm{ins}}(T)$ for all cells, which is determined from the measured $R(T)$ curve and, in the metallic state, we assume a constant $\rho_{\mathrm{met}} = 4.6 \ \mu\Omega$ m for all cells, also determined from the measured $R(T)$ curve [Fig. 1(b)]. With this approach, the strain-induced variation of the MIT-IMT temperatures is included in the model. For a detailed description, see Appendix B2.

Prior to the simulation of an entire current-sweep sequence, for each pixel the high- or low-resistance state within the hysteretic T range is set, depending on the history. This procedure takes into account, e.g., previous current-sweep sequences and hence can capture history effects in simulations for different current sweeps. For a given bias current value, the mesh-current analysis and the time-dependent heat equation are solved with small time steps until the solution reaches a steady state. Subsequently, the procedure is repeated with an incremented

current value. In this way, we calculate the IVC and the spatial distribution of the current density J and the temperature T.

E. Comparison of simulations with experimental results

The simulation results are included in Fig. 3 for direct comparison with the experimental data. The model is numerically stable over almost the whole parameter space, except for a section in the first current sweep after the resistive switching. For this reason, we focus our discussion on the second sweep. We note that the simulation of the first sweep reveals that after return to zero current, some resistors remain in the metallic state. This is consistent with the imaging results, which show that metallic inclusions appear after the first sweep. For the simulation of the second sweep, this information from the simulation of the first sweep is included, which explains why we also find different results in the simulations of different sweeps.

The heuristic numerical model, which includes strain effects in the V_2O_3 thin film indirectly via the MIT-IMT temperature maps, reproduces the resistive switching very well. Comparing the simulated IVC with the measured IVC in Fig. 3(a), the threshold currents for resistive switching are very similar and the maximum voltage in the simulation is only 14% smaller than in the experiment. The model reproduces the appearance and disappearance of the metallic filament accompanying resistive switching [see Fig. 3(b) and the animation in Video 1 of Appendix C]. Additionally, the effects, which are atypical for an electrothermal breakdown (discussed above), are also reproduced.

The agreement of the electrothermal model with the experimental results supports the hypothesis that an electrothermal breakdown induces resistive switching. The simulated images for bias points A and B in Fig. 3(b) demonstrate the current and temperature redistribution. As discussed in Sec. I, this redistribution results from a runaway effect driven by electrothermal instability. In particular, the simulation for bias point A already shows an inhomogeneous T distribution within the entire device area prior to resistive switching. After switching to the low-resistance state at bias point B, a single metallic filament appears in the optical image and the simulation shows that the current density is concentrated in this filament, with a local temperature of approximately 20 K above the base temperature T_b, while the area outside the filament cools down. At bias point B, the simulation still shows a few filamentary regions with slightly enhanced temperature, while with further sweeping up the bias current, these areas also cool down close to T_b.

Remarkably, the simulated data do not only reproduce all the experimentally observed features in the IVCs but also in the shape and direction of the metallic filament.

The filaments in the photomicrographs and the simulation both connect the electrodes at an oblique angle of $\alpha \approx 17°$, following roughly one preferred axis of the herringbone domains [see Fig. 1(c)]. The minimum filament width, right before the device switches back to the high-resistance state, is approximately 0.5 μm, which corresponds to the domain size. However, we note that the value of 0.5 μm has to be considered as an upper limit, as this is also the spatial resolution of the optical microscope. These observations support the idea that the herringbone domain structure significantly affects the details of resistive switching.

The effects that are atypical of an electrothermal breakdown, such as hysteresis and sawtoothlike jumps in the IVC, filament branching, and splitting, seem to have the same cause: a hysteretic and strain-induced heterogenous electrothermal medium.

Considering the overall shape of the IVCs shown in Fig. 3, the voltage is almost constant in the low-resistance state. This behavior is typical for an electrothermal breakdown, where a Joule-heating filament controls the voltage across the device. Usually, the filament growth with applied current is reversible and the increasing and decreasing current curves are congruent in this bias regime. However, the IVCs are hysteretic [see the inset to Fig. 3(a)]. We argue that the hysteresis in the thermally driven MIT-IMT, i.e., the shift between the MIT and IMT temperatures in V_2O_3, is causing this hysteresis in the IVCs. When the device is biased on the increasing current branch, the width of the filament increases and more and more regions undergo an IMT. For electrical bias on the decreasing current branch, the situation reverses, i.e., the width of the filament reduces and more and more regions undergo a MIT. As $T_{IMT} > T_{MIT}$, more Joule-heating power is required to drive regions through the IMT on the increasing current branch than on the decreasing current branch, when regions are driven through the MIT. Hence, for a given current I, the voltage V is higher in the increasing current branch than in the decreasing current branch.

The sawtoothlike IVC jumps [see the inset to Fig. 3(a)] are due to discontinuous generation and extinction of entire filaments or segments of filaments. We attribute this to filament edge pinning of boundaries between the insulating and metallic phase due to the spatial variation in local IMT temperatures. In particular, the filament does not grow continuously as the current is increased but switches adjacent domains to the metallic state as soon as the dissipated power is sufficient. For increasing currents, only a single filament is visible in the photomicrographs, the width of which increases for increasing currents. For decreasing currents, the expected behavior is that the filament width will decrease continuously. However, the filament branches and splits into multiple filaments (see Fig. 3 and the animation in Video 1 of Appendix C). The varying

local MIT-IMT temperatures (see Fig. 2) define percolation paths to which the filaments can lock in. Consequently, when the current is reduced, it distributes along these percolation paths. The geometry of these paths closely resembles the spontaneously forming domain configuration observed during temperature sweeps in the phase coexistence regime at the MIT. For the same reason, the filament is not connecting the electrodes along the shortest path but at an oblique angle. In contrast to the filament in the photomicrographs, the filament in the simulation consists of multiple filaments for biasing on the increasing current branch, although it is more compact than for the decreasing current branch. One explanation is that we cannot resolve these multiple filaments in the photomicrographs due to the limited resolution of the microscope. Another explanation is that the simulation uses transition-temperature maps derived from a series of fixed domain patterns, while in reality the domains are plastic (see the discussion in Sec. III B and Fig. 7 in Appendix A3), i.e., the domain walls can move. Due to this plasticity, there might be a tendency of the domains to merge, which is not reflected in the numerical model.

V. CONCLUSIONS

We demonstrate electrothermally induced resistive switching in a current-biased planar V_2O_3 thin-film device with a base temperature at the onset of the IMT. Photomicrographs show the appearance of a metallic filament that accompanies resistive switching. A model of the resistive switching reveals that the spatial variation in local MIT-IMT temperatures influences the details of the electrothermal breakdown.

The variation of the local MIT-IMT temperatures is the result of strain minimization in the V_2O_3 thin film and we conclude that elastic energy influences resistive-switching properties by affecting the filament configuration. Therefore, the influence of strain on the dynamics of switching devices should be taken into account and may allow for novel ways of tuning their properties.

These findings demonstrate the crucial role played by Joule heating and strain effects in this class of memristive devices, which are considered as promising building blocks in neuromorphic computing. Obviously, the approach taken in this work can also be applied to other Mott-insulator systems.

APPENDIX A: PHASE SEPARATION AT THE MIT-IMT

This appendix provides further details on the phase separation of the investigated V_2O_3 film across the MIT and the IMT.

1. Evolution of domain configurations across the MIT-IMT

Figure 5(b) shows a more detailed series of photomicrographs at temperatures T across the MIT-IMT. The $R(T)$ curves [Fig. 5(a)] are acquired with a bias current $I = 5\ \mu$A. The capital letters indicate the acquisition temperatures of the photomicrograph series. The $R(T)$ curves show a 4-order-of-magnitude change of R across the MIT-IMT, with a thermal hysteresis of approximately 5 K between the cooling and heating branches. The minimum temperature within the thermal cycle is 80 K.

The transition between the two phases progresses through the formation of domain patterns with dark and bright contrast that are identified as metallic and insulating regions, respectively. Starting from a homogeneous metallic state (A: 176 K), small insulating islands begin to form (B: 170 K) that grow and connect to form a herringbonelike domain pattern (C: 168 K and D: 166 K). At this point, the metallic domains still provide continuous paths connecting the electrodes. These get disconnected when the temperature is further decreased (E: 164 K and F: 162 K), which goes along with a steep increase in resistance, as the current now has to flow through parts of the film that are in the insulating phase. At even lower temperatures (G: 161 K, H: 160 K, and I: 158 K), the V_2O_3 film is in a state where metallic patches are embedded within an insulating matrix. The size of the metallic domains decreases with decreasing temperature until the sample is in an almost homogeneous insulating state (J: 152 K).

The heating branch shows a slightly different behavior. Beginning from the insulating state (K: 160 K), small metallic islands appear (L: 164 K and M: 166 K) that connect to elongated domains (N: 167 K and O: 168 K). These domains are wider than the domains in the cooling branch and have a different preferred direction. Upon further increase of the temperature, more metallic domains appear and long metallic paths are created that eventually form continuous metallic paths that connect the electrodes (P: 170 K). The metallic regions grow (Q: 172 K and R: 174 K) until only isolated insulating patches are left
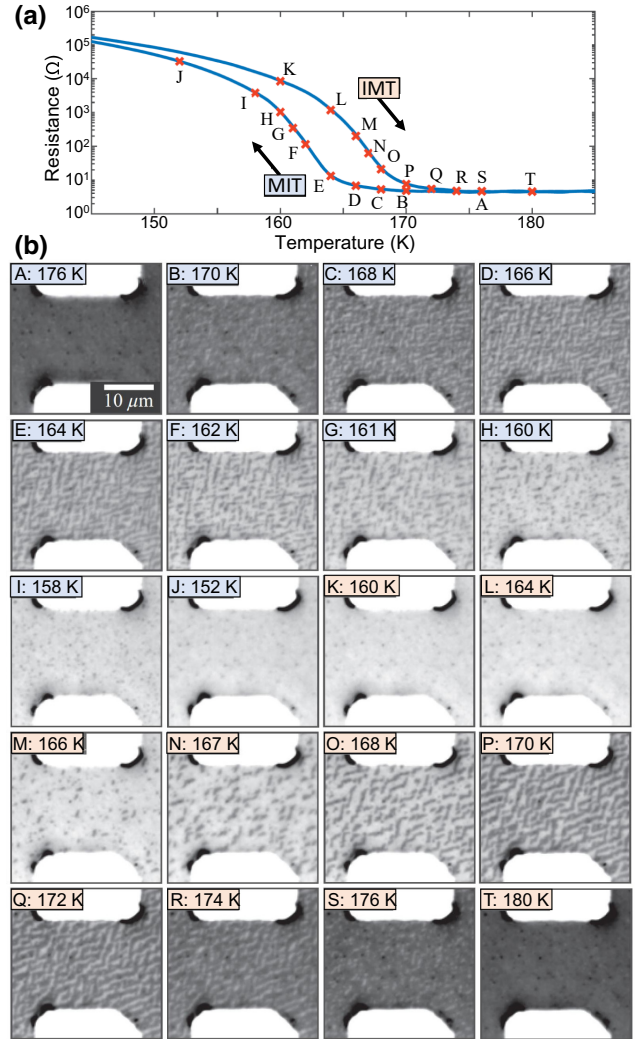

FIG. 5.   The phase separation in V_2O_3 at the MIT-IMT: (a) $R(T)$ curves; (b) images acquired at the points, labeled A–T in (a), during cool-down and warm-up of the sample.

(S: 176 K). Eventually, the film arrives in a homogeneous metallic state (T: 180 K).

2. Directionality and periodicity of the domain patterns

The preferred direction of the domains and their periodicity can be estimated from the FFT) of the optical images. This is shown for selected temperatures in Fig. 6. Angles are measured clockwise with respect to the vertical axis, i.e., they correspond to the definition of α for optical images in the main text. The FFT of the domain configuration in the MIT [Figs. 6(a) and 6(b)] clearly shows four peaks that correspond to directions of $99°$ and $169°$, with a mean periodicity of 1.3 μm at 166 K and 1.5 μm at 162 K. The preferred orientations of the long axis of the domains
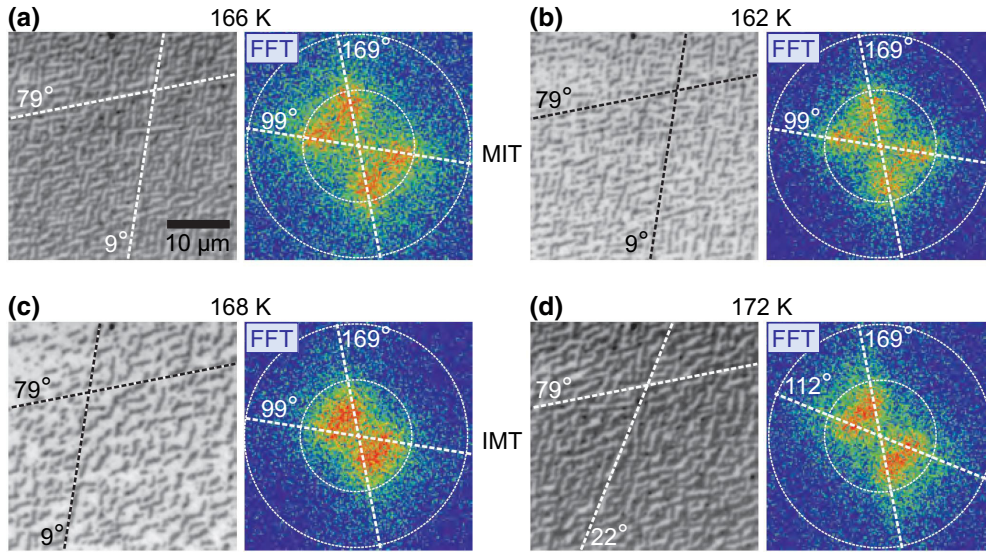
FIG. 6. The domain configuration (left) and FFT (right) for selected temperatures of (a) 166 K and (b) 162 K in the cooling branch (MIT) and (c) 168 K and (d) 172 K in the heating branch (IMT). The dashed lines highlight the predominant directionality of the long axis of domains in the real-space images and in which the peaks occur. The angles are measured clockwise with respect to the vertical axis. The inner (outer) circles in the FFT correspond to a spatial frequency of $1/\mu$m ($2/\mu$m).

in real space are perpendicular to the directions found in the FFT and are indicated by the broken lines at 9° and 79° in the optical images. Figures 6(c) and 6(d) show the domain configuration and FFT for temperatures of 168 K and 172 K in the IMT. At $T = 168$ K, it is not possible to distinguish the peaks of the 99° and 169° axes in the FFT. However, the real-space image at 168 K shows that many of the domains are still oriented along the 9° and 79° axes, while some domains have an orientation that lies in between these axes. At 172 K, on the other hand, only a few domains are oriented along the 9° axis and the preferred directions become 22° and 79°, which is observed in the FFT as a narrowing of the peaks in the angular direction. The mean periodicity of the domains in the heating branch (IMT) is found to be 2.2 μm at 168 K and 1.8 μm at 172 K.

3. Reproducibility of the domain configuration

Figures 7(a) and 7(b) show the domain configuration at 168 K in the heating branch for two subsequent measurement runs. A complete thermal cycle (heating to room temperature and cooling to 80 K) separates the two images. While the overall density of metallic domains is similar, the domain patterns differ significantly. For comparison, a color-coded superposition of the images in Figs. 7(a) and 7(b) is shown in Fig. 7(c). Metallic domains that are present in both Figs. 7(a) and 7(b) appear dark. Domains that are present only in Fig. 7(a) are represented in green, while those that are present only in Fig. 7(b) are

represented in red. It is apparent that the domain configuration for repeated measurements is neither deterministic nor random. The same holds true for other temperatures in both the MIT and IMT. This indicates that the phase separation is not due to growth-induced local inhomogeneities of the film—e.g., in chemical composition—which could lead to a spatially varying transition temperature but, rather, is caused through minimization of local strain, as proposed by McLeod *et al.* [50].

APPENDIX B: NUMERICAL MODEL

This appendix describes the numerical model, which is used to simulate the IVCs and spatial distribution of temperature T and current density J in the V_2O_3 films. This description is based on chapter 5.4 in Ref. [61].

1. Resistor network and mesh-current analysis

To calculate the current distribution, the sample is approximated by a 2D resistor network that is constructed from a square primitive cell with edge length $\Delta x = \Delta y$ that contains one node and four resistors. The resulting resistor network, obtained by assembling n primitive cells in the x direction and m primitive cells in the y direction, is shown in Fig. 8. The four resistors within each primitive cell with index i,j, with $i \in \{1,m\}$ and $j \in \{1,n\}$, are assigned the same resistance $R_{i,j}$. The resistors at the left and right edges of the resistor network are truncated, making the boundary insulating, and a perfectly conducting wire connects the bottom and top edges to the current
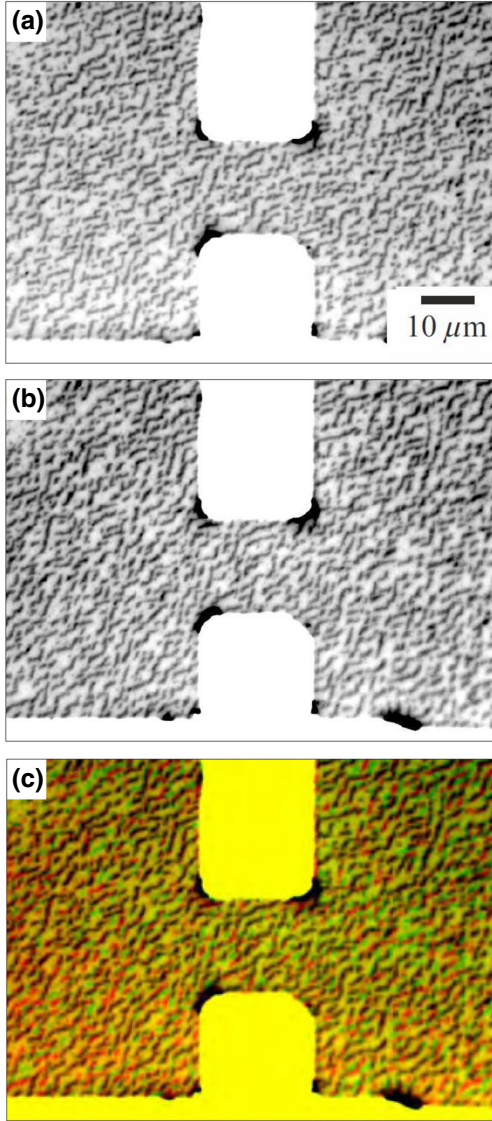
FIG. 7. The reproducibility of the domain configuration. (a),(b) Optical images, recorded at 168 K in the heating branch for two subsequent runs with a full thermal cycle in between. (c) The color-coded superposition of images from (a) and (b). Metallic domains that are present in both (a) and (b) appear dark. Metallic domains only present in (a) are green, while those only present in (b) are red. Insulating domains present in both micrographs are shown in yellow.

FIG. 8. The resistor network of $m \times n$ primitive cells used to approximate the resistance of the sample. Each primitive cell (red squares) contains one node and four resistors (except for the columns $j = 1$ and $j = n$, with only three resistors per primitive cell). A mesh current $I_{k,l}$ (blue) flows in each of the essential meshes of the resistor network. An additional mesh containing the current source is connected to the left-hand side of the resistor network.

can be written in matrix form as

$$
\mathbf{W} \cdot \begin{pmatrix} I_{11} \\ \vdots \\ I_{1,n-1} \\ \vdots \\ I_{m+1,n-1} \\ I \end{pmatrix} = \begin{pmatrix} 0 \\ \vdots \\ 0 \\ \vdots \\ 0 \\ V \end{pmatrix}. \tag{B1}
$$

The solution of this equation system returns, for a given bias current I, the voltage V across the network and the mesh currents, from which the current through each of the four resistors in the primitive cell i,j can be calculated according to

$$
\begin{aligned}
I_{i,j,1} &= I_{k,l} - I_{k,l-1}, \\
I_{i,j,2} &= I_{k+1,l} - I_{k,l}, \\
I_{i,j,3} &= I_{k+1,l} - I_{k+1,l-1}, \\
I_{i,j,4} &= I_{k+1,l-1} - I_{k,l-1}, \tag{B2}
\end{aligned}
$$

where, by convention, currents flowing in the positive x and y directions have positive sign. These describe the current flow between adjacent primitive cells and are defined on the boundary between them (cf. Fig. 9).

Although it is not properly defined, it is desirable to evaluate the current density at the nodes. This is calculated by interpolating the current densities at the boundaries of the primitive cell, which delivers the current densities $J_{i,j}^x$

source. The loops formed by four neighboring nodes and the resistors between them are called essential meshes.

For the complete resistor network, one obtains a set of $a = (n-1)(m+1)$ equations for a essential meshes plus the equation for the current source mesh, which serves as a boundary condition. This set of equations is assembled into a $(a+1) \times (a+1)$ matrix $\mathbf{W}$, so that the equation system
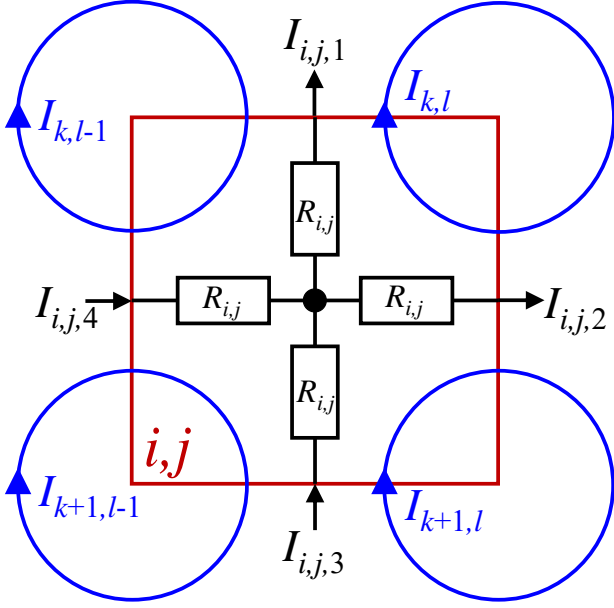
FIG. 9. On the definition of the currents $I_{i,j,1}$ to $I_{i,j,4}$ flowing through the resistors in the primitive cell i,j, which are calculated from the adjacent mesh currents.

in the x direction and $J_{i,j}^{y}$ in the y direction, as well as the magnitude of the current density $J_{i,j}^{\mathrm{norm}}$:

$$J_{i,j}^{x} = \frac{I_{i,j,2} + I_{i,j,4}}{2\,\Delta y\,d_f},$$

$$J_{i,j}^{y} = \frac{I_{i,j,1} + I_{i,j,3}}{2\,\Delta x\,d_f},$$

$$J_{i,j}^{\mathrm{norm}} = \sqrt{\left(J_{i,j}^{x}\right)^2 + \left(J_{i,j}^{y}\right)^2}, \qquad (B3)$$

with the film thickness d_f. Note that these quantities approach the correct value only for Δx, $\Delta y \to 0$ and might deviate from the correct solution for finite dimensions of the primitive cell. Therefore, they are only used for displaying the results and not as input for further calculations. The power density $p_{i,j}$ generated through Joule heating in the primitive cell of volume $V_{i,j}$ is a quantity that is used for modeling the thermal characteristics of the sample and is given by

$$p_{i,j} = \frac{P_{i,j}}{V_{i,j}} = \frac{R_{ij}}{\Delta x\,\Delta y\,d_f}\left(I_{i,j,1}^2 + I_{i,j,2}^2 + I_{i,j,3}^2 + I_{i,j,4}^2\right). \qquad (B4)$$

For the reasons mentioned above, the currents through the boundaries are used to calculate the power dissipated in the resistors within the primitive cell.

2. Definition of temperature-dependent resistivity

To approximate the temperature dependence of the resistivity of the V_2O_3 film, the following assumptions are made. (i) The resistivity ρ_{met} in the metallic phase is constant with respect to temperature and lateral position. (ii) The resistivity ρ_{ins} deep in the insulating phase (at temperatures far below the MIT-IMT temperatures) is homogeneous and has the same temperature dependence as the globally measured $R(T)$. (iii) For cool-down of the sample, the increase in resistivity from ρ_{met} to ρ_{ins} in the transition region is described by a function $f\ (T_{\mathrm{MIT}}\,(x,y) - T)$ that increases from 0 above the MIT temperature T_{MIT} to 1 at low temperatures. Accordingly, the local resistivity for cool-down of the sample is described by the function

$$\rho_{\mathrm{MIT}}\,(x,y,T) = \rho_{\mathrm{ins}}\,(T)\,f\,[T_{\mathrm{MIT}}\,(x,y) - T] + \rho_{\mathrm{met}}. \quad (B5)$$

(iv) Similarly, for warm-up of the sample, the decrease in resistivity in the transition region is described by the same function $f\,[T_{\mathrm{IMT}}\,(x,y) - T]$, which now has the difference between the IMT temperature T_{IMT} and the temperature as argument:

$$\rho_{\mathrm{IMT}}\,(x,y,T) = \rho_{\mathrm{ins}}\,(T)\,f\,[T_{\mathrm{IMT}}\,(x,y) - T] + \rho_{\mathrm{met}}. \quad (B6)$$

Since the transition temperatures vary spatially, this leads to an inhomogeneous distribution of the resistivity in the transition region, while the resistivity is homogeneous outside the transition region. Note that the transition temperatures $T_{\mathrm{MIT}}\,(x,y)$ and $T_{\mathrm{IMT}}\,(x,y)$ that are used here to define the temperature dependence of the resistivity are determined experimentally (cf. Fig. 2), which should allow for a good representation of the spatial dependence of the resistivity.

The resistivity in the metallic phase is derived from experimental data as $\rho_{\mathrm{met}} = 4.618 \times 10^{-6}$ Ωm. The resistivity at low temperatures is obtained by fitting the measured $R(T)$ curve in the temperature range from 80 K to 130 K with the function

$$\rho_{\mathrm{ins}}\,(T) = ae^{bT} + ce^{dT}, \qquad (B7)$$

where $a = 4.66 \times 10^8$ Ωm, $b = -0.1926$/K, $c = 3.19 \times 10^5$ Ωm, and $d = -0.098\,49$ /K. The function f that describes the transition between the metallic and insulating phases is obtained by running the mesh-current analysis with the matrix $R_{i,j}\,(T)$ as input for temperatures throughout the transition region and adjusting f until the measured resistance is reproduced. The resulting temperature-dependent resistivity is shown in Fig. 10.
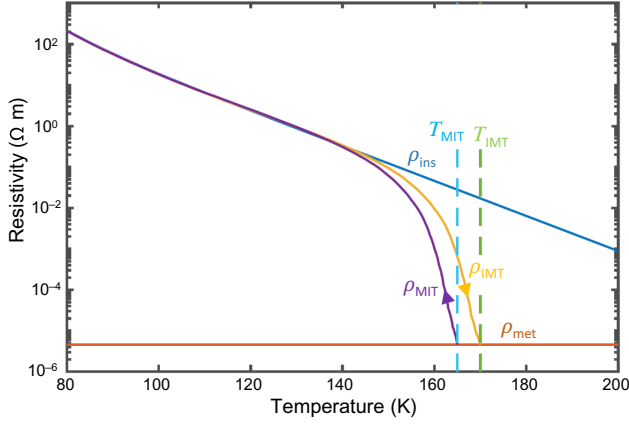
FIG. 10. The modeling of the temperature dependence of the V_2O_3 resistivity. For the cooling branch, ρ_{MIT} increases from ρ_{met} to ρ_{ins} for $T < T_{MIT}$ (blue dashed line). In the heating branch ρ_{IMT} decreases to ρ_{met} for T approaching T_{IMT} (green dashed line).

3. Finite-difference approximation to heat equation

Heat transfer in solids is described by the parabolic partial differential equation, known as the heat equation:

$$\rho\,c_P\frac{\partial T}{\partial t} - \nabla\,(k\nabla T) = \dot{q}_V, \tag{B8}$$

where ρ is the density, c_P is the heat capacity at constant pressure, k is the thermal conductivity, and $\dot{q}_V$ is the volumetric heat source. In two dimensions and for a film thickness d_f, this can be written as

$$\rho\,c_P\frac{\partial T}{\partial t} - \frac{\partial}{\partial x}\left(k_x\frac{\partial T}{\partial x}\right) - \frac{\partial}{\partial y}\left(k_y\frac{\partial T}{\partial y}\right) = \dot{q}_V, \tag{B9}$$

or, if the thermal conductivity $k = k_x = k_y$ is isotropic, as

$$\frac{\partial T}{\partial t} - \kappa\left(\frac{\partial^2 T}{\partial x^2} + \frac{\partial^2 T}{\partial y^2}\right) = \frac{\dot{q}_V}{\rho c_P}, \tag{B10}$$

where the thermal diffusivity $\kappa = k/(\rho c_P)$. The partial derivatives in the heat equation can be approximated by finite differences. The same discretization in space as for the mesh-current analysis is used and the variables are evaluated on the central node of the primitive cell with index i,j. The time is discretized into time steps Δt and an index τ is introduced describing the point in time. The heat equation can be approximated in space and time using a number of finite-difference methods. Here, the backward Euler method is used which, in contrast to the forward Euler or Crank-Nicolson method, is unconditionally stable and immune to oscillations. For a node spacing of Δx and Δy and a time step Δt, the implicit discrete form of

Eq. (B10) is given by

$$\frac{T_{i,j}^{\tau+1} - T_{i,j}^{\tau}}{\Delta t} - \kappa\left[\frac{T_{i,j+1}^{\tau+1} - 2T_{i,j}^{\tau+1} + T_{i,j-1}^{\tau+1}}{(\Delta x)^2}\right.$$
$$\left. + \frac{T_{i+1,j}^{\tau+1} - 2T_{i,j}^{\tau+1} + T_{i-1,j}^{\tau+1}}{(\Delta y)^2}\right] = \frac{\dot{q}_{i,j}^{\tau}}{\rho\,c_P}. \tag{B11}$$

At this point, an additional thermal coupling to the bath with temperature T_b is introduced, which is a consequence of the heat flow to the cold finger through the substrate of thickness d_s and an effective thermal conductivity k_s. This can be modeled as a heat source $\dot{Q}_b = k_s\left(T_b - T_{i,j}^{\tau+1}\right)\Delta x\Delta y/d_s$ that is given by the power that is transferred to the bath through a cuboid with cross section $\Delta x\;\Delta y$ and length d_s. Accordingly, the volumetric heat source in Eq. (B11) is represented by the sum of Joule heating $p_{i,j}$ and a contribution of $\dot{Q}_b$ lumped to the volume $V_{i,j}$:

$$\dot{q}_{i,j}^{\tau} = p_{i,j}^{\tau} + \frac{\dot{Q}_b}{V_{i,j}} = p_{i,j}^{\tau} + \frac{k_s}{d_f\,d_s}\left(T_b - T_{i,j}^{\tau+1}\right). \tag{B12}$$

It is further assumed that the node spacing in the x and y directions is equal ($\Delta x = \Delta y$). With the thermal diffusivity to the bath $\kappa_s = k_s/\left(\rho_s\,c_{P,s}\right)$, Eq. (B11) becomes

$$T_{i,j}^{\tau+1} - T_{i,j}^{\tau} - \frac{\kappa\,\Delta t}{(\Delta x)^2}$$
$$\times \left(T_{i-1,j}^{\tau+1} + T_{i,j-1}^{\tau+1} - 4T_{i,j}^{\tau+1} + T_{i,j+1}^{\tau+1} + T_{i+1,j}^{\tau+1}\right)$$
$$= \frac{p_{i,j}^{\tau}\,\Delta t}{\rho\,c_P} + \frac{\kappa_s\,\Delta t}{d_f\,d_s}\left(T_b - T_{i,j}^{\tau+1}\right). \tag{B13}$$

Rearranging this equation so that terms at time $\tau + 1$ are on the left-hand side and terms at time τ are on the right-hand side, and introducing the coefficients $A_f = \kappa\,\Delta t/(\Delta x)^2$, $A_b = \kappa_s\,\Delta t/\left(d_f\;d_s\right)$, and $A_q = \Delta t/\left(\rho\,c_P\right)$, results in

$$-A_f\;T_{i-1,j}^{\tau+1} - A_f\;T_{i,j-1}^{\tau+1} + \left(1 + 4A_f + A_b\right)T_{i,j}^{\tau+1}$$
$$-A_f\;T_{i,j+1}^{\tau+1} - A_f\;T_{i+1,j}^{\tau+1} - A_bT_b = T_{i,j}^{\tau} + A_q p_{i,j}^{\tau}. \tag{B14}$$

These equations are assembled into a $(m \cdot n + 1) \times (m \cdot n + 1)$ heat transfer matrix $\mathbf{H}$ so that the equation system is given by

$$\mathbf{H} \cdot \begin{pmatrix} T_{11}^{\tau+1} \\ \vdots \\ T_{1n}^{\tau+1} \\ \vdots \\ T_{mn}^{\tau+1} \\ T_b \end{pmatrix} = \begin{pmatrix} T_{11}^{\tau} + A_q p_{1,1}^{\tau} \\ \vdots \\ T_{1n}^{\tau} + A_q p_{1,n}^{\tau} \\ \vdots \\ T_{mn}^{\tau} + A_q p_{m,n}^{\tau} \\ T_{\text{bath}} \end{pmatrix}, \tag{B15}$$
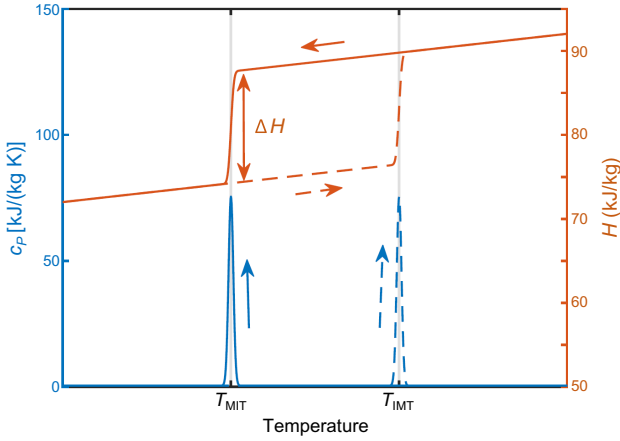
FIG. 11. The temperature-dependent heat capacity c_P (blue curve) and enthalpy H (red curve). The latent heat ΔH at the phase transition leads to a jump in enthalpy and a peak in heat capacity. The broken lines show the IMT at T_{IMT} and the solid lines the MIT at T_{MIT}.

where the last row contains the equation $T_b = T_{\mathrm{bath}}$, which is used to set the bath temperature as a boundary condition.

The metal-insulator phase transition in V_2O_3 is connected to the occurrence of a latent heat of approximately $\Delta H = 2$ kJ/mol ≈ 13.3 kJ/kg that has to be supplied to the system to change from one phase to the other [62]. The latent heat, which is represented by a jump in enthalpy H, leads to a diverging heat capacity $c_P = dH/dT$ at the phase transition [63]. The latent heat is represented in the numerical model by introducing a temperature-dependent heat capacity

$$c_P(T) = c_{P0} + \frac{\Delta H}{\sqrt{\pi}\,\Delta T} e^{\frac{(T-T_c)^2}{\Delta T^2}}, \qquad \text{(B16)}$$

where a constant heat capacity $c_{P0} = 0.45$ kJ/ (kg K) and a finite width $\Delta T = 0.1$ K of the phase transition around the transition temperature T_c is assumed. The heat capacity according to Eq. (B16) is shown in Fig. 11.

4. Simulation of electrical breakdown in V_2O_3

To simulate the electrical breakdown in V_2O_3, the equations for the current distribution and heat transfer [Eqs. (B1) and (B15), respectively] are implemented and solved in MATLAB. This is done by initializing the system at zero bias current ($I_{\mathrm{bias}} = 0$) and at the bath temperature ($T_{i,j} = T_{\mathrm{bath}}$) for $t = 0$ and slowly ramping the current to $I_{\mathrm{bias}}^{\mathrm{max}} = 20$ mA and back to $I_{\mathrm{bias}}^{\mathrm{end}} = 0$ mA over time, with a rate that is much slower than the thermal dynamics of the sample, so that the system is modeled in quasistatic approximation.

Figure 12 shows the program flow chart. First, the system is initialized at the bath temperature, zero bias current, and completely in the insulating phase. Then, the $R_{i,j}$ for
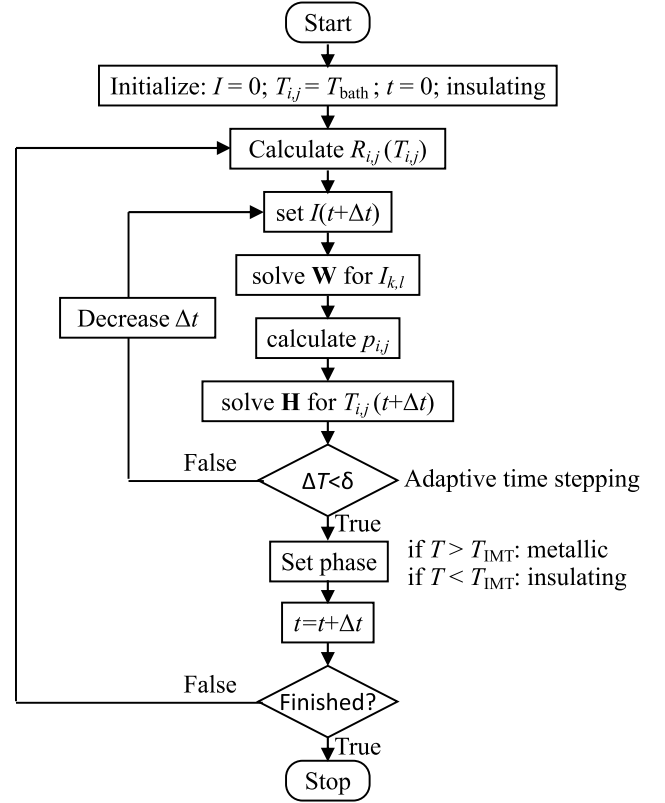

FIG. 12. The flow chart for the simulation.

the initial temperature and phase are calculated. The bias current is increased to the value at the next time step, $t + \Delta t$. The mesh-current analysis is solved and the current distribution is calculated. The Joule heating is calculated from $R_{i,j}$ and the current distribution and input into the heat equation, which is solved for the temperatures $T_{i,j}(t + \Delta t)$. Note that due to the strong temperature dependence of resistivity and heat capacity, the system is highly nonlinear as it approaches the MIT or IMT. To accurately capture the nonlinearities, a sufficiently small time step Δt needs to be used. This is accomplished by using an adaptive time step. If the maximum change in temperature,

$$\Delta T = \max_{\forall i,j} \left[|T_{i,j}(t + \Delta t) - T_{i,j}(t)| \right], \qquad \text{(B17)}$$

is larger than the convergence criterion δ, the time step is reduced and the temperature distribution is recalculated using the smaller time step. If ΔT is far below the convergence criterion, the time step is increased. When the convergence criterion is satisfied, the phase transition is evaluated: the material is set to the metallic phase, where T_{IMT} is exceeded and to the insulating phase, where the temperature has fallen below T_{MIT}. Subsequently, the time is incremented and the calculated temperature and phase
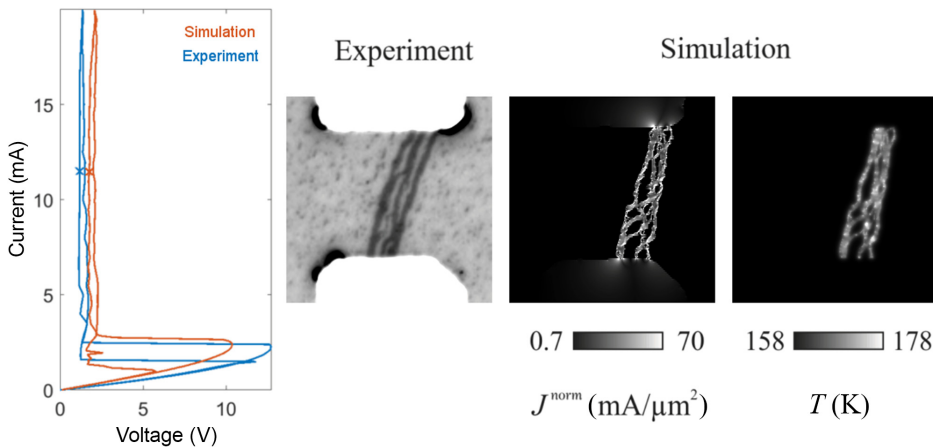
VIDEO 1. An animation of the electrical breakdown in a planar thin-film device at the onset of the IMT. The left-hand graph shows the current-voltage relation of the experiment and the simulation. The two small crosses ("×") mark the bias points. The panel in the center shows the corresponding photomicrographs of the device under investigation. The two panels on the right-hand side show the simulated current density and temperature.

distribution are used as inputs to calculate the new $R_{i,j}$ values. The program runs in a loop, progressing through time, until the bias current has reached its final value.

APPENDIX C: CURRENT-VOLTAGE RELATION, PHOTOMICROGRAPHS, AND COMPUTER-SIMULATION DATA COMBINED IN ONE ANIMATION

To summarize the main results on resistive switching due to electrothermal filament formation, we combine the electrical transport measurement data, the photomicrographs, and the computer-simulation data in one animation (see Video 1).

[1] P. Limelette, A. Georges, D. Jérome, P. Wzietek, P. Metcalf, and J. M. Honig, Universality and critical behavior at the Mott transition, Science **302**, 89 (2003).

[2] D. B. McWhan and J. P. Remeika, Metal-insulator transition in $(V_{1-x}Cr_x)_2O_3$, Phys. Rev. B **2**, 3734 (1970).

[3] M. Imada, A. Fujimori, and Y. Tokura, Metal-insulator transitions, Rev. Mod. Phys. **70**, 1039 (1998).

[4] A. Singer, J. G. Ramirez, I. Valmianski, D. Cela, N. Hua, R. Kukreja, J. Wingert, O. Kovalchuk, J. M. Glownia, M. Sikorski, M. Chollet, M. Holt, I. K. Schuller, and O. G. Shpyrko, Nonequilibrium Phase Precursors during a Photoexcited Insulator-to-Metal Transition in V_2O_3, Phys. Rev. Lett. **120**, 207601 (2018).

[5] Z. Yang, C. Ko, and S. Ramanathan, Oxide electronics utilizing ultrafast metal-insulator transitions, Annu. Rev. Mater. Res. **41**, 337 (2011).

[6] P. Markov, R. E. Marvel, H. J. Conley, K. J. Miller, R. F. Haglund Jr., and S. M. Weiss, Optically monitored electrical switching in VO_2, ACS Photonics **2**, 1175 (2015).

[7] N. A. Butakov, I. Valmianski, T. Lewi, C. Urban, Z. Ren, A. A. Mikhailovsky, S. D. Wilson, I. K. Schuller, and J. A. Schuller, Switchable plasmonic-dielectric resonators with metal-insulator transitions, ACS Photonics **5**, 371 (2018).

[8] J. del Valle, Y. Kalcheim, J. Trastoy, A. Charnukha, D. N. Basov, and I. K. Schuller, Electrically Induced Multiple Metal-Insulator Transitions in Oxide Nanodevices, Phys. Rev. Appl. **8**, 054041 (2017).

[9] E. Janod, J. Tranchant, B. Corraze, M. Querré, P. Stoliar, M. Rozenberg, T. Cren, D. Roditchev, V. T. Phuoc, M. Besland, and L. Cario, Resistive switching in Mott insulators and correlated systems, Adv. Funct. Mater. **25**, 6287 (2015).

[10] C.-Y. Lin, P.-H. Chen, T.-C. Chang, K.-C. Chang, S.-D. Zhang, T.-M. Tsai, C.-H. Pan, M.-C. Chen, Y.-T. Su, Y.-T. Tseng, Y.-F. Chang, Y.-C. Chen, H.-C. Huang, and S. M. Sze, Attaining resistive switching characteristics and selector properties by varying forming polarities in a single HfO_2-based RRAM device with a vanadium electrode, Nanoscale **9**, 8586 (2017).

[11] A. Sawa, Resistive switching in transition metal oxides, Mater. Today **11**, 28 (2008).

[12] H. S. P. Wong, H.-Y. Lee, S. Yu, Y.-S. Chen, Y. Wu, P.-S. Chen, B. Lee, F. T. Chen, and M.-J. Tsai, Metal-oxide RRAM, Proc. IEEE **100**, 1951 (2012).

[13] M. A. Zidan, J. P. Strachan, and W. D. Lu, The future of electronics based on memristive systems, Nat. Electron. **1**, 22 (2018).

[14] D. Ielmini and H. S. P. Wong, In-memory computing with resistive switching devices, Nat. Electron. **1**, 333 (2018).

[15] Z. Wang, H. Wu, G. W. Burr, C. S. Hwang, K. L. Wang, Q. Xia, and J. J. Yang, Resistive switching materials for information processing, Nat. Rev. Mater. **5**, 173 (2020).

[16] M. D. Pickett, G. Medeiros-Ribeiro, and R. S. Williams, A scalable neuristor built with Mott memristors, Nat. Mater. **12**, 114 (2013).

[17] I. K. Schuller, R. Stevens, R. Pino, and M. Pechan, Neuromorphic computing—from materials research to systems architecture roundtable, DOI:10.2172/1283147 (2015).

[18] P. Stoliar, J. Tranchant, B. Corraze, E. Janod, M. Besland, F. Tesler, M. Rozenberg, and L. Cario, A leaky-integrate-and-fire neuron analog realized with a Mott insulator, Adv. Funct. Mater. **27**, 1604740 (2017).

[19] W. Yi, K. Tsang, S. Lam, X. Bai, J. Crowell, and E. Flores, Biological plausibility and stochasticity in scalable VO_2 active memristor neurons, Nat. Commun. **9**, 4661 (2018).

[20] J. del Valle, P. Salev, F. Tesler, N. M. Vargas, Y. Kalcheim, P. Wang, J. Trastoy, M.-H. Lee, G. Kassabian, J. G. Ramírez, M. J. Rozenberg, and I. K. Schuller, Subthreshold firing in Mott nanodevices, Nature **569**, 388 (2019).

[21] Hai-Tian Zhang, Priyadarshini Panda, Jerome Lin, Yoav Kalcheim, Kai Wang, John Freeland, Dillon Fong, Shashank Priya, Ivan Schuller, Subramanian Sankaranarayanan, Kaushik Roy, and Shriram Ramanathan, Organismic materials for beyond von Neumann machines, Appl. Phys. Rev. **7**, 011309 (2020).

[22] Sangheon Oh, Yuhan Shi, Javier del Valle, Pavel Salev, Yichen Lu, Zhisheng Huang, Yoav Kalcheim, Ivan K. Schuller, and Duygu Kuzum, Energy-efficient Mott activation neuron for full-hardware implementation of neural networks, Nat. Nanotechnol. **16**, 680 (2021).

[23] T. Oka, R. Arita, and H. Aoki, Breakdown of a Mott Insulator: A Nonadiabatic Tunneling Mechanism, Phys. Rev. Lett. **91**, 066406 (2003).

[24] H. Yamakawa, T. Miyamoto, T. Morimoto, T. Terashige, H. Yada, N. Kida, M. Suda, H. M. Yamamoto, R. Kato, K. Miyagawa, K. Kanoda, and H. Okamoto, Mott transition by an impulsive dielectric breakdown, Nat. Mater. **16**, 1100 (2017).

[25] T. Oka and H. Aoki, Ground-State Decay Rate for the Zener Breakdown in Band and Mott Insulators, Phys. Rev. Lett. **95**, 137601 (2005).

[26] M. Eckstein, T. Oka, and P. Werner, Dielectric Breakdown of Mott Insulators in Dynamical Mean-Field Theory, Phys. Rev. Lett. **105**, 146404 (2010).

[27] F. Heidrich-Meisner, I. González, K. A. Al-Hassanieh, A. E. Feiguin, M. J. Rozenberg, and E. Dagotto, Nonequilibrium electronic transport in a one-dimensional Mott insulator, Phys. Rev. B **82**, 205110 (2010).

[28] R. Kumai, Y. Okimoto, and Y. Tokura, Current-induced insulator-metal transition and pattern formation in an organic charge-transfer complex, Science **284**, 1645 (1999).

[29] S. Yamanouchi, Y. Taguchi, and Y. Tokura, Dielectric Breakdown of the Insulating Charge-Ordered State in La$_{2-x}$Sr$_x$NiO$_4$, Phys. Rev. Lett. **83**, 5555 (1999).

[30] I. Valmianski, P. Y. Wang, S. Wang, J. G. Ramírez, S. Guénon, and I. K. Schuller, Origin of the current-driven breakdown in vanadium oxides: Thermal versus electronic, Phys. Rev. B **98**, 195144 (2018).

[31] W.-R. Lee and K. Park, Dielectric breakdown via emergent nonequilibrium steady states of the electric-field-driven Mott insulator, Phys. Rev. B **89**, 205126 (2014).

[32] N. Sugimoto, S. Onoda, and N. Nagaosa, Field-induced metal-insulator transition and switching phenomenon in correlated insulators, Phys. Rev. B **78**, 155104 (2008).

[33] G. Mazza, A. Amaricci, M. Capone, and M. Fabrizio, Field-Driven Mott Gap Collapse and Resistive Switch in Correlated Insulators, Phys. Rev. Lett. **117**, 176401 (2016).

[34] J. Li, C. Aron, G. Kotliar, and J. E. Han, Electric-Field-Driven Resistive Switching in the Dissipative Hubbard Model, Phys. Rev. Lett. **114**, 226403 (2015).

[35] J. Duchene, M. Terraillon, P. Pailly, and G. Adam, Filamentary conduction in VO$_2$ coplanar thin-film devices, Appl. Phys. Lett. **19**, 115 (2003).

[36] S. Guénon, S. Scharinger, S. Wang, J. G. Ramírez, D. Koelle, R. Kleiner, and I. K. Schuller, Electrical breakdown in a V$_2$O$_3$ device at the insulator-to-metal transition, EPL **101**, 57003 (2013).

[37] J. S. Brockman, L. Gao, B. Hughes, C. T. Rettner, M. G. Samant, K. P. Roche, and S. S. P. Parkin, Subnanosecond incubation times for electric-field-induced metallization of a correlated electron oxide, Nat. Nanotechnol. **9**, 453 (2014).

[38] V. I. Polozov, S. S. Maklakov, A. L. Rakhmanov, S. A. Maklakov, and V. N. Kisel, Blow-up overheating instability in vanadium dioxide thin films, Phys. Rev. B **101**, 214310 (2020).

[39] Manca, *et al.*, Influence of thermal boundary conditions on the current-driven resistive transition in VO$_2$ microbridges, Appl. Phys. Lett. **107**, 143509 (2015).

[40] Javier Del Valle, Nicolas M. Vargas, Rodolfo Rrocco, Pavel Salevyoav Kalcheim, Pavel N. Lapa, Coline Adda, Min-Han Lee, Paul y. Wang, Lorenzo Fratino, Marcelo L. Rozenberg, and Ivan K. Schuller, Spatiotemporal characterization of the field-induced insulator-to-metal transition, Science **373**, 907 (2021).

[41] A. V. Gurevich and R. G. Mints, Self-heating in normal metals and superconductors, Rev. Mod. Phys. **59**, 941 (1987).

[42] F. Giorgianni, J. Sakai, and S. Lupi, Overcoming the thermal regime for the electric-field driven Mott transition in vanadium sesquioxide, Nat. Commun. **10**, 1159 (2019).

[43] Y. Kalcheim, A. Camjayi, J. del Valle, P. Salev, M. Rozenberg, and I. K. Schuller, Non-thermal resistive switching in Mott insulator nanowires, Nat. Commun. **11**, 2985 (2020).

[44] H. Schuler, S. Klimm, G. Weissmann, C. Renner, and S. Horn, Influence of strain on the electronic properties of epitaxial V$_2$O$_3$ thin films, Thin Solid Films **299**, 119 (1997).

[45] N. Alyabyeva, J. Sakai, M. Bavencoffe, J. Wolfman, P. Limelette, H. Funakubo, and A. Ruyter, Metal-insulator transition in V$_2$O$_3$ thin film caused by tip-induced strain, Appl. Phys. Lett. **113**, 241603 (2018).

[46] A. Ronchi, P. Homm, M. Menghini, P. Franceschini, F. Maccherozzi, F. Banfi, G. Ferrini, F. Cilento, F. Parmigiani, S. S. Dhesi, M. Fabrizio, J.-P. Locquet, and C. Giannetti, Early-stage dynamics of metallic droplets embedded in the nanotextured Mott insulating phase of V$_2$O$_3$, Phys. Rev. B **100**, 075111 (2019).

[47] Yoav Kalcheim, Nikita Butakov, Nicolas M. Vargas, Min-Han Lee, Javier del Valle, Juan Trastoy, Pavel Salev, Jon Schuller, and Ivan K. Schuller, Robust Coupling between Structural and Electronic Transitions in a Mott Material, Phys. Rev. Lett. **122**, 057601 (2019).

[48] Yoav Kalcheim, Coline Adda, Pavel Salev, Min-Han Lee, Nareg Ghazikhanian, Nicolás M. Vargas, Javier del Valle, and Ivan K. Schuller, Structural Manipulation of Phase Transitions by Self-Induced Strain in Geometrically Confined Thin Films, Adv. Funct. Mater. **30**, 2005939 (2020).

[49] Pavel Salev, Javier del Valle, Yoav Kalcheim, and Ivan K. Schuller, Giant nonvolatile resistive switching in a Mott oxide and ferroelectric hybrid, PNAS **116**, 8798 (2019).

[50] A. S. McLeod, E. van Heumen, J. G. Ramírez, S. Wang, T. Saerbeck, S. Guénon, M. Goldflam, L. Anderegg, P. Kelly, A. Mueller, M. K. Liu, I. K. Schuller, and D. N. Basov, Nanotextured phase coexistence in the correlated insulator V$_2$O$_3$, Nat. Phys. **13**, 80 (2017).

[51] P. Stoliar, L. Cario, E. Janod, B. Corraze, C. Guillot-Deudon, S. Salmon-Bourmand, V. Guiot, J. Tranchant, and M. Rozenberg, Universal electric-field-driven resistive transition in narrow-gap Mott insulators, Adv. Mater. **25,** 3222 (2013).

[52] P. Diener, E. Janod, B. Corraze, M. Querré, C. Adda, M. Guilloux-Viry, S. Cordier, A. Camjayi, M. Rozenberg, M. P. Besland, and L. Cario, How a dc Electric Field Drives Mott Insulators out of Equilibrium, Phys. Rev. Lett. **121,** 016601 (2018).

[53] G. Gopalakrishnan, D. Ruzmetov, and S. Ramanathan, On the triggering mechanism for the metal-insulator transition in thin film VO_2 devices: Electric field versus thermal effects, J. Mater. Sci. **44,** 5345 (2009).

[54] A. Ronchi, P. Franceschini, P. Homm, M. Gandolfi, G. Ferrini, S. Pagliara, F. Banfi, M. Menghini, J.-P. Locquet, and C. Giannetti, Light-Assisted Resistance Collapse in a V_2O_3-Based Mott-Insulator Device, Phys. Rev. Appl. **15,** 044023 (2021).

[55] M. K. Stewart, D. Brownstead, S. Wang, K. G. West, J. G. Ramirez, M. M. Qazilbash, N. B. Perkins, I. K. Schuller, and D. N. Basov, Insulator-to-metal transition and correlated metallic state of V_2O_3 investigated by optical spectroscopy, Phys. Rev. B **85,** 205113 (2012).

[56] J. Trastoy, Y. Kalcheim, J. del Valle, I. Valmianski, and Ivan K. Schuller, Enhanced metal-insulator transition in V_2O_3 by thermal quenching after growth, J. Mater. Sci. **53,** 9131 (2018).

[57] M. Lange, S. Guénon, F. Lever, R. Kleiner, and D. Koelle, A high-resolution combined scanning laser- and widefield polarizing microscope for imaging at temperatures from 4 K to 300 K, Rev. Sci. Instr. **88,** 123705 (2017).

[58] A. I. Poteryaev, J. M. Tomczak, S. Biermann, A. Georges, A. I. Lichtenstein, A. N. Rubtsov, T. Saha-Dasgupta, and O. K. Andersen, Enhanced crystal-field splitting and orbital-selective coherence induced by strong correlations in V_2O_3, Phys. Rev. B **76,** 085127 (2007).

[59] S.-K. Mo, J. D. Denlinger, H.-D. Kim, J.-H. Park, J. W. Allen, A. Sekiyama, A. Yamasaki, K. Kadono, S. Suga, Y. Saitoh, T. Muro, P. Metcalf, G. Keller, K. Held, V. Eyert, V. I. Anisimov, and D. Vollhardt, Prominent Quasiparticle Peak in the Photoemission Spectrum of the Metallic Phase of V_2O_3, Phys. Rev. Lett. **90,** 186403 (2003).

[60] H. Garcke and U. Weikard, Numerical approximation of the Cahn-Larché equation, Numer. Math. **100,** 639 (2005).

[61] M. Lange, Ph.D. thesis, Eberhard Karls Universität Tübingen, 2018.

[62] H. V. Keer, D. L. Dickerson, H. Kuwamoto, H. L. C. Barros, and J. M. Honig, Heat capacity of pure and doped V_2O_3 single crystals, J. Solid State Chem. **19,** 95 (1976).

[63] O. V. Lyakh, V. I. Surikov, V. I. Surikov, and N. A. Prokudina, Magnetic susceptibility and heat capacity of V_2O_3 and $V_{1.973}Me_{0.020}O_3$ (Me = Fe, Cr and Al), Russ. Phys. J **55,** 116 (2012).

Publication 3

Laser-induced quenching of metastability at the Mott-insulator to metal transition

Theodor Luibrand,[1] Lorenzo Fratino,[2,3] Farnaz Tahouni-Bonab,[1] Amihai Kronman,[4] Yoav Kalcheim,[4,5]
Ivan K. Schuller,[5] Marcelo Rozenberg,[3] Reinhold Kleiner,[1] Dieter Koelle,[1] and Stefan Guénon[1,*]

[1]*Physikalisches Institut, Center for Quantum Science (CQ) and LISA+, Eberhard
Karls Universität Tübingen, Auf der Morgenstelle 14, 72076 Tübingen, Germany*
[2]*CNRS Laboratoire de Physique Théorique et Modélisation, CY Cergy Paris Université, 95302 Cergy-Pontoise Cedex, France*
[3]*CNRS Laboratoire de Physique des Solides, Université Paris-Saclay, 91405, Orsay, France*
[4]*Department of Materials Science and Engineering, Technion –
Israel Institute of Technology, Technion City, 32000 Haifa, Israel*
[5]*Center for Advanced Nanoscience, Department of Physics, University of
California — San Diego, 9500 Gilman Drive, La Jolla, CA92093-0319, USA*

There is growing interest in strongly correlated insulator thin films because the intricate interplay of their intrinsic and extrinsic state variables causes memristive behavior that might be used for bio-mimetic devices in the emerging field of neuromorphic computing. In this study we find that laser irradiation tends to drive V_2O_3 from supercooled/superheated metastable states towards thermodynamic equilibrium, most likely in a non-thermal way. We study thin films of the prototypical Mott-insulator V_2O_3, which show spontaneous phase separation into metal-insulator herringbone domains during the Mott transition. Here, we use low-temperature microscopy to investigate how these metal-insulator domains can be modified by scanning a focused laser beam across the thin film surface. We find that the response depends on the thermal history: When the thin film is heated from below the Mott transition temperature, the laser beam predominantly induces metallic domains. On the contrary, when the thin film is cooled from a temperature above the transition, the laser beam predominantly induces insulating domains. Very likely, the V_2O_3 thin film is in a superheated or supercooled state, respectively, during the first-order phase transition, and the perturbation by a laser beam drives these metastable states into stable ones. This way, the thermal history is locally erased. Our findings are supported by a phenomenological model with a laser-induced lowering of the energy barrier between the metastable and equilibrium states.

Strongly correlated insulator thin films are the subject of intensive research in the emerging field of neuromorphic computing [1–4]. If these materials are cooled to a temperature below the transition temperature, the charge carrier mobility is considerably reduced due to electron-electron correlation effects like the Mott-Hubbard interaction (e.g., V_2O_3 [5–9]), charge transfer (e.g., rare-earth nickelates [10, 11]) or dimerization (e.g., VO_2)[12]. This reduction in charge carrier mobility results in a metal-to-insulator transition (MIT) [13]. An equivalent insulator-to-metal transition (IMT) is observed during heating. The electron-electron correlation effects cause an intricate interplay of intrinsic and extrinsic state variables that can be leveraged for engineering neuromorphic devices [14]. One way to influence strongly correlated insulator thin-film devices externally is through exposure to light. For instance, light is used to trigger resistive switching [15–18], to tune the resistive switching voltage thresholds [19] or to tune the frequency of relaxation oscillators [20] in VO_2 devices. Furthermore, because strongly correlated insulator thin-film neuromorphic devices are usually operated in a critical state at the onset of the IMT/MIT, their functionality is affected by thermodynamics of phase transitions. For instance, the hysteresis in resistance R vs temperature T curves due to the first order MIT/IMT in VO_2 is lever-

aged for multistate resistive switching [21–23]. In V_2O_3, the MIT/IMT is accompanied by structural (corundum to monclinic) and magnetic (paramagnetic to antiferromagnetic) phase transitions, providing a complex interplay of many degrees of freedom [24–27]. As a foundation of utilizing V_2O_3-based neuromorphic device applications that are implementing light as an external stimulus, one needs a better understanding of the phase transitions in V_2O_3.

We have investigated the effect of laser scanning irradiation on a V_2O_3 thin film during the IMT/MIT by acquiring photomicrographs. Here we report on laser-induced phase transitions. While at the IMT, the metal phase is induced, the insulating phase is predominantly induced at the MIT. The latter is surprising, because one might expect the main effect of the laser irradiation to be heating, which is expected to drive the system towards a more metallic state.

The sample under investigation is a continuous 300-nm-thick rf-sputtered V_2O_3 film on an r-cut sapphire substrate with gold electrodes evaporated on top (see Ref. [28] for details); Fig. 1(a) shows its $R(T)$ curve for both heating and cooling. The resistance change of four orders of magnitude at the phase transition is a sign of high film quality.

We used the same optical microscopy setup as in Lange *et al.* [29], where we have demonstrated that the change in reflectivity allows for imaging the separation of the insulating and metallic phases with $0.5\,\mu m$ spatial resolution. As described in Refs. [30, 31], the setup is a

---

* stefan.guenon@uni-tuebingen.de

cryogenic combined widefield and laser scanning micro-scope. A sketch of the experimental setup is shown in Fig. 1(b), and a detailed description is given in Ref. [32] (Sec. I).

For this study, the photomicrographs are acquired in the widefield mode with an monochromatic (532 nm) LED illumination, and the laser scanning mode is used for exposing the sample under investigation to laser light of 405 nm wavelength. The theoretical laser spot diameter on the thin-film surface is 322 nm. We have measured the incident laser power on the sample surface by replacing the sample with a photodiode. The maximum laser power is 919 μW. However, different laser powers were chosen, throughout this study. For exposure, the selected area is scanned line by line (line separation 100 nm) with the laser in the continuous wave mode as depicted in Fig. 1(b). During each line scan, the laser spot stays at a position for 13 ms then it moves to the next position at a distance of 100 nm.

The procedure to investigate the effect of laser scanning irradiation is the following:

1. A photomicrograph ($32 \times 32 \, \mu m^2$) of the thin film is acquired.

2. A selected area ($14 \times 14 \, \mu m^2$) is exposed to laser light.

3. A second photomicrograph is acquired.

4. For the differential image, the first photomicrograph is subtracted from the second.

With this procedure, the laser-induced changes from the metallic to the insulating and from the insulating to the metallic phases are mapped.

We have exposed a V_2O_3 thin film by laser light at different temperatures during the IMT/MIT (Fig. 1). The $R(T)$ curve shows a hysteresis of several Kelvins due to the first-oder nature of the IMT/MIT [7]. During heating of the sample from 80 K to room temperature, the heating was interrupted four times during the IMT, and a pristine (unirradiated) $14 \times 14 \, \mu m$ area was exposed with 0.1 mW laser power according to the procedure described above. The same procedure was chosen for cooling from room temperature to 80 K with 0.6 mW laser power. Note, that we chose different pristine areas on the sample for each scanning procedure. The photomicrographs in Fig. 1(c),(d) (in particular, D and E) show the characteristic herringbone domain pattern due to strain-induced separation of the metallic and insulating phases [29, 33]. A crucial result of this study is that during heating, mostly metallic domains are induced (dark patches in the differential images in Fig. 1(c) and (d)), whereas during cooling, predominantly insulating domains are created by laser irradiation (bright patches in the differential images in Fig. 1(c) and (d)). Furthermore, laser scanning irradiation does not smear or destroy the herringbone domain patterns but modifies them by changing the ratio
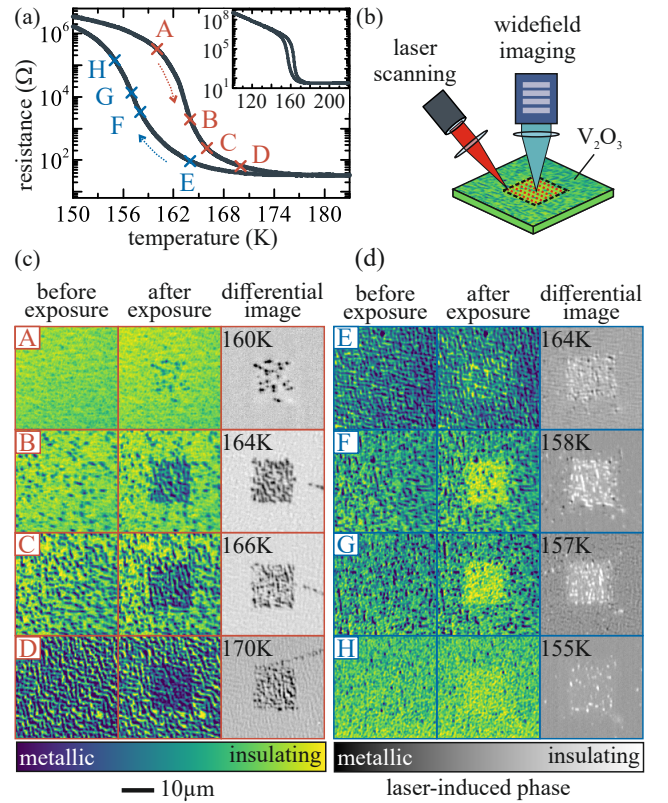

FIG. 1. (a) Zoom into the phase transition region of the $R(T)$ curve. The red and blue dashed arrows indicate the heating and cooling branch, respectively. Inset: Full $R(T)$ curve of the V_2O_3 thin film sample under investigation with same units as in the main graph. The capital letters mark the set-temperatures in one thermal cycle, at which separated squares in the V_2O_3 thin film were irradiated using the laser scanning mode. (b) Simplified schematic of the measurement setup. Photomicrographs are acquired by widefield microscopy before and after laser scanning within the dashed square of pristine areas. (c) Photomicrograph series demonstrating the laser scanning irradiation effect acquired during one heating run. For the differential images, the image before laser irradiation was subtracted from the image after scanning. The image contrasts were optimized for every temperature. (d) Photomicrograph series acquired during cooling, analogous to (c).

of the metallic and insulating surface areas. In an additional experiment on a patterned V_2O_3 thin film microbridge (see Fig. S2 in Ref. [32]) we show, that indeed the laser-scanning-induced phase change has a significant effect on the film resistivity. Moreover, we observe that the size of the laser-induced domains is similar to the size of the domains of the temperature-driven phase transition without laser exposure. This indicates, that domain walls permeate the whole film, and that the laser-induced phase transition is not only due to a surface effect.

We also modified the laser irradiation procedure to determine the power thresholds for laser-induced phase changes during heating and cooling (see Sec. III in
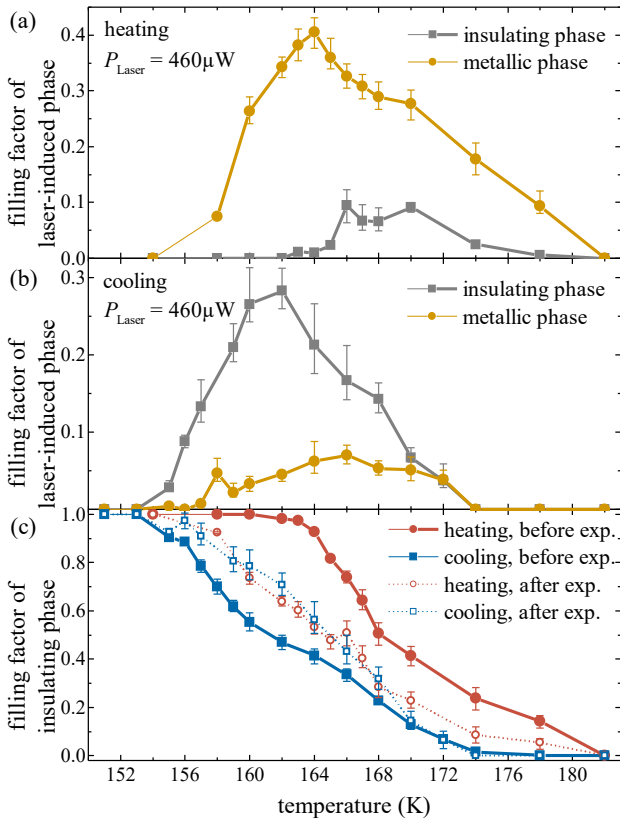
FIG. 2. Temperature dependence of metal and insulator filling factors affected by laser irradiation of $460\,\mu$W. (a) Filling factors of the metallic and insulating phases induced by laser irradiation during heating. (b) Same filling factors during cooling. (c) Filling factors of the insulating phase during one thermal cycle.

Ref. [32] for details). It was found that laser irradiation already at relatively low power levels induces a phase change during heating (i.e., IMT), while during cooling (i.e., MIT), the required laser power is considerably larger. Moreover, the temperature range, in which a laser-induced phase change was observable, is larger during IMT, compared to MIT. Hence, the heating branch of the transition seems to be more sensitive to laser irradiation than the cooling branch.

For a quantitative analysis of the laser-induced phase changes, we investigated the filling factors, i.e., the ratio between the surface area of a particular phase and the total surface area of interest at a laser power of $460\,\mu$W. This laser power was chosen because it is far from the minimum and maximum threshold values for both cooling and heating (see Sec. III in Ref. [32]). As mentioned above, the metallic and insulating thin-film areas can be clearly distinguished by their brightness level in the photomicrographs (see Fig. 1 and [29]). However, these brightness levels change from micrograph to micrograph. Therefore, the following evaluation procedure was used for determining the filling factors. We visually inspected the (differential) micrographs in Fiji [34] and chose an

upper and lower limit for the brightness that separates the particular two phases. A third brightness level was calculated by averaging the upper and lower limit. For these three brightness values, we calculated the filling factors, which correspond to the data points and the error bars in Fig. 2, using a Python routine.

Figure 2(a) and (b) show the temperature dependence of the filling factors of the laser-induced metallic and insulating phases during heating and cooling, respectively. Except for the fact that in the heating case, predominantly the metallic, and in the cooling case, predominantly the insulating phase is created, the overall behavior is very similar: the laser irradiation switches a considerable percentage of the thin-film area during the IMT from insulating to metallic (40% at 164 K) and during the MIT from metallic to insulating (28% at 162 K). Furthermore, in both cases, there is a temperature interval in which a smaller amount of the minor phase (insulating at the IMT and metallic at the MIT) is induced as well.

Figure 2(c) shows the filling factor of the insulating phase before and after laser irradiation. The error bars of the before-irradiation graphs are smaller compared to the after-irradiation graphs because a larger area was used for determining the filling factors before irradiation. Like the $R(T)$-curves shown in Fig. 1(a), the before-irradiation curves are hysteretic due to the first-order character of the IMT/MIT phase transitions. Most importantly, the after-irradiation curves (dashed lines) lay between the curves before irradiation and are almost identical for temperatures at 168 K and below (solid lines). This implies that after irradiation, it is no longer possible to decide (by means of the filling factor) whether the film was in the heating or cooling branch. In this sense, laser irradiation above the power threshold erases the thermal history of the V_2O_3 thin film.

The most intriguing result of this study is that laser irradiation predominantly induces insulating domains in large amounts during cooling. Considering the laser spot as a local heat source, it is not surprising that laser irradiation induces metallic domains since the metallic phase is the high-temperature phase of the Mott transition. Indeed, we observe this behavior during heating of the sample through the IMT. However, the predominant laser-induced creation of insulating domains during cooling is puzzling. In other words, why does the effect of laser irradiation depend on the thermal history? To answer this question, the thermodynamic nature of the MIT/IMT of the V_2O_3 thin film must be considered.

The thermodynamic description of V_2O_3 thin films is the subject of ongoing research [35–37]. It is recognized that at the MIT, three phase transitions are coupled: first, an electronic transition due to Mott-Hubbard charge carrier localization, second, a magnetic transition from a paramagnetic-to-antiferromagnetic state, and third, a structural transition from corundum to a monoclinic crystal structure. Furthermore, as indicated in Ref. [29], the characteristic herringbone domain pattern

resembles the solutions of the Cahn-Larché equation describing a phase separation due to spinodal decomposition [38]. Other studies also indicate that the IMT/MIT is associated with a spinodal instability [39, 40]. Despite those intricate details, the $R(T)$-hysteresis and the associated latent heat at the IMT and MIT clearly indicate a first-order phase transition. Consequently, it is safe to assume that during heating the V_2O_3 thin film is in a metastable superheated state, and during cooling it is in a metastable supercooled state. The most likely interpretation of our results is that the perturbation releases the V_2O_3 thin film from its metastable state, and when the laser spot moves to a new position, the thin film relaxes locally into a stable state. The general details of the perturbation induced by the laser beam are elusive and additional effects might be at play, for instance, a photoinduced change of the $3d$-orbital occupation could trigger the formation of metallic nanodroplets in the IMT [41].

With respect to the MIT we measured electrical transport properties during minor thermal cycles to investigate how heating affects a V_2O_3 thin film in the critical state. This procedure emulates a heat source that changes the temperature gradually on a large length scale. A detailed description and discussion of these additional experiments can be found in Ref. [32] (Sec. IV). Although we found that a minor heating cycle can indeed increase the resistance, the effect is not strong enough to account for what we observed in the laser irradiation experiment.

To elaborate on the matter of metastability, we discuss a phenomenological numerical model. In a two-dimensional (2D) resistor network, each site can either be metallic or insulating, depending on the local temperature, which is updated at every simulation step. Solving Kirchhoff's laws, currents and voltages on each site are determined. A first-order Landau-type free energy functional provides stable and metastable states separated by a barrier. The laser irradiation is implemented in the model by decreasing the barrier height to drive transitions between insulating and metallic states. For each site, the escape from a metastable state was determined by comparing random numbers to Boltzmann factors with a constant number of iterations. If the escape criterion is fulfilled, the transition probability is given by a Boltzmann distribution; see Sec. V in Ref. [32] for details.

Our model reproduces the hysteresis in the $R(T)$ curves, as shown in Fig. 3(a). Figure 3(b) shows the evolution of the filling factor of the insulating phase at different laser intensities. With increasing laser intensity the hysteresis is diminished, and eventually it is completely suppressed, similarly to the experimental results in Fig. 2(c). In Fig. 3(c) we present a simulation series of selected network maps before and after laser exposure with moderate laser intensity ($\Gamma/k_B = 600\,\mathrm{K}$), and their corresponding differential images. For heating, the laser induces predominantly metallic sites (Fig. 3(c)), for cool-

ing insulating sites (Fig. 3(d)). We note that during heating, the majority of sites goes into a metallic state (indicated by black squares in the differential maps), while a few sites revert back to an insulating state (indicated by white squares in the differential maps); this reproduces very well the experimental results. Moreover, this behavior reverses in the cooling branch (Fig. 3(d), again in agreement with experimental observations. So, according to the simulations, the laser irradiation enhances the process of relaxing the system from a metastable state.

In conclusion, we can state that a V_2O_3 thin film in the metastable state at the IMT/MIT is highly susceptible to a local perturbation by a focused laser beam at the sub-micrometer scale. Whether the laser perturbation predominantly creates a metallic or insulating phase depends on whether the film is in the heating or cooling branch. Our observations tell that the laser beam brings the system from a supercooled/superheated state to the equilibrium one, provided that the laser power is sufficient to overcome corresponding energy barriers. This implies, that laser scanning irradiation can be used to effectively erase thermal history and provides a novel method to reset memristive devices locally. Our experiments may also be considered as a clear indication that external stimuli on a strongly correlated thin film in a critical state can result in unexpected and presumably non-thermal effects. Non-thermal effects have been in-
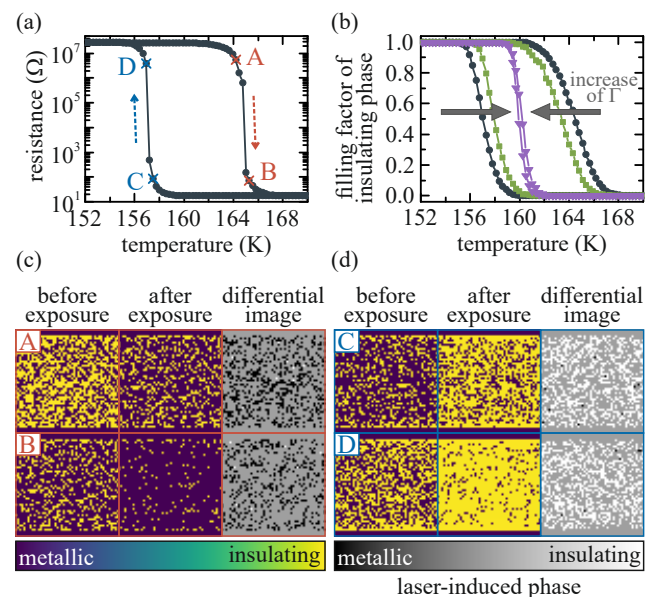

FIG. 3. Results of numerical simulations based on a 2D resistor network model. (a) $R(T)$ curves; arrows indicate heating (red) and cooling (blue) branches. (b) Filling factors of the insulating phase vs. T, for various values of laser intensity $\Gamma/k_B = 0$ (grey circles), $600\,\mathrm{K}$ (green squares) and $1200\,\mathrm{K}$ (purple triangles). (c) Selected network maps before laser exposure, after laser exposure with $\Gamma/k_B = 600\,\mathrm{K}$, and their corresponding differential images for two temperature values in the heating branch, as indicated with capital letters in (a). (d) same as in (c) – for the cooling branch.

vestigated in ultra-fast pump-probe experiments on VO_2 and V_2O_3 [41–45]. In contrast, in our experiment we have a quasi-static setting. The findings of this study may trigger additional experimental and theoretical studies to explore the thermodynamics of phase transitions and local perturbations in this class of materials.

ACKNOWLEDGMENTS

References

[1] I. K. Schuller, R. Stevens, R. Pino, and M. Pechan, Neuromorphic Computing – From Materials Research to Systems Architecture Roundtable, 10.2172/1283147 (2015).

[2] J. del Valle, J. G. Ramírez, M. J. Rozenberg, and I. K. Schuller, Challenges in materials and devices for resistive-switching-based neuromorphic computing, Journal of Applied Physics **124**, 211101 (2018).

[3] A. Hoffmann, S. Ramanathan, J. Grollier, A. D. Kent, M. J. Rozenberg, I. K. Schuller, O. G. Shpyrko, R. C. Dynes, Y. Fainman, A. Frano, E. E. Fullerton, G. Galli, V. Lomakin, S. P. Ong, A. K. Petford-Long, J. A. Schuller, M. D. Stiles, Y. Takamura, and Y. Zhu, Quantum materials for energy-efficient neuromorphic computing: Opportunities and challenges, APL Materials **10**, 070904 (2022).

[4] T. J. Park, S. Deng, S. Manna, A. N. M. N. Islam, H. Yu, Y. Yuan, D. D. Fong, A. A. Chubykin, A. Sengupta, S. K. R. S. Sankaranarayanan, and S. Ramanathan, Complex Oxides for Brain-Inspired Computing: A Review, Advanced Materials **35**, 2203352 (2022).

[5] F. J. Morin, Oxides Which Show a Metal-to-Insulator Transition at the Neel Temperature, Physical Review Letters **3**, 34 (1959).

[6] D. B. McWhan and J. P. Remeika, Metal-Insulator Transition in $(V_{1-x}Cr_x)_2O_3$, Physical Review B **2**, 3734 (1970).

[7] D. B. McWhan, A. Menth, J. P. Remeika, W. F. Brinkman, and T. M. Rice, Metal-insulator Transitions in Pure and Doped V_2O_3, Physical Review B **7**, 1920 (1973).

[8] A. Georges, G. Kotliar, W. Krauth, and M. J. Rozenberg, Dynamical mean-field theory of strongly correlated fermion systems and the limit of infinite dimensions, Reviews of Modern Physics **68**, 13 (1996).

[9] P. Limelette, A. Georges, D. Jerome, P. Wzietek, P. Metcalf, and J. M. Honig, Universality and Critical Behavior at the Mott Transition, Science **302**, 89 (2003).

[10] J. Torrance, P. Lacorre, A. Nazzal, E. Ansaldo, and C. Niedermayer, Systematic study of insulator-metal transitions in perovskites $RNiO_3$ (R=Pr,Nd,Sm,Eu) due to closing of charge-transfer gap, Physical Review B **45**, 8209 (1992).

[11] S. Catalano, M. Gibert, J. Fowlie, J. Íñiguez, J.-M. Triscone, and J. Kreisel, Rare-earth nickelates $RNiO_3$: thin films and heterostructures, Reports on Progress in Physics **81**, 046501 (2018).

[12] S. Biermann, A. Poteryaev, A. I. Lichtenstein, and A. Georges, Dynamical Singlets and Correlation-Assisted Peierls Transition in VO_2, Physical Review Letters **94**, 026404 (2005).

[13] M. Imada, A. Fujimori, and Y. Tokura, Metal-insulator transitions, Reviews of Modern Physics **70**, 1039 (1998).

[14] Y. Zhou and S. Ramanathan, Mott Memory and Neuromorphic Devices, Proceedings of the IEEE **103**, 1289 (2015).

[15] B.-J. Kim, G. Seo, and Y. W. Lee, Bidirectional laser triggering of planar device based on vanadium dioxide thin film, Optics Express **22**, 9016 (2014).

[16] J. Kim, S. J. Jeong, B.-J. Kim, and Y. W. Lee, Laser-triggered current gating based on photothermal effect in VO_2 thin-film device using CO_2 laser, Applied Physics B **124**, 67 (2018).

[17] G. Seo, B.-J. Kim, Y. Wook Lee, and H.-T. Kim, Photo-Assisted Bistable Switching Using Mott Transition in Two-Terminal VO_2 Device, Applied Physics Letters **100**, 011908 (2012).

[18] G. Li, D. Xie, H. Zhong, Z. Zhang, X. Fu, Q. Zhou, Q. Li, H. Ni, J. Wang, E.-j. Guo, M. He, C. Wang, G. Yang, K. Jin, and C. Ge, Photo-Induced Non-Volatile VO_2 Phase Transition for Neuromorphic Ultraviolet Sensors, Nature Communications **13**, 1729 (2022).

[19] Y.-W. Lee, E.-S. Kim, B.-S. Shin, and S.-M. Lee, High-Performance Optical Gating in Junction Device based on Vanadium Dioxide Thin Film Grown by Sol-Gel Method, Journal of Electrical Engineering and Technology **7**, 784 (2012).

[20] G. Seo, B.-J. Kim, H.-T. Kim, and Y. W. Lee, Photo-Assisted Electrical Oscillation in Two-Terminal Device Based on Vanadium Dioxide Thin Film, Journal of Lightwave Technology **30**, 2718 (2012).

[21] T. Driscoll, H.-T. Kim, B.-G. Chae, M. D. Ventra, and D. N. Basov, Phase-transition driven memristive system, Applied Physics Letters **95**, 043503 (2009).

[22] A. Rana, C. Li, G. Koster, and H. Hilgenkamp, Resistive switching studies in VO_2 thin films, Scientific Reports **10**, 3293 (2020).

[23] X. Gao, C. M. M. Rosário, and H. Hilgenkamp, Multilevel operation in VO_2-based resistive switching devices, AIP Advances **12**, 015218 (2022).

[24] Y. Kalcheim, N. Butakov, N. M. Vargas, M.-H. Lee, J. del Valle, J. Trastoy, P. Salev, J. Schuller, and I. K. Schuller, Robust Coupling between Structural and Electronic Transitions in a Mott Material, Physical Review Letters **122**, 057601 (2019).

[25] B. A. Frandsen, Y. Kalcheim, I. Valmianski, A. S. McLeod, Z. Guguchia, S. C. Cheung, A. M. Hallas, M. N. Wilson, Y. Cai, G. M. Luke, Z. Salman, A. Suter, T. Prokscha, T. Murakami, H. Kageyama, D. N. Basov, I. K. Schuller, and Y. J. Uemura, Intertwined magnetic, structural, and electronic transitions in V_2O_3, Physical Review B **100**, 235136 (2019).

[26] J. Trastoy, A. Camjayi, J. del Valle, Y. Kalcheim, J.-P. Crocombette, D. A. Gilbert, J. A. Borchers, J. E. Villegas, D. Ravelosona, M. J. Rozenberg, and I. K. Schuller, Magnetic field frustration of the metal-insulator transition in V_2O_3, Physical Review B **101**, 245109 (2020).

[27] E. Barazani, D. Das, C. Huang, A. Rakshit, C. Saguy, P. Salev, J. del Valle, M. C. Toroker, I. K. Schuller, and Y. Kalcheim, Positive and Negative Pressure Regimes in Anisotropically Strained V_2O_3 Films, Advanced Functional Materials **33**, 2211801 (2023).

[28] M. K. Stewart, D. Brownstead, S. Wang, K. G. West, J. G. Ramírez, M. M. Qazilbash, N. B. Perkins, I. K. Schuller, and D. N. Basov, Insulator-to-Metal Transition and Correlated Metallic State of V_2O_3 Investigated by Optical Spectroscopy, Physical Review B **85**, 205113 (2012).

[29] M. Lange, S. Guénon, Y. Kalcheim, T. Luibrand, N. M. Vargas, D. Schwebius, R. Kleiner, I. K. Schuller, and D. Koelle, Imaging of Electrothermal Filament Formation in a Mott Insulator, Physical Review Applied **16**, 054027 (2021).

[30] M. M. Lange, S. Guénon, F. Lever, R. Kleiner, and D. Koelle, A High-Resolution Combined Scanning Laser and Widefield Polarizing Microscope for Imaging at Temperatures from 4 K to 300 K, Review of Scientific Instruments **88**, 123705 (2017).

[31] M. M. Lange, A High-Resolution Polarizing Microscope for Cryogenic Imaging: Development and Application to Investigations on Twin Walls in $SrTiO_3$ and the Metal-Insulator Transition in V_2O_3, Ph.D. thesis, Universität Tübingen (2018).

[32] See Supplemental Material at [URL] for details on the sample and measurement setup, a microbridge experiment, thresholds of laser scanning irradiation, analysis of thermal effects via minor loop measurements, and Mott resistor network simulation.

[33] A. S. McLeod, E. van Heumen, J. G. Ramírez, S. Wang, T. Saerbeck, S. Guénon, M. Goldflam, L. Anderegg, P. Kelly, A. Mueller, M. K. Liu, I. K. Schuller, and D. N. Basov, Nanotextured Phase Coexistence in the Correlated Insulator V_2O_3, Nature Physics **13**, 80 (2016).

[34] J. Schindelin, I. Arganda-Carreras, E. Frise, V. Kaynig, M. Longair, T. Pietzsch, S. Preibisch, C. Rueden, S. Saalfeld, B. Schmid, J.-Y. Tinevez, D. J. White, V. Hartenstein, K. Eliceiri, P. Tomancak, and A. Cardona, Fiji: an open-source platform for biological-image analysis, Nature Methods **9**, 676 (2012).

[35] C. Castellani, C. D. Castro, D. Feinberg, and J. Ranninger, New Model Hamiltonian for the Metal-Insulator Transition, Physical Review Letters **43**, 1957 (1979).

[36] G. Kotliar, E. Lange, and M. J. Rozenberg, Landau Theory of the Finite Temperature Mott Transition, Physical Review Letters **84**, 5180 (2000).

[37] M. I. Díaz, J. E. Han, and C. Aron, Electrically Driven Insulator-to-Metal Transition in a Correlated Insulator: Electronic Mechanism and Thermal Description, Physical Review B **107**, 195148 (2023).

[38] H. Garcke and U. Weikard, Numerical Approximation of the Cahn-Larché Equation, Numerische Mathematik **100**, 639 (2005).

[39] T. Bar, S. K. Choudhary, M. A. Ashraf, K. Sujith, S. Puri, S. Raj, and B. Bansal, Kinetic Spinodal Instabilities in the Mott Transition in V_2O_3: Evidence from Hysteresis Scaling and Dissipative Phase Ordering, Physical Review Letters **121**, 045701 (2018).

[40] S. Kundu, T. Bar, R. K. Nayak, and B. Bansal, Critical Slowing Down at the Abrupt Mott Transition: When the First-Order Phase Transition Becomes Zeroth Order and Looks Like Second Order, Physical Review Letters **124**, 095703 (2020).

[41] A. Ronchi, P. Homm, M. Menghini, P. Franceschini, F. Maccherozzi, F. Banfi, G. Ferrini, F. Cilento, F. Parmigiani, S. S. Dhesi, M. Fabrizio, J.-P. Locquet, and C. Giannetti, Early-Stage Dynamics of Metallic Droplets Embedded in the Nanotextured Mott Insulating Phase of V_2O_3, Physical Review B **100**, 075111 (2019).

[42] F. Giorgianni, J. Sakai, and S. Lupi, Overcoming the thermal regime for the electric-field driven Mott transition in vanadium sesquioxide, Nature Communications **10**, 1159 (2019).

[43] A. Cavalleri, C. Tóth, C. W. Siders, J. A. Squier, F. Ráksi, P. Forget, and J. C. Kieffer, Femtosecond Structural Dynamics in VO_2 during an Ultrafast Solid-Solid Phase Transition, Physical Review Letters **87**, 237401 (2001).

[44] S. Wall, S. Yang, L. Vidas, M. Chollet, J. M. Glownia, M. Kozina, T. Katayama, T. Henighan, M. Jiang, T. A. Miller, D. A. Reis, L. A. Boatner, O. Delaire, and M. Trigo, Ultrafast disordering of vanadium dimers in photoexcited VO_2, Science **362**, 572 (2018).

[45] M. R. Otto, L. P. René de Cotret, D. A. Valverde-Chavez, K. L. Tiwari, N. Émond, M. Chaker, D. G. Cooke, and B. J. Siwick, How optical excitation controls the structure and properties of vanadium dioxide, Proceedings of the National Academy of Sciences **116**, 450 (2018).

Supplemental material: Laser-induced quenching of metastability at the Mott-insulator to metal transition
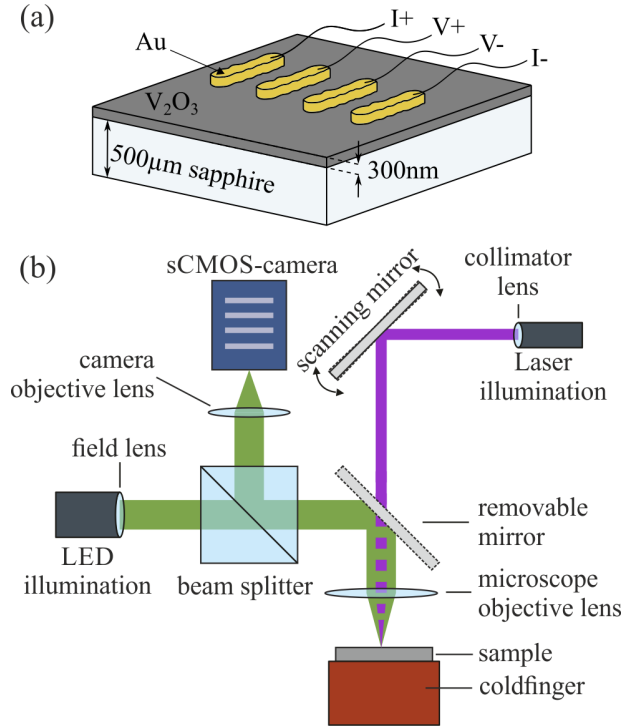
T. Luibrand *et al.*

CONTENTS

FIG. S1.   (a) V_2O_3 thin-film sample under investigation. Four parallel gold electrodes are used for measuring the $R(T)$ relation. (b) Simplified schematic diagram of the combined widefield and laser scanning microscope. The removable mirror is used to switch between the two operation modes.

I.   SAMPLE AND MEASUREMENT SETUP

The sample under investigation (Fig. S1(a)) is a continuous 300-nm-thick rf-sputtered V_2O_3 film on an r-cut sapphire substrate. Using a shadow mask, four 2-mm-long parallel gold electrodes with a distance of $1.5\,mm$ were evaporated as contacts for resistance measurements. The sample is mounted in vacuum on the coldfinger of a liquid Helium continuous-flow cryostat with a temperature range of $4.2\,K$ to $300\,K$. Electric transport measurements were performed using a Keithley 2400 SourceMeter configured as a current source.

The experimental setup is a cryogenic combined widefield and laser scanning microscope, which is described in detail in [1, 2]. Figure S1(b) shows a simplified schematic of the microscope setup that can be operated either in the widefield or in the laser scanning mode.

The illumination for the widefield microscope is realized by a LED with $532\,nm$ wavelength and follows a Köhler illumination scheme. The depicted field lens is used to define the illuminated sample area. After passing a beam splitter, the light is reflected by a removable mirror and is focused onto the sample by the microscope objective lens. The microscope objective has a high numerical aperture (NA = 0.8), which allows for a working distance of $1\,mm$. After reflection from the sample, the light travels the same way back, is deflected by the beam splitter and then focused onto the sensor of a low noise sCMOS camera. This widefield microscope has a field of view (FOV) of $500\times500\,\mu m^2$ and a spatial resolution of $0.48\,\mu m$. The entire optical path of the widefield microscope is polarization sensitive, which however is not relevant for this study.

The illumination for the laser scanning microscope is provided by a 405-nm-laser diode coupled into a single mode fiber. The laser light is collimated and thereafter reflected by a fast steering mirror, that serves as scanning mirror. In order to use this operation mode, the removable mirror is not inserted in the beam path. The laser beam is focused onto the sample by the microscope objective lens. Assuming a Gaussian beam profile, the theoretical laser spot diameter is $322\,nm$ ($1/e^2$ diameter). The FOV of the laser scanning microscope is identical with the FOV of the widefield microscope. The polarization sensitive components and the detector unit of the laser light are not included here, because in this study, we use the laser scanning microscope exclusively for irradiation.
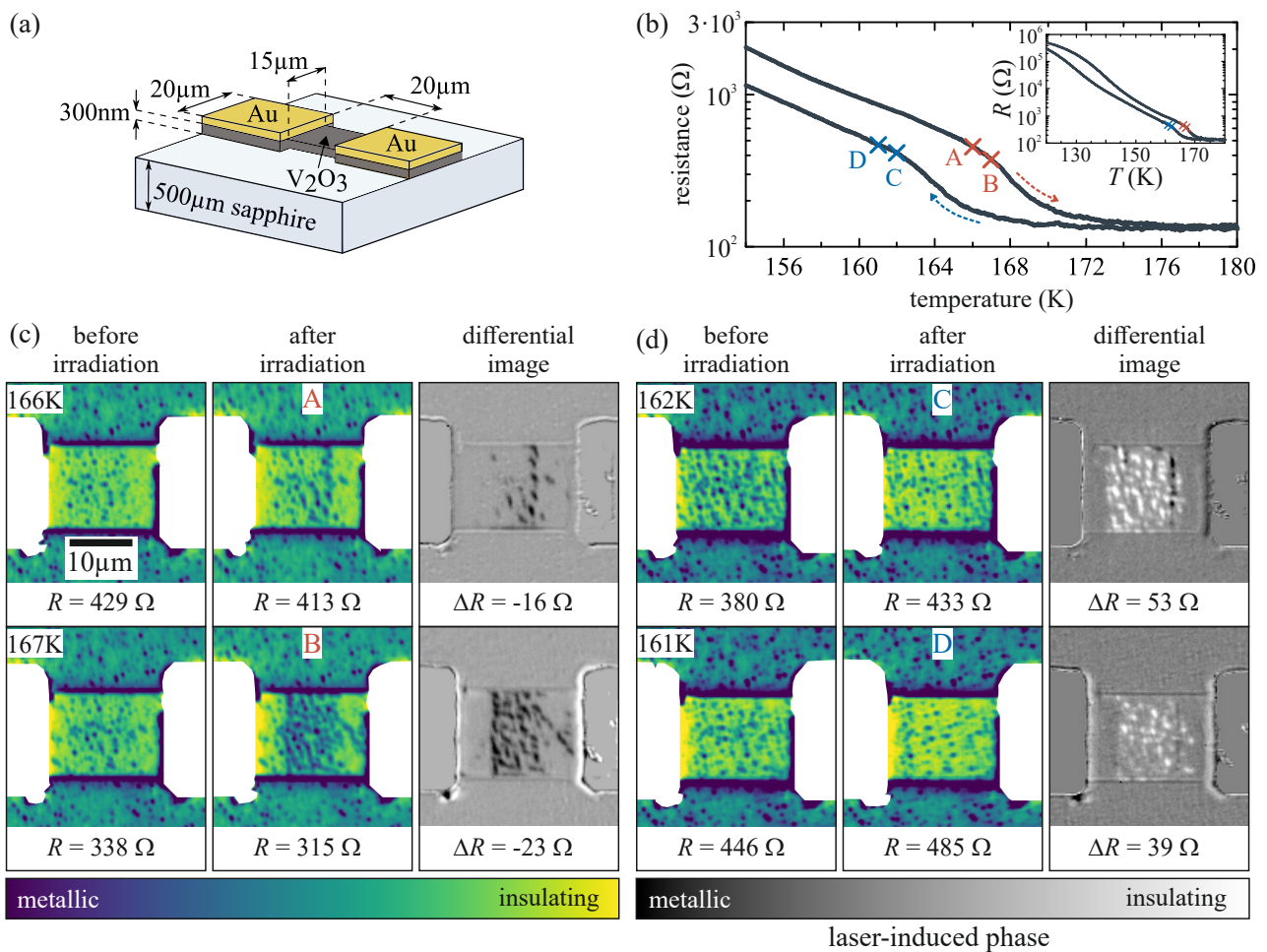
FIG. S2. Effect of laser irradiation on the resistance of a patterned V_2O_3 microbridge. (a) Schematic of planar microbridge device under test. (b) $R(T)$ curves; red and blue dashed arrows indicate the heating and cooling branch, respectively. Capital letters mark the set-temperatures, at which the device was irradiated. Inset: $R(T)$ curves on expanded T scale. (c) Photomicrographs demonstrating the laser irradiation effet acquired during one heating run. For the differential images, the image before laser irradiation was subtracted from the image after scanning. The image contrasts on the microbridge were optimized for both temperatures. The two Au electrodes used for the two point measurements are the rectangles in overload at the left and right, respectively. The device resistance and the device resistance change due to laser irradiation are shown below the micrographs. (d) analog to (c), but in the cooling branch.

II. MICROBRIDGE EXPERIMENT

In order to confirm the hypothesis, that laser scanning indeed induces phase transitions, we investigated its effect on the electrical properties of a V_2O_3 microbridge device in an additional experiment. The sample under investigation is a planar microbridge device patterned in a 300-nm-thick film V_2O_3 thin-film (same deposition procedure as in Sec. I) using Ar ion milling, followed by Au deposition and lift-off to define Au contacts (see Fig. S2(a) for device dimensions). The $R(T)$ curve Fig. S2(b) shows irregular behaviour: at the MIT/MIT, the change in resistance is only about one order of magnitude, and the insulating state still shows a relatively low resistance, i.e., the microbridge seems to be shunted. Possibly, it is shunted at the edges of the microbridge or the V_2O_3 film was not completely etched down to the substrate during the Ar-ion milling process leaving a thin ion-damaged residual layer. Nevertheless, the device is still suitable to qualitatively assess the effect of laser irradiation on the film resistivity.

For the two-terminal layout we assume a well-defined homogeneous current distribution in the microbridge. To bring the sample in a defined state in the heating branch, we used a thermal cycling procedure. This implies cooling the sample to a temperature, where the hysteresis is closed (in this case $T = 80\,\mathrm{K}$) followed by heating to the target temperature. The same device was used for each laser-irradiation scan, so thermal cycling is required to bring the
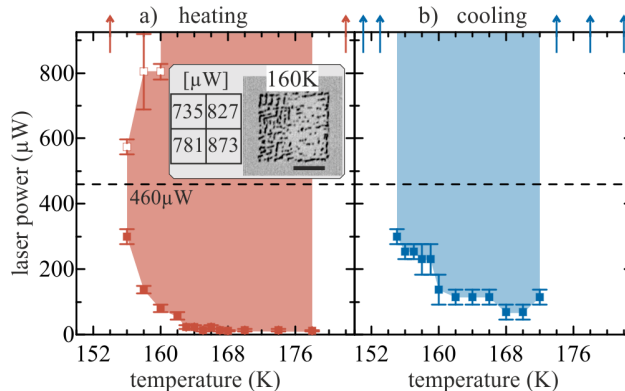
FIG. S3. Power thresholds vs. temperature for laser irradiation-induced phase changes. The horizontal black dashed line indicates the laser intensity used in Fig. 2 in the main manuscript. The vertical arrows on top of the figure indicate temperatures, at which the laser does not induce a phase change. (a) heating branch. Inset: Differential image of a laser irradiation pattern at $160\,\mathrm{K}$. The corresponding laser intensities are displayed on the left axis. At laser intensities of $827\,\mu\mathrm{W}$ and above, a phase change is only induced at the edge of the irradiated area. The scale bar indicates $10\,\mu\mathrm{m}$. (b) cooling branch.

sample in a defined pristine state for imaging at every single set temperature. At every set temperature – after acquiring a widefield micrograph (see left columns of Fig. S2(c) and (d)) – a single stripe of $\sim 10\,\mu\mathrm{m}$ width across the middle of the bridge was scanned with the laser beam (same scanning parameters as in the main manuscript). After irradiation a widefield micrograph was acquired (see middle columns of Fig. S2(c) and (d)). The right columns of Fig. S2(c) and (d) show differential images, i.e., the image before irradiation was subtracted from the image after irradiation. Simultaneously, we measured the device resistance before and after laser-irradiation with a bias current of $1\,\mu\mathrm{A}$.

Analogous to the results shown in the main manuscript, metallic and insulating phases are induced by laser irradiation, which show up as black and white patches, respectively, in the differential images. Clearly, the data obtained on this microbride show, that in the heating branch predominantly the metallic phase is induced, and that comes with a reduction of the device resistance. In the cooling branch, mostly the insulating phase is induced, which leads to a significant increase of the device resistance.

III. THRESHOLDS OF LASER SCANNING IRRADIATION

We modified the laser irradiation procedure to determine the power thresholds for laser-induced phase changes during heating and cooling. Instead of scanning the whole $22 \times 22\,\mu\mathrm{m}^2$ area with the same intensity, four $11 \times 11\,\mu\mathrm{m}^2$ quadrants are exposed with different laser powers of $230\,\mu\mathrm{W}$, $460\,\mu\mathrm{W}$, $689\,\mu\mathrm{W}$, and $919\,\mu\mathrm{W}$. The two consecutive quadrants, for which the first shows no and the next some laser-induced phase change, are chosen by examining the corresponding photomicrographs. Following a nested interval procedure, an additional pristine area is exposed to a quadrant pattern, with the minimum and maximum laser power corresponding to the power levels of the two consecutive quadrants chosen before. Using the photomicrographs of this pattern, the lower and upper limits of the laser power threshold are estimated, and these limits are averaged to calculate the threshold value.

The results are shown in Fig. S3. The temperature range, in which laser irradiation affects the V_2O_3 film, is larger during heating than during cooling. Further, the minimal power threshold in the heating branch is $11.5\,\mu\mathrm{W}$ (at $168\,\mathrm{K}$ and $178\,\mathrm{K}$), which corresponds to a theoretical $0.3\,\mathrm{mW}/\mu\mathrm{m}^2$ peak intensity assuming a Gaussian point spread function. However, the minimal power threshold in the cooling branch is six times larger ($69\,\mu\mathrm{W}$, peak intensity $1.7\,\mathrm{mW}/\mu\mathrm{m}^2$). During heating at low temperatures between 156 K and 160 K, the laser irradiation effect is reduced for high power levels, and the induced phase changes are mainly limited to the edges of the exposed area (see inset Fig. S3(a)). Empty markers in Fig. S3 indicate the corresponding laser power values. A similar effect was not observed during cooling.

IV. THERMAL EFFECTS: MINOR LOOP EXPERIMENT

Since the laser irradiation effect discussed in the main manuscript involves focusing the beam onto a very small region, it is important to check whether the observed phenomenology could simply arise from heating. To address
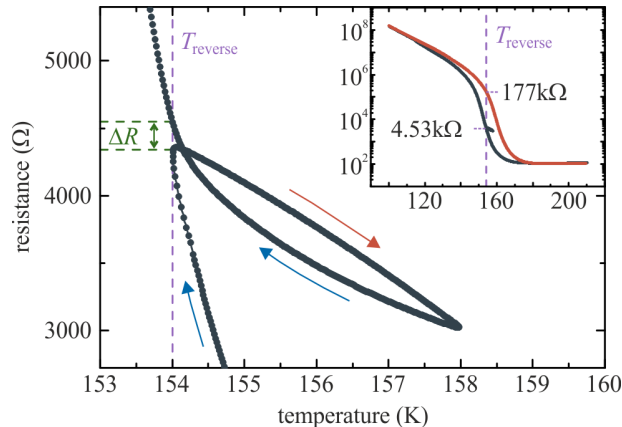
FIG. S4. Effect of thermal cycle on the cooling branch. $R(T)$ curve for 100-nm-thick V_2O_3 including a minor temperature cycle acquired in the middle of the cooling curve (cooling is marked by blue arrows, heating by the red arrow), starting at $T_{reverse}$ =154 K (as indicated by the purple dashed line). The full thermal cycle is shown in the inset (same units as in the main graph), heating curve is indicated in red).

this issue, we performed R vs T measurements on a continuous 100-nm-thick rf-sputtered V_2O_3 film on r-cut sapphire [3], with various temperature ramp protocols which would mimic possible laser-induced heating effects. We are aware of the limitation of the difference between smooth adiabatic thermal cycling of the entire thin film and a local laser-induced thermal perturbation.

Here we focus on measurements conducted on the cooling curve where the experiments on laser irradiation described in the main manuscript showed a surprising increase in the insulating phase fraction in considerably large amounts. To check whether a simple heating-cooling thermal cycle may induce a similar effect, we performed the following experiments: first, we warmed the sample up to 210 K to ensure that it is in the fully metallic phase and then slowly cooled it to $T_{reverse}$ =154 K which is in the middle of the resistive transition. This reversal temperature exhibits the maximum slope of $\log(R)$ vs T, where the largest effects are expected in resistance change due to the proximity to the percolation threshold. After reaching $T_{reverse}$ we performed a minor heating loop, i.e., the sample was heated up by a certain temperature ΔT and then cooled down to 100 K. Several runs were conducted with various values of ΔT.

An example of the resistance recorded during such a procedure is shown in Fig. S4 for $\Delta T = 4$ K which showed the most pronounced effect, i.e., the strongest change ΔR in resistance at $T_{reverse}$ measured after performing the minor heating loop. During most of this partial temperature cycle the resistance of the minor heating curve is higher than during cooling, as expected. However, as $T_{reverse}$ is approached again during cooling the resistance increases and crosses that of the minor heating curve. After completion of the minor thermal cycle, $R(T_{reverse}) = 4530\,\Omega$, which corresponds to an increase by $\sim 5\,\%$ over the starting resistance $R(T_{reverse}) = 4330\,\Omega$ measured before initiating the minor temperature cycle. This increase in resistance is qualitatively similar to the effect observed in the case of laser irradiation, where after exposure the insulating phase fraction has increased (see panels E-H in Fig. 1(d) in the main manuscript). Contrary to the large effect observed in response to laser irradiation, which drives the film close to thermodynamic equilibrium (increase in filling factor of the insulating phase by $\sim 20\,\%$ in the middle of the cooling branch; see Fig. 2(c) in the main manuscript), the minor heating cycles result in only a slight increase of $\sim 5\,\%$ in resistance as compared to the original cooling branch. We note that the minor thermal cycling loop experiments were repeated for several ΔT values and that from $\Delta T = 2$ K to 8 K none showed an increase in resistance at $T_{reverse}$ larger than 5 %.

However, quantitatively, it is found that the effect of temperature cycling on the phase fraction is significantly smaller than that of the laser. Considering Fig. 2(c) in the main manuscript, the filling factors of the insulating phase at 157 K after laser exposure and at 155 K before exposure in the cooling branch yield the same value of ~ 0.9. Hence, the impact of the laser irradiation in terms of phase filling factors would correspond to a shift in temperature by $\Delta T_{irr} = -2$ K. That, in turn, would correspond to a relative change in resistance of $\Delta R/R = [R(155\,\text{K}) - R(157\,\text{K})]/R(155\,\text{K})) \approx 91\,\%$ from Fig. 1(a) in the main manuscript. Similar considerations can be made all over the temperature range from 155 K to 168 K in Fig. 2(c) in the main manuscript, and the relative resistance changes are always well above 5 % (see examples in Table I).

The conclusion that the effect of minor thermal cycles is considerably smaller than that of the laser is further corroborated by the observation that the phase fractions after laser irradiation from both the heating and cooling curves (Fig. 2(c) in the main manuscript) collapse to approximately the same intermediate values between the curves. If the thermal cycling had a similar effect as the laser irradiation, we would expect it to result in a significant rise

Supplementary Table I. Estimated relative resistance changes by laser irradiation via filling factors of the insulating phase.

T_1	T_2	$\Delta T_{\rm irr} = T_2 - T_1$	filling factor of ins. phase	$\Delta R/R = \frac{R(T_2)-R(T_1)}{R(T_2)}$
(K)	(K)	(K)		(%)
157	155	−2	∼ 0.9	91
160	157	−3	∼ 0.8	96
162	158	−4	∼ 0.7	83
164	160	−4	∼ 0.55	84
166	164	−2	∼ 0.4	35
168	166	−2	∼ 0.3	22

in resistance close to the mid-point value between the resistances of the cooling curve (4.33 kΩ) and heating curve (177 kΩ) at $T_{\rm reverse}$ (see Fig. S4). Since the resistance only increases to 4530 Ω we conclude that the phase fraction after the thermal cycling is much closer to that of the cooling curve than that observed after laser irradiation.

This points to a non-trivial effect of laser irradiation which provides a pathway towards the true equilibrium between the insulating and metallic phases by lowering the free energy barrier between them.

V. MOTT RESISTOR NETWORK SIMULATION

We model and numerically solve our system as a Mott resistor network model as schematized in Fig. S5. A load resistance $R_{\rm load}$ is making a voltage divider circuit with a resistor tensor network.

In order to determine the resistance of the entire network, a small bias voltage $V_{\rm in}$ is applied in order to obtain a voltage $V_{\rm S}$ across the system

$$V_{\rm S} = \frac{R_{\rm S}}{R_{\rm S} + R_{\rm load}} \cdot V_{\rm in} , \tag{S1}$$

where $R_{\rm S}$ denotes the total resistance of the resistor network solved using Kirchhoff laws. Each site of our 50×50 grid is represented by four resistors of two possible values, $R_{\rm met}$ and $R_{\rm ins}$.

In order to simulate the first-order transition we assume a free energy from Landau's theory with shape [4, 5]

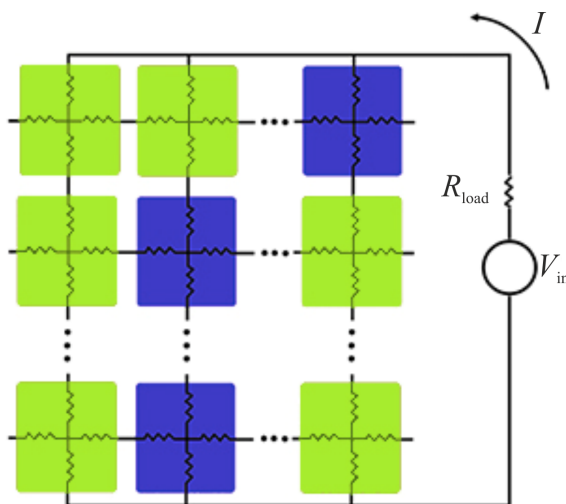$$f(T,\eta) = h(T)\eta + p(T)\eta^2 + c\eta^4 . \tag{S2}$$

FIG. S5. Schematic representation of the Mott resistor network model and simulation circuit. Light green represents insulating sites with a high resistance $R_{\rm ins}$ and the blue cells represent metallic sites with a low resistance $R_{\rm met}$.

Supplementary Table II. Constant parameters of the free energy.

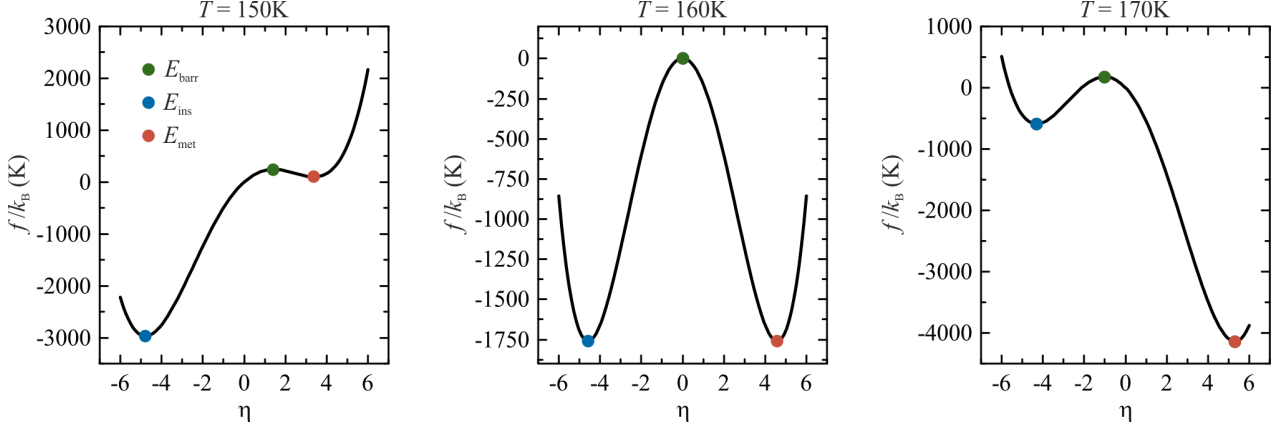| T_c (K)	T_A (K)	h_0/k_B (K)	p_1/k_B (K)	c/k_B (K)
160	87	-2666.67	-200	4

FIG. S6.   Functional form of the free energy $f(\eta)$ of the system with the parameters given in Table. II for three selected temperatures: $T = 150\,\text{K} < T_c$, $T = 160\,\text{K} = T_c$, $T = 170\,\text{K} > T_c$. The green markers show the local maxima E_{barr}, the blue and red markers show the minima E_{ins} and E_{met} of the free energy, respectively.

T is the temperature, η is an order-parameter-like quantity,

$$h(T) = h_0 \cdot \frac{T - T_c}{T_c - T_A} \, , \tag{S3}$$

and

$$p(T) = p_1 \cdot \frac{T - T_A}{T_A}, \tag{S4}$$

with a critical temperature T_c, where the free energy is symmetric, and T_A, h_0, p_1, c are constant parameters, specified in Table II.

As illustrated for three selected temperatures around T_c in Fig. S6, the free energy exhibits two minima with energies E_{met} and E_{ins} and one local maximum E_{barr}. The temperature dependence of the energies of these stationary points is shown in Fig. S7.

Each resistor in the network is in a metallic state with energy E_{met} or in an insulating state with energy E_{ins}. In each simulation cycle, we assign an escape criterion to each site, dependent on whether the initial state is metallic or insulating.
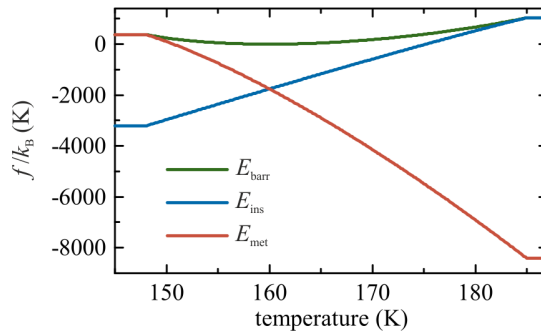

FIG. S7.   Temperature dependence of the energies E_{met} of the metallic state (red), E_{ins} of the insulating state (blue) and E_{barr} of the barrier (green), computed as stationary points of Eq. (S2).

Supplementary Table III. Constant parameters of the simulations.

V_{in} (V)	C_v (J/K)	k_h (J/K)	R_{met} (Ω)	R_{ins} (Ω)
10^{-5}	1	0.166	10	$1.5 \cdot 10^7$

- The criterion to reach the energy barrier from the metallic state is

$$P_{\text{Met} \rightarrow \text{Barrier}} = e^{\frac{-(E_{\text{barr}} - E_{\text{met}} - \Gamma)}{k_{\text{B}} T}} \ . \tag{S5}$$

- The criterion to reach the barrier from an insulating state is

$$P_{\text{Ins} \rightarrow \text{Barrier}} = e^{\frac{-(E_{\text{barr}} - E_{\text{ins}} - \Gamma)}{k_{\text{B}} T}} \ . \tag{S6}$$

k_{B} denotes the Boltzmann constant and Γ the energy contribution of the laser in both equations. We generate a random number between zero and one and compare it to the escape criterion of Eq. (S5) or Eq. (S6) with a constant number of iterations, respectively. If the escape criterion exceeds the random number, we assign a resistivity R_{ins}, by assuming Boltzmann weights, with probability

$$P_{\text{ins}} = \frac{e^{\frac{-E_{\text{ins}}}{k_{\text{B}} T}}}{e^{\frac{-E_{\text{ins}}}{k_{\text{B}} T}} + e^{\frac{-E_{\text{met}}}{k_{\text{B}} T}}}, \tag{S7}$$

or R_{met} with probability

$$P_{\text{met}} = \frac{e^{\frac{-E_{\text{met}}}{k_{\text{B}} T}}}{e^{\frac{-E_{\text{ins}}}{k_{\text{B}} T}} + e^{\frac{-E_{\text{met}}}{k_{\text{B}} T}}} \ . \tag{S8}$$

T is the local temperature on the site updated at each cycle by the following formula using the heat equation through the discrete Laplacian approximation

$$T_{ij} = T_{\text{subs}} + \frac{V^2}{C_v R_{ij}} + 4T_{ij} - k_h \sum_{<ik>}^{\text{first neighboors}} T_{ik} \ , \tag{S9}$$

where the indices i and j denote the coordinates of the site in the network, T_{subs} the substrate temperature, C_v the specific heat of the system, k_h the thermal conductivity and $\sum_{<ik>}^{\text{first neighboors}}$ denotes the summation over the first neighbouring sites around the one with coordinates ij. The constant parameters used in our calculations are summarized in Table III.

VI. REFERENCES

[1] M. M. Lange, S. Guénon, F. Lever, R. Kleiner, and D. Koelle, A High-Resolution Combined Scanning Laser and Widefield Polarizing Microscope for Imaging at Temperatures from 4 K to 300 K, Review of Scientific Instruments **88**, 123705 (2017).
[2] M. M. Lange, A High-Resolution Polarizing Microscope for Cryogenic Imaging: Development and Application to Investigations on Twin Walls in SrTiO$_3$ and the Metal-Insulator Transition in V$_2$O$_3$, Ph.D. thesis, Universität Tübingen (2018).
[3] J. Trastoy, Y. Kalcheim, J. del Valle, I. Valmianski, and I. K. Schuller, Enhanced Metal–Insulator Transition in V$_2$O$_3$ by Thermal Quenching after Growth, Journal of Materials Science **53**, 9131 (2018).
[4] J. del Valle, P. Salev, F. Tesler, N. M. Vargas, Y. Kalcheim, P. Wang, J. Trastoy, M.-H. Lee, G. Kassabian, J. G. Ramírez, M. J. Rozenberg, and I. K. Schuller, Subthreshold firing in Mott nanodevices, Nature **569**, 388 (2019).
[5] P. Stoliar, J. Tranchant, B. Corraze, E. Janod, M. Besland, F. Tesler, M. Rozenberg, and L. Cario, A leaky-integrate-and-fire neuron analog realized with a Mott insulator, Advanced Functional Materials **27**, 1604740 (2017).